Diss. ETH No. 22188

ATTOSECOND XUV COINCIDENCE SPECTROSCOPY

A thesis submitted to attain the degree of

DOCTOR OF SCIENCES OF ETH ZURICH

(DR. SC. ETH ZURICH)

presented by

MAZYAR SABBAR

Dipl.-Phys. (Leibniz Universität Hannover)

born on 21.09.1983

citizen of Germany

accepted on the recommendation of

Prof. Dr. U. Keller, Supervisor
Prof. Dr. H. J. Wörner, Co-Examiner
PD. Dr. L. Gallmann, Co-Examiner

2014

Table of Contents

Symbols and Abbreviations **VI**

Symbols VI

Abbreviations VIII

List of Figures **X**

Publications **XV**

Journal papers XV

Conference papers XVII

Abstract **XIX**

Kurzfassung (German) **XXI**

Chapter 1 Introduction **1**

Chapter 2 Femtosecond laser system for attosecond science **7**

2.1 Few-cycle Ti:sapph laser oscillator 8

2.2 Chirped pulse multipass amplifier 10

2.3 Carrier-envelope-phase stabilized CPA 12

2.4 Temporal characterization of ultrashort pulses 13

2.5 Hollow-core fiber compression stage 16

Chapter 3 High harmonic generation **19**

3.1 Semi-classical three-step model 20

3.2 Macroscopic response 25

3.3 Attosecond pulse trains 28

3.4 The RABBITT technique 29

Chapter 4 Single attosecond pulses 33
4.1 Schemes for SAP generation 34
4.2 The attosecond streaking technique 38
4.3 The FROG-CRAB technique 40

Chapter 5 The COLTRIMS detector 45
5.1 The COLTRIMS apparatus 45
5.2 Reconstruction of the 3D momenta of fragments 46
5.3 Calibration of the detector 48
5.4 Coincidence detection 51

Chapter 6 Combining attosecond pulses with coincidence spectroscopy 53
6.1 Overview 54
6.2 Vacuum chambers and vacuum system 56
6.3 IR-only experiments 58
6.4 Active interferometer stabilization 58
6.5 XUV-IR pump-probe experiments and single attosecond pulse characterization 61

Chapter 7 3D attosecond streak camera 67
7.1 Introduction 67
7.2 Ellipticity adjustment via above threshold ionization 67
7.3 Resolving the rotating electric field vector in 3D 68
7.4 Conclusion 69

Chapter 8 Attochirp-corrected ionization time delays using coincidence spectroscopy 71
8.1 Introduction and motivation 72
8.2 The Wigner time delay 73
8.3 Experimental setup 76
8.4 Time delay extraction from attosecond streaking 77
8.5 Attochirp-corrected time delays from coincidence streaking 80
8.6 Influence of data processing on time delay extraction from FROG-CRAB 83
8.7 Discussion 85

Chapter 9 Conclusion and outlook **87**

References **93**

Curriculum Vitæ **99**

Acknowledgements **100**

Symbols and Abbreviations

Symbols

$\mathbf{A}_\mathrm{L}$	vector potential
A_q	single atom response for the qth harmonic
α	ratio between electric field amplitudes
$\boldsymbol{B}$	magnetic field
c	speed of light in vacuum
e	electron charge
$\mathbf{E}_\mathrm{IR}$	electric field of the IR pulse
η	phase of single-photon transition amplitude
ε	ellipticity
E	photon / electron energy
φ	phase
I	intensity
I_p	ionization potential
κ	ionization fraction
k	wave vector
λ	wavelength
l	orbital angular momentum
L	length
m	magnetic quantum number
m_e	electron mass
N_atm	atomic number density at one atmosphere
ω	angular frequency

w	$1/e^2$ beam radius
ψ	wave function
P	gas pressure in atmospheres
$\boldsymbol{p}$	momentum
ρ	particle density
r_e	classical electron radius
T_p	pulse duration
τ_W	Eisenbud-Wigner-Smith time delay (or Wigner delay)
V	potential
W_dc	ADK-rate

Abbreviations

ADK	Ammosov-Delone-Krainov
Ag	silver
AIS	active interferometer stabilization
Al	aluminum
AOM	acousto-optic modulator
APT	attosecond pulse train
Ar	argon
ATA	attosecond transient absorption
ATI	above-threshold ionization
CCD	charge-coupled device
CEP	carrier envelope phase
CM	chirped mirror
COM	center–of-mass
COLTRIMS	cold target recoil ion momentum spectroscopy
CPA	chirped pulse amplifier
CRAB	complete reconstruction of attosecond bursts
cw	continuous wave
DFG	difference frequency generation
DOG	double optical gating
EOM	electro-optic modulator
FROG	frequency-resolved optical gating
FWHM	full width at half maximum
GD	group delay
GDD	group delay dispersion
HH	high harmonic
HHG	high harmonic generation
HCF	hollow-core fiber

IR	infrared
KLM	Kerr-lens mode locking
MCP	multi channel plate
Nd:YLF	neodymium-doped yttrium lithium fluoride
Ne	neon
OA	optic axis
OC	output coupler
OPA	optical parametric amplifier
PC	Pockels cell
PD	photo diode
PPLN	periodically poled lithium niobate
RABBITT	reconstruction of attosecond beating by interference of two-photon transitions
RMS	root-mean-square
SAP	single attosecond pulses
SAE	single-active-electron approximation
SB	side band
SFG	sum frequency generation
SH	second harmonic
SPIDER	spectral phase interferometry for direct electric-field reconstruction
SPM	self-phase modulation
TDSE	time-dependent Schrödinger equation
TISE	time-independent Schrödinger equation
Ti:sapph	titanium-sapphire
TOF	time-of-flight
UV	ultraviolet
VMIS	velocity-map-imaging spectrometer
XUV	extreme ultraviolet

List of Figures

Figure 2.1. Evolution of ultrafast lasers. At the end of the 1980s dye lasers were rapidly replaced by the Ti:sapph laser. Since then the pulse duration has been pushed to its physical limit for central frequencies lying in the visible to infrared............ 8

Figure 2.2 Ti:sapph oscillator Rainbow™. The Ti:sapph crystal is pumped with a 532 nm laser (Coherent Verdi V5). After being coupled out via the output coupler (OC) the pulses pass a pair of chirped mirrors (CM) for pulse compression. The AOM, the periodically poled lithium niobate (PPLN) and the photodiode (PD) are part of the CEP stabilization described in section 2.4. 9

Figure 2.3. Simplified illustration of the commercial multipass amplifier system. The amplifier is seeded with the Rainbow™ oscillator described in section 2.1. After 9 amplification passes through the Ti:sapph crystal, pulses of 28 fs duration and 750 µJ pulse energy at a repetition rate of 10 kHz are generated. A detailed description can be found in the text. 11

Figure 2.4. The most established schemes for the temporal characterization of ultrashort laser pulses. Details can be found in the text............ 15

Figure 2.5. Hollow-core fiber compression. In (a) the spectra of the amplifier and the hollow-core fiber (HCF) using are presented. The spectral broadening has been achieved through SPM inside the HCF which was filled with 2.5 bar of Ne. Using the SPIDER technique the pulses were temporally characterized as shown in (b). 17

Figure 3.1. Simplified illustration of the characteristic HH spectrum. On the left side a steep decrease of the harmonic yield is observed corresponding to the classical perturbative regime. In the middle part a plateau appears which cannot be explained in the perturbative picture. The right part in which the yield drops is called the cut-off of the spectrum............ 20

Figure 3.2. Three-step model for HHG. Left panel: The IR field bends the ionic potential allowing for the electron to tunnel ionize. Middle panel: The IR field has changed sign, accelerating the electron back to the core. Right panel: The electron reaches the position of the ion core and hence recombines with it. Upon this process a photon is emitted. For details see text............ 21

Figure 3.3. Electron trajectories in HHG. (a) Illustration of the electron trajectories after ionization. Those trajectories which eventually recombine with the ion core are shown in blue while the non-recombining ones are represented in green. (b) The recombination time of the electron can be determined by the tangent at the time of birth............ 24

Figure 3.4. Return energies of the recombining electrons as a function of time of birth within the cycle. Two types of trajectories are generated (short and long trajectories) leading to the same final kinetic energy. The distribution shows a characteristic maximum of $3.17 \cdot U_{\mathrm{p}}$ which is referred to as cut-off energy. 25

Fig 3.5. Illustration of the phase mismatch between emitted harmonic radiation. As the IR field propagates through the medium, harmonics at different positions are generated. Due to the difference in the refractive indices of the ionized medium for the IR and harmonic field, a phase mismatch can occur leading to a decrease of the harmonic yield. 27

Figure 3.6. (a) Principle of the RABBITT technique illustrated by two consecutive HH. The SB18 can be populated upon the excitation path HH17 plus absorption of one IR photon or upon absorption of HH19 plus emission of one IR photon. (b) RABBITT spectrogram. Recording electron spectra for different XUV-IR delays leads to a typical spectrogram, here measured with the COLTRIMS apparatus. 30

Figure 4.1. Illustration of important gating schemes for SAP generation. Detailed information can be found in the text. 37

Figure 4.2. Principle of the attosecond streak camera. (a) The SAP produces a continuous electron distribution (blue) upon ionization of a ground state electron (here Ar). If an additional IR field is used the whole spectrums shifts according to the product $v_0 A_{\mathrm{L}}$. (b) Recording the electron spectrum as a function of XUV-IR delay reveals a spectrogram with a modulation that follows approximately the vector potential of the IR field. 38

Figure 4.3. Simulated FROG-CRAB trace. Following parameter were used: A $5\,\mathrm{fs}$ IR pulse with $10^{13}\,\mathrm{W/cm^2}$ intensity and a chirped attosecond pulse with a transform-limit of $150\,\mathrm{as}$ and a GDD of $2000\,\mathrm{as}^2$. 41

Figure 4.4. Testing the time delay extraction from FROG-CRAB. In (a) a matrix has been prepared containing two attosecond streaking traces delayed by 200 as. The reconstructed phases of both parts φ^{up} and φ^{low} (c) allows to determine the time delay between both traces (d). 42

Figure 4.5. Testing the time delay extraction from FROG-CRAB. Same plots as in Fig. 4.4 except that a time delay of only 10 as has been chosen. 43

Figure 5.1. Schematic of a COLTRIMS detector. A XUV pulse (blue) ionizes atoms or molecules in the supersonic gas jet of the COLTRIMS. A delayed IR pulse is used as a probe. The fragments arrive either on the left or the right detector depending on the sign of the charge. Detailed information can be found in the text. 46

Figure 5.2. Typical TOF distribution in a Ar/Ne gas mixture. The peak appearing for very small TOF values corresponds to strayed photons hitting the MCP detector. These counts can be used for a first estimation of the time-zero calibration. 49

Figure 5.3. Schematic illustration of the cyclotron time t_c vs. index N. This plot can be used to determine the *B*-field strength from the acquired data. A residual offset δt can be caused either from a wrong estimation of N or from inaccuracies of the time zero calibration depending on the size of δt 50

Figure 5.4. Sum of the momentum distributions along the *z*-direction for Ar and Ne. Due to momentum conservation after single photon ionization, this distribution has to peak at 0 momentum. 50

Figure 5.5. Applying a coincidence filter on the 3D electron momentum distribution measured in a gas target containing Ar and Ne. The plot on the left panel shows the momentum distribution as measured for both species. On the right panel the distributions are shown as obtained by applying a coincidence filter on the momentum sum. 51

Figure 6.1. Schematic representation of the combined attosecond beamline (left side) and COLTRIMS apparatus (right side). The IR driving pulses are divided into two using a 20% beam-splitter. The more intense part is focused in the gas target in order to generate HH. The weaker part is sent through a delay line and then recombined with the XUV light by a holey mirror. Both beams are sent on a toroidal mirror which has its focus in the interaction region of the COLTRIMS. The beam of the active interferometer stabilization system is depicted by the green line. A more detailed description can be found in the text. 55

Figure 6.2. Schematic of the vacuum system of the AttoCOLTRIMS. A high vacuum in the COLTRIMS chamber needs to be guaranteed for the conduction of experiments with a good signal-to-noise ratio. A detailed description can be found in the text. 57

Figure 6.3. Illustration of the beam paths for the AIS. The filter unit removes the central part of the IR beam and cw light in the pump arm. The remaining donut-shape beam is reflected by the rear side of the holey mirror. Here it recombines with the light coming from the probe arm which passes through the hole of the mirror. After removal of the residual IR by the band-pass filter, the cw light is focused onto the CCD camera used to image the interference fringes. See the text for a more detailed description. 59

Figure 6.4. Characterization of the AIS. (a) Evolution of the control voltage applied to the piezo translation stage while operating the AIS over 7 h. (b) RMS variation of the recorded phase over the same time interval yielding a standard deviation of about 60 as. 61

Figure 6.5. Schematic illustration of the 3D momentum distribution of electrons (blue shaded area) in attosecond streaking. In (a) the IR-unperturbed distribution is shown. Electrons of same energy can have momenta in different direction (red arrows). (b) If an IR field, polarized along the *z*-direction is overlapped, a momentum shift will be introduced leading to different final energies even though both electrons had the same initial energy. 63

Figure 6.6. Momentum distribution of electrons in an attosecond streaking measurement conducted in Ne. The distribution contains all elections counts measured during the complete experiment. Here z is the direction of the IR streaking polarization. For the extraction of the streaking trace, only those electrons are considered that lie within the positive half of the $40°$ cone.................... 64

Figure 6.7. Reconstruction of a SAP produced with the AttoCOLTRIMS. (a) Attosecond streaking spectrogram measured with the COLTRIMS apparatus using Ar for the HH generation and Ne as the target gas. (b) FROG-CRAB reconstruction of the trace. (c) Reconstructed spectrum and phase of the pulse. (d) The time-domain representation reveals a pulse duration of 280 as with a GDD of $\sim 16000\,\mathrm{as}^2$. 65

Figure 7.1. 3D reconstruction of the vector potential of an elliptically polarized few-cycle IR pulse by attosecond streaking in the COLTRIMS apparatus. The red circles/line show the motion of the COM of the electron distribution modulated by the IR pulse. The projection of the oscillations is presented in black. The expected phase shift of about $90°$ between the y- and z- component of the light field can already be seen from the blue lines drawn at a delay position of 0 fs 69

Figure 8.1. Photoemission process modeled with a potential well. Solving the TISE for scattering of the waves entering from left yields the blue line. The potential well introduces a phase shift η onto the scattered relative to the free wave function (red line). 74

Figure 8.2. Extraction of time delays from attosecond streaking assuming a short-range Yukawa-potential. It can be shown that in this case the Wigner delay τ_W is given directly by the difference of the vector potential A_L and the streaking trace itself. 75

Figure 8.3. Attosecond coincidence streaking. (a) Streaking photoelectron spectrogram obtained from photoelectrons originating from simultaneous ionization of Ne and Ar streaked by an IR intensity of about $3\cdot 10^{12}\,\mathrm{W/cm}^2$. (b) If each photoelectron is assigned to its parent ion by applying a coincidence filter, two separate streaking spectrograms are obtained. 77

Figure 8.4 Time delay extraction from two traces obtained from coincidence streaking. (a) Simultaneously measured streaking traces for Ar and Ne obtained by applying a coincidence filter. An apparent time shift $\Delta\tau$ can be retrieved by comparing the delay position of the central maximum. (b) Time dependent COM energy shift extracted from the spectrograms (open circles) for Ar (red) and Ne (blue) with corresponding fit (dashed line). 78

Figure 8.5. Influence of the ionization cross-section on the electron distribution of Ar and Ne. Cross-sections and electron spectra as retrieved by applying the FROG-CRAB algorithm to the data shown in Fig. 8.4 (a). (a) Ionization cross-section of Ar (red line) and Ne (blue line). (b)

Photoelectron spectra of Ar (blue solid line) and Ne (red solid line) as retrieved by the FROG-CRAB algorithm. If the corresponding photoabsorption cross-sections (Fig. 8.5 (a)) are considered, the corrected spectra (red dashed line for Ar, blue dashed line for Ne) are similar and in particular peak at the same XUV photon energy of about 37 eV. 79

Figure 8.6. FROG-CRAB reconstruction of time delay between Ar and Ne. Measured (a) and reconstructed (b) spectrograms for Ne and Ar photoelectrons; before running the retrieval algorithm the two traces are patched together onto a common energy axis in order to ensure consistency in the reconstruction (see main text). (c) Retrieved spectra (solid lines) and group delay (dashed lines) of the photoelectron wavepacket for Ar (red) and Ne (blue). The vertical and horizontal black lines indicate that comparing the group delays for both species at the same photoelectron energy results in a time delay $\Delta\tau^{\mathrm{Ar/Ne}} \approx -100\,\mathrm{as}$. 81

Figure 8.7.Ionization time delays reconstructed from FROG-CRAB. (a) XUV spectra (solid lines) and group delays (dashed lines) for Ar (red) and Ne (blue) computed from the reconstruced streaking spectrograms shown in Fig. 3 (c) adding the ionization potential of the two targets. (b) For any XUV energy within a range where the spectral intensity of Ar and Ne spectra overlaps (between 28 and 38 eV), a time delay $\Delta\tau^{\mathrm{Ar/Ne}}$ is calculated for a total number of 33 independently measured traces. The green band represents the one-sigma confidence interval of the reconstructed time delays using smoothed streaking traces, which agrees well with the mean value extracted from the noisy raw traces (green open circles). The black solid line is a theory curve obtained by computing the contributions of one-photon matrix elements within the random-phase approximation (RPAE) [80] and of the continuum-continuum laser driven transition [87] for both gas targets. 82

Figure 8.8. Time delays for an arbitrarily chosen double trace from the dataset containing 33 traces... 84

Publications

Parts of this thesis are published in the following journal papers and conference proceedings.

Journal papers

1) M. Sabbar, S. Heuser, R. Boge, M. Lucchini, L. Gallmann, C. Cirelli, U. Keller, "Combining attosecond XUV pulses with coincidence spectroscopy", submitted

2) M. Sabbar, S. Heuser, R. Boge, M. Lucchini, L. Gallmann, C. Cirelli, U. Keller, "Direct measurement of photoemission time delays in Ar and Ne", submitted

3) R. Boge, S. Heuser , M. Sabbar, M. Lucchini, L. Gallmann, C. Cirelli, U. Keller, "Revealing the time dependent polarization of ultrashort pulses with sub-cycle resolution", to be submitted

4) C. A. Arrell, J. Ojeda, M. Sabbar, W. Okell, T. Witting, T. Siegel, Z. Diveki, S. Hutchinson, L. Gallmann, U. Keller, F. van Mourik, R. Chapman, C. Cacho, N. Rodrigues, I. C. E. Turcu, J. W. G. Tisch, E. Springate, J. P. Marangos, M. Chergui, "A simple electron time-of-flight spectrometer for ultrafast VUV photoelectron spectroscopy of liquid solutions", to be submitted

5) R. Locher, M. Lucchini, J. Herrmann, M. Sabbar, M. Weger, A. Ludwig, L. Castiglioni, M. Greif, J. Osterwalder, M. Hengsberger, L. Gallmann, U. Keller, "Versatile attosecond beamline in a two-foci configuration for simultaneous time-resolved measurements". Review of Scientific Instruments, vol. **85**, 013113, 2014

6) J. Herrmann, M. Weger, R. Locher, M. Sabbar, P. Rivière, U. Saalmann, J.–M. Rost, L. Gallmann, U. Keller, “Virtual single-photon transition interrupted: time-gated optical gain and loss”, Phys. Rev. A, vol. **88**, 043843, 2013

7) M. Lucchini, J. Herrmann, A. Ludwig, R. Locher, M. Sabbar, L. Gallmann, U. Keller, “Role of electron wave-packet interference in the optical response of helium atoms”, New Journal of Physics, vol. **15**, 103010, 2013

8) L. Gallmann , J. Herrmann, R. Locher, M. Sabbar, A. Ludwig, M. Lucchini, U. Keller, “Resolving intra-atomic electron dynamics with attosecond transient absorption spectroscopy”, Molecular Physics, vol. **111**, Nos. 14-15, 2243-2250, 2013

Conference papers

1) S. Heuser, M. Sabbar, C. Cirelli, U. Keller, “Photoionization Time Delay in Molecular Hydrogen” (Post-deadline Talk), Ultrafast Phenomena, Okinawa, Japan, July 7-11, 2014

2) M. Sabbar, S. Heuser, R. Boge, M. Lucchini, L. Gallmann, C. Cirelli, U. Keller, “Probing single photon ionization times with coincidence spectroscopy”, Gordon Research Conference (GRC) on Multiphoton Processes, Waltham, USA, June 15-20, 2014

3) R. Boge, M. Sabbar, S. Heuser, C. Cirelli, L. Gallmann, U. Keller, “Combining attosecond science with coincidence momentum spectroscopy” (Talk), Conference on Lasers and Electro-Optics (CLEO) US, San Jose, USA, May 8-13, 2014

4) M. Sabbar, S. Heuser, R. Boge, C. Cirelli, L. Gallmann, U. Keller, “Combining Attosecond Science with Coincidence Momentum Spectroscopy”, NCCR MUST annual meeting, Engelberg, Switzerland, January 8-10, 2014

5) J. Herrmann, M. Weger, R. Locher, M. Sabbar, P. Rivière, U. Saalmann, J.-M. Rost, L. Gallmann, U. Keller, “Optical gain by interrupting the temporal evolution of a dipole”, ATTO2013, Paris, France, July 8-12, 2013.

6) M. Lucchini, J. Herrmann, A. Ludwig, M. Sabbar, R. Locher, L. Gallmann, U. Keller, “Role of electron wave-packet interference in the optical response of helium”, ATTO2013, Paris, France, July 8-12, 2013.

7) J. Herrmann, M. Lucchini, A. Ludwig, M. Sabbar, R. Locher, L. Gallmann, U. Keller, “Probing Electron Wave-packet Interference” (Talk), Conference on Lasers and Electro-Optics (CLEO) US, San Jose, USA, June 9-14, 2013

8) J. Herrmann, M. Weger, R. Locher, M. Sabbar, P. Rivière, U. Saalmann, J.-M. Rost, L. Gallmann, U. Keller, "Creation of Optical Gain and Absorption via a Virtual Single photon Transition", Conference on Lasers and Electro-Optics (CLEO) US, San Jose, USA, June 9-14, 2013

9) M. Lucchini, J. Herrmann, A. Ludwig, M. Sabbar, R. Locher, L. Gallmann, U. Keller, "Optical Response of Electron Wave-packet Interference Revisited" (Talk), Conference on Lasers and Electro-Optics (CLEO) Europe, Munich, Germany, May 12-16, 2013

10) J. Herrmann, M. Weger, R. Locher, M. Sabbar, P. Rivière, U. Saalmann, J.-M. Rost, L. Gallmann, U. Keller, "Interrupted virtual single-photon transition", Conference on Lasers and Electro-Optics (CLEO) Europe, Munich, Germany, May 12-16, 2013

11) C. Arrell, M. Sabbar, J. Ojeda Andara, L. Gallmann, M. Chergui, U. Keller, "Photoemission from liquid solution using high harmonic generation", NCCR MUST annual meeting, Engelberg, Switzerland, January 8-10, 2013

12) M. Weger, R. Locher, M. Sabbar, J. Herrmann, L. Gallmann, U. Keller, "High Harmonic Generation and Attoscience", NCCR MUST annual meeting, Lenk, Switzerland, January 8-12, 2012

13) C. Arrell, M. Scarongella, M. Sabbar, M. Brown, H.-J. Wörner, L. Gallmann, F. Van Mourik, U. Keller, M. Chergui, "Time-resolved photoelectron spectroscopy from liquid microjets using high harmonic generation", NCCR MUST annual meeting, Lenk, Switzerland, January 9 - February 14 , 2011

Abstract

In recent years the technological advancements in attosecond science have paved the way for monitoring the electron dynamics in atomic, molecular and solid state systems with attosecond resolution [1-3]. Today, researchers are able to address one of the most fundamental questions in quantum mechanics: How fast can light remove a bound electron from an atom, a molecule or a solid target [1,3,4]? There are mainly three experimental techniques that have proven their ability: The attoclock [5] which addresses tunneling time upon multi photon ionization and the RABBITT [6] and attosecond streaking [7] technique which probe dynamics following single photon ionization. While the attoclock technique requires full access to the momentum in the polarization plane of the ionizing field which is ensured by the 3D momentum resolution of a COLTRIMS [8,9] detector, the electron dynamics upon single photon ionization has so far only been probed with detectors providing 1D or 2D resolution.

In this thesis an attosecond XUV beamline providing single attosecond pulses has been designed, built up and combined with the unique possibilities of a COLTRIMS apparatus to study electron dynamics initiated by single photon ionization. Unlike common charge fragment detectors in the attosecond community the COLTRIMS offers full 3D momentum resolution and coincidence capability. Both of these features have been exploited in the framework of this thesis to conduct novel experiments probing attosecond dynamics.

The beamline provides single attosecond pulses originating from the process of high harmonic generation using waveform controlled few-cycle infrared pulses combined with the polarization gating technique. To allow for XUV-IR pump-probe experiments a Mach-Zehnder type interferometer has been set up. Due to the much lower count rates achievable with detectors with coincidence capability, long-term few-nanometer interferometric stability is essential. Therefore, an active interferometer stabilization has been implemented and proven to provide optimal conditions. Using this capability first attosecond streaking experiments have been performed in a COLTRIMS detector allowing to verify the production of single attosecond pulses.

Using the combination of the 3D momentum resolution of the COLTRIMS and the temporal resolution of single attosecond pulses the rotating electric field vector of an intense infrared pulse has been characterized for the first time. This method offers a route for the in situ characterization of the time-dependent polarization of light fields.

In addition we have taken advantage of the coincidence capability of the COLTRIMS apparatus by performing experiments which we refer to as coincidence attosecond streaking. Here, we have used a gas mixture containing multiple atomic or molecular species. Conducting attosecond streaking measurements on such a target delivers a spectrogram containing all different types of electrons. A coincidence filter allows then to assign the electrons to their parent ion through momentum conservation and thereby to extract multiple streaking spectrograms from one single measurement. These spectrograms have been recorded under identical conditions allowing to extract unambiguously the relative timing between emitted electrons originating from different species. A careful analysis of our data has demonstrated the crucial role of the chirp of the attosecond pulses in the time delay extraction, which was not taken into account in previous studies. We present a general route to overcome this source of error leading to corrected time delays of tens of attoseconds between valence electrons originating from argon and neon. We show that these results are in agreement with predictions based on the calculation of the transition matrix elements for two-photon ionization.

Kurzfassung (German)

Der technologische Fortschritt in der Attosekundenphysik hat es in den vergangenen Jahren ermöglicht die Elektronendynamik in atomaren und molekularen Systemen sowie in Festkörpern zu verfolgen [1-3]. Heute können Wissenschaftler eine der fundamentalsten Fragen der Quantenmechanik adressieren: Wie schnell kann Licht ein gebundenes Elektron von einem Atom, Molekül oder Festkörper entfernen [1,3,4]? Es gibt im Wesentlichen drei Methoden, welche das Potential zu solchen Messungen unter Beweis gestellt haben: Die Attoclock [5], welche die Tunnelzeit des Elektrons nach einer Multi-Photon-Anregung adressiert und die RABBITT- [6] und Attosekunden-Streaking [7] Methoden, welche die Elektronendynamik nach einer Einzel-Photon-Anregung abfragen. Während die Attoclock-Technik den vollen Zugang zum Impuls in der Polarisationsebene des ionisierenden Strahls verlangt, welcher durch die 3D Impulssauflösung eines COLTRIMS Detektors [8,9] gewährleistet wird, wurde die Elektronendynamik nach einer Einzel-Photon-Anregung bisher nur mit Detektoren untersucht, welche eine 1D bzw. eine 2D Auflösung bieten.

Im Rahmen dieser Arbeit wurde eine Attosekunden-XUV-Beamline konzipiert und aufgebaut und mit den einzigartigen Möglichkeiten eines COLTRIMS Detektors verbunden, um die Elektronendynamik nach einer Einzel-Photon-Anregung zu untersuchen. Im Gegensatz zu den üblicherweise verwendeten Detektoren in der Attosekunden-Gemeinde, bietet der COLTRIMS Apparat volle 3D Impulsauflösung bei gleichzeitiger Koinzidenzdetektion. In dieser Arbeit wurden beide Eigenschaften ausgenutzt, um neuartige Experimente mit Attosekunden-Auflösung durchzuführen.

Die Beamline stellt einzelne Attosekunden-Pulse bereit, welche aus dem Prozess der Erzeugung von hohen Harmonischen stammen. Hierzu werden phasenstabilisierte infrarot Pulse mit nur wenigen Zyklen in Kombination mit der Polarization-Gating-Technik in ein Edelgas fokussiert. Um XUV-IR pump-probe Experimente zu ermöglichen wurde ein Mach-Zehnder Interferometer aufgebaut. Wegen der sehr viel geringeren Zählraten in Experimenten mit Koinzidenzdetektion, ist eine interferometrische Stabilität auf der Skala von wenigen Nanometern unabdingbar. Daher wurde eine aktive Interferometer-Stabilisierung aufgebaut, welche nachweislich optimale Bedingungen gewährleistet. Mit diesem Potential ausgestattt haben wir erste Attosekunden-Streaking Messungen in einem COLTRIMS Detektor durchgeführt und zugleich den Nachweis für die Produktion von einzelnen Attosekundenpulsen erbracht.

Unter Ausnutzung der Kombination von 3D Impulsauflösung des COLTRIMS Detektors und der Zeitauflösung von einzelnen Attosekundenpulsen wurde im Rahmen dieser Arbeit zum ersten Mal die Rotation des elektrische Feldvektors eines intensiven infrarot Pulses gemessen. Diese Methode bietet einen Weg für die in situ Charakterisierung der zeitabhängigen Polarisation von Lichtfeldern.

Zusätzlich wurde im Rahmen dieser Arbeit auch die Koinzidenzdetektion des COLTRIMS Apparates durch Messungen, welche wir ''Koinzidenz-Attosekunden-Streaking'' nennen, ausgeschöpft. Hier verwenden wir ein Gasgemisch aus unterschiedlichen atomaren oder molekularen Spezies. Die Durchführung von Attosekunden-Streaking Messungen an einem solchen Gemisch liefert ein Spektrogramm, das sämtliche Elektronentypen enthält. Die Anwendung eines Koinzidenzfilters hilft nun die gemessenen Elektronen ihren zugehörigen Ionen über Impulserhaltung zuzuordnen und so mehrere Streaking-Spektrogramme aus einer einzelnen Messung zu extrahieren. Die Spektrogramme wurde unter identischen Bedingungen aufgenommen, was eine eindeutige Bestimmung von relativen Zeitverzögerungen der emittierten Elektronen unterschiedlicher Spezies ermöglicht. Eine genaue Analyse unserer Daten hat erwiesen, dass der Chirp des verwendeten Attosekundenpulses eine wesentliche Rolle in der Extraktion von Zeitverzögerungen spielt, was in bisherigen Studien nicht berücksichtigt wurde. In dieser Arbeit präsentieren wir einen allgemeinen Weg diese Fehlerquelle zu vermeiden. Unsere Messungen, durchgeführt an den Valenzelektronen von Argon und Neon, zeigen korrigierte Ergebnisse, welche energieabhängige Zeitverzögerungen von einigen zehn Attosekunden aufweisen. Diese Ergebnisse sind in Überstimmung mit Vorhersagen basierend auf der Berechnung von Übergangsdipolmomenten für zwei-Photon-Übergänge.

Chapter 1

Introduction

The field of attosecond science started at the turn of the millennium. Since the very early results a lot of progress has been made both from the technological as well as from the scientific point of view. The pulse duration has been pushed down to a few tens of attoseconds [10,11] while intriguing measurements have been performed addressing fundamental questions in quantum physics [1,12]. But what exactly makes these incredibly short pulses so attractive for scientists?

To answer this question it is worth to make a step back to the mid of the 1980s when Ahmed Zewail and co-workers developed the field of femtochemistry. In 1985 Zewail's group presented a pioneering work on the bond breakage of iodine cyanide $\left(\mathrm{ICN}^{*} \rightarrow \mathrm{I}+\mathrm{CN}\right)$ [13]. Here, they had used for the first time femtosecond laser arrangements to perform time-resolved spectroscopy[1]. At this time the resolution was limited to 400 fs. Nevertheless, this allowed them to conclude that the breakage occurs after about 500 fs. The same reaction was studied two years later [14] with improved resolution leading to the observation of the complete breakage process including the intermediate products. This was a major breakthrough since transition states were thought to be elusive. These exciting findings led to the development of a whole new field involving the study of molecular bonds and molecules with different degrees of complexity ranging from diatomic-molecules to proteins and DNA [15].

Interestingly Zewail, who was awarded with the Noble prize in 1999, stated in the perspective-section of a review paper from 2000 [15]:

---

[1] The pump-probe technique has been used: An initial pump pulse triggers the dynamics followed by a time-delayed second pulse that probes the system.

"Since the current femtosecond lasers (4.5 fs) are now providing the limit of time resolution for phenomena involving nuclear motion, one may ask: Is there another domain in which the race against time can continue to be pushed? Sub-fs or attosecond resolution may one day allow for the direct observation of the coherent motion of electrons".

Indeed this perspective was quite appropriate. As Zewail pointed out the natural dynamics of nuclear motion within molecules takes place on the femtosecond time-scale. In contrast the electron motion in an atomic or molecular systems is generally much faster due to its smaller mass. Therefore, attosecond pulses are needed in order to resolve the electronic dynamics.

The generation of attosecond pulses required some new concepts. The main reason is the necessity of an extremely large spectral bandwidth. The uncertainty-principle (also: time-bandwidth product)

$$\Delta E \cdot T_p = 1.83\ \mathrm{eV} \cdot \mathrm{fs}$$ [2]

dictates already a spectral bandwidth of $\Delta E = 10\,\mathrm{eV}$ for a pulse duration of $T_p = 183\,\mathrm{as}$. Due to the low central energy of visible ultrashort pulses (e.g. titanium sapphire: $\sim 1.5\,\mathrm{eV}$) such bandwidths are impossible to achieve, limiting these pulses to the femtosecond regime. Attosecond pulses therefore require the spectral components to be in the ultraviolet or extreme ultraviolet region.

The key concept used for the generation of attosecond pulses is a nonlinear strong-field phenomenon known as high harmonic generation which was discovered in the 1980s [16]. Here, pico- or femtosecond pulses, providing a strong laser field, are up-converted into high-energy photons by the interaction with noble gas atoms. Unlike the well studied perturbative harmonics the spectrum exhibits a pronounced plateau region, in which the harmonics have almost the same intensity. The mechanism was first explained by the semi-classical three-step-model developed by Paul Corkum [17]: The electric field of the ultrashort pulse is sufficiently strong to significantly bend the binding potential of the atom which makes it likely that the valence electron tunnel ionizes. The freed electron is then accelerated in the continuum and may recombine with the ion core when the driving field changes its direction. Upon this process an extreme ultraviolet (XUV) photon is generated corresponding to the sum of the kinetic energy of the electron and the ionic potential. Depending on the time of birth of the electron within the laser cycle it can be shown that different photon energies result. Finally, the appearance of the discrete peaks can be explained by the interference of the electron trajectories generated by the periodic repetition of the process by the driving laser field.

---

[2] This formula assumes a Gaussian spectrum.

This revealing explanation also suggests an attosecond temporal structure of high harmonics which was verified experimentally in 2001 by P. M. Paul and co-workers [6]. Due to the repetition of the process each half-cycle of the driving laser, trains of attosecond pulses are generated. In the following years many successful schemes were developed to isolate a single-attosecond pulse [18,19]. Parallel to this advancements experiments were conducted aiming to resolve the electron dynamics in various systems.

Conducting these experiments involves some difficulties due to the following reasons:

1. The absorption cross-section of air requires the measurements to be done in vacuum.
2. The state-of-the-art XUV flux is still to low to perform true XUV-XUV pump-probe experiments.
3. Almost all materials exhibit strong XUV absorption. Suitable optics such as mirrors therefore need to be specially designed (multilayer mirrors) or used in grazing incidence (metallic mirrors). Beamsplitters and optics for the manipulation of the polarization, in the traditional sense, do not exist.
4. Interferometric pump-probe measurements on attosecond time-scales require the optical setup to provide nanometer stability.

Nevertheless, many clever ideas have been introduced to overcome these challenges.

Today most established attosecond time-resolved methods are based on a two-color pump-probe measurement involving an XUV- and infrared (IR) pulse. There are two types of detectors available for the realization of these experiments: XUV photon spectrometers or charged particle detectors.

Using photon spectrometers attosecond transient absorption experiments can be conducted. Here, the absorption of the XUV spectrum is recorded as a function of the

XUV-IR pump-probe delay. In the first experiment of this kind [20] exciting results were presented uncovering an attosecond delay between the generation of singly- and doubly charged Krypton. Moreover, an electronic coherence between the spin-orbit states was measured for the first time. A range of other work has proven the potential of this method [21,22].

Charged particle spectrometers instead are based on the fact that XUV pulses or intense light fields can ionize atoms or molecules in single- or multi-photon ionization, respectively. The detection of the charged fragments allows then to record the momentum distribution as a function of the pump-probe delay. The most common charged fragment detector is the time-of-flight (TOF) spectrometer [23]. Here, the particles are physically collected within a small solid angle which effectively corresponds to the extraction of a 1D momentum distribution. More advanced spectrometers like the velocity-map imaging (VMI) spectrometer [24] are able to resolve a 2D projection of the momentum distribution.

The above discussion illustrates that the detector crucially determines the type of experiment that can be conducted. In this thesis the attosecond technology has been successfully combined with the COLTRIMS[3] detector. The COLTRIMS device is a spectroscopic apparatus with unique features. It allows for the reconstruction of the full 3D momentum of the charged fragments after a break-up process and offers the possibility to measure the electrons and ions in coincidence, which means that it e.g. enables to assign an electron to its parent ion.

This thesis is structured as follows. In chapter 2 a review about the developments of ultrashort laser pulses is provided. Here, in particular, the laser system used in the scope of this thesis is exemplarily presented.

Chapter 3 reviews the basics of high harmonic generation (HHG) and its connection to attosecond pulses. The single-atom picture given by the three-step-model is introduced, offering the reader a simple interpretation of the high harmonic process. As will be shown, the temporal structure of high harmonics corresponds to attosecond pulse trains (APTs). In this context, the RABBITT[4] technique is discussed as a way to temporally characterize these pulses.

---

[3] cold target recoil ion momentum spectroscopy

Chapter 4 deals with the generation and application of single attosecond pulses which have been used as one of the main tools to carry out the time-resolved studies within this thesis. The most relevant generation techniques are presented and discussed. The principle of the attosecond streaking method will be explained using experimental data. Finally, the FROG-CRAB[5] technique is presented underlining its use for both the temporal characterization of single attosecond pulses and the extraction of time-delays.

Chapter 5 gives an overview of the COLTRIMS apparatus, which has been used to carry out the studies within this thesis. The description includes its principle and the main features exploited for the measurements.

For attosecond single-photon ionization experiments the COLTRIMS has been upgraded with an attosecond front-end providing the possibility to perform attosecond time-resolved measurements using pump-probe schemes. This device is referred to as AttoCOLTRIMS. Chapter 6 gives a review of the AttoCOLTRIMS apparatus developed within this thesis containing all relevant details.

One of the intriguing applications of the AttoCOLTRIMS is the possibility to directly measure the rotating electric field vector of the probing light field in an attosecond streaking experiment. In chapter 7 a sample measurement is presented demonstrating this capability and its possible applications.

Within this thesis the coincidence capability of the COLTRIMS detector has also been used to study photoemission time delays between atomic species. In chapter 8 measurements between valence electrons of argon and neon are presented being in good agreement with theoretical calculations. The results suggest important implications for time-delay extraction in attosecond science.

---

[4] reconstruction of attosecond beating by interference of two- photon transitions

[5] frequency-resolved optical gating for complete reconstruction of attosecond bursts

Chapter 2

Femtosecond laser system for attosecond science

Attosecond science is historically tightly linked to the development of ultrashort pulses in the visible to infrared. Only by the use of these pulses it is today possible to generate attosecond pulses through the process of high harmonic generation (HHG).

It all started with the invention of the laser in 1960 by Theodore Maiman [25]. Since then numerous types of lasers have been developed. Both continuous wave and pulsed lasers have been pushed to their limits. In particular in the 1970s and 1980s pulsed lasers have seen a dramatic development reaching picosecond and femtosecond duration (see Fig. 2.1). Until the end of the 1980s dye lasers [26] were dominating the ultrashort pulse domain. However, in the 1990s their development was slowed down drastically by the 'revolution' of the solid-state lasers overcoming some of their major drawbacks such as the rapid degrading during operation and relatively low output power.

Among the solid-state laser materials the Titanium-sapphire (Ti:sapph) [27] prevailed in many aspects against its competitors due to its exceptional gain cross section and its thermal conductivity. Here, the use of the Kerr-lens-mode locking (KLM) [28] and the chirped mirror technique [29] allowed to achieve pulse durations down to the few-cycle regime corresponding to less then 7 fs at its central wavelength of about 800 nm. A very important step especially for attosecond science was the development of the carrier-envelope-phase (CEP) detection and stabilization. This permits nowadays to use a well-defined (constant) electric waveform of the laser field. More recently a waveform synthesizer based on a spectrally broadened Ti:sapph output was demonstrated allowing arbitrary electric fields and pulse durations down to 2 fs [30]. Besides the Ti:sapph laser optical parametric sources [31] have been of great interest for attosecond science in recent years. Since these sources provide longer wavelength they are well suited not only to generate HH at high photon energies, but also to address many interesting theoretical predictions in strong-field physics. Even though a number of studies have already been performed, these sources are still technically challenging and suffer from relatively low pulse energies and/or repetition rate.

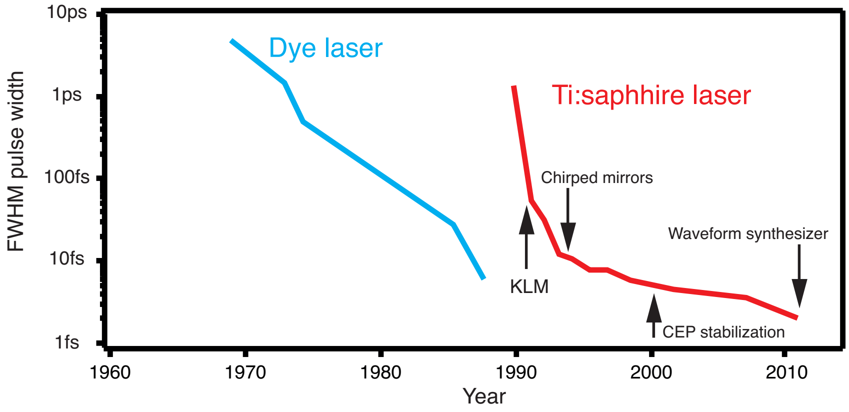

Figure 2.1. Evolution of ultrafast lasers. At the end of the 1980s dye lasers were rapidly replaced by the Ti:sapph laser. Since then the pulse duration has been pushed to its physical limit for central frequencies lying in the visible to infrared.

In this chapter the principle of a CEP stabilized chirped pulse amplifier system is presented as it is used nowadays in many attosecond laboratories. This description is followed by a brief overview about the most common scheme for ultrashort pulse characterization and a section covering details about our hollow-core fiber compression, which is the last major step before the generation of attosecond pulses.

2.1 Few-cycle Ti:sapph laser oscillator

The term oscillator is used to distinguish a pure laser with an optical cavity from a laser amplifier. Due to the low pulse energy output, laser oscillator are usually used in attosecond science as a seed for an amplifier stage. The Ti:saphh crystal is well suited for this purpose: It offers a huge gain bandwidth of about 400 nm spanning from $\lambda = 670 - 1050\,\text{nm}$. Due to the uncertainty principle, this is a necessary requirement to produce few-cycle pulses. However, a broadband spectrum does not necessarily lead to pulse formation. Additionally, the wavelength (frequency) components need to have a well-defined phase relation $\varphi(\omega)$, where $\omega = 2\pi c / \lambda$ is the angular frequency. If all spectral components share the same phase it can be shown that the pulse has the shortest possible time duration which is referred to as the transform limit of the spectrum. A non-linear phase relationship can lead to pulse broadening ($d^2\varphi / d\omega^2 \neq 0$) or to pulse distortion ($d^3\varphi / d\omega^3 \neq 0$). In case of a fixed relationship of all components (modes) the term 'mode locking' is used.

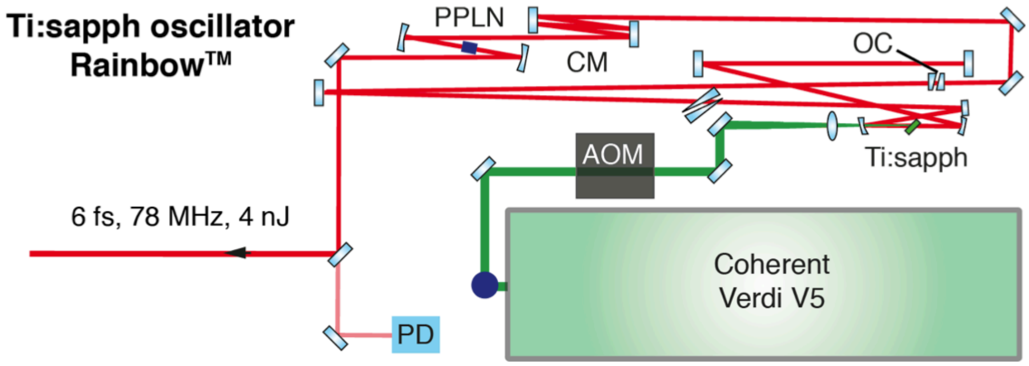

Figure 2.2 Ti:sapph oscillator Rainbow™. The Ti:sapph crystal is pumped with a 532 nm laser (Coherent Verdi V5). After being coupled out via the output coupler (OC) the pulses pass a pair of chirped mirrors (CM) for pulse compression. The AOM, the periodically poled lithium niobate (PPLN) and the photodiode (PD) are part of the CEP stabilization described in section 2.4.

There are active and passive methods to achieve this. In active mode locking the losses inside the resonator are synchronized with the cavity round trip time using an acusto-optic or electro-optic modulator (AOM and EOM, respectively). Pulse formation occurs during the time when the losses are smallest. Other then this, in passive schemes active synchronization is not necessary. There are different passive approaches e.g. the saturable absorber or the Kerr-lens mode locking (KLM). A saturable absorber [32] is an element placed inside the cavity in order to transmit only high intensity laser pulses. Low intensity continuous wave operation is prevented by absorption. An initial random laser spike that may appear is able to start the mode locking process. KLM instead makes use of a nonlinear process: At sufficiently high intensities Kerr-lensing in the gain material starts to play a role which means that the gain medium itself acts as a intensity dependent focusing lens. In the pulsed operation the beam has therefore different divergence. This can be exploited by inserting an aperture, which introduces high losses for continuous wave (cw) and thereby favors pulsed operation. It is even possible to dispense with the aperture altogether by adjusting the pump beam and the laser beam overlap in the gain medium such that it is optimal only for the pulsed operation. Most Ti:sapph lasers are Kerr-lens mode locked.

We use a commercial Kerr-lens mode locked Ti:sapph oscillator from Femtolasers Produktions GmbH which is dubbed Rainbow™ shown in Fig. 2.2. It delivers few-cycle pulses of 6 fs duration at a repetition rate of 78 MHz and pulse energies of about 4 nJ. Moreover, the oscillator is fully CEP-stabilized. In section 2.4 details about the CEP detection and stabilization scheme are described.

2.2 Chirped pulse multipass amplifier

Ultrafast Ti:sapph oscillators are widespread and heavily used for scientific purposes as for example in ultrafast spectroscopy including pump-probe experiments and nonlinear optics. However, in attosecond science pulse energies on the order of microjoules are necessary which are not achievable directly from a laser due to the nonlinear effects and damage threshold of the optics. In 1985 G. Mourou and D. Strickland introduced the concept of the chirped pulse amplifier (CPA) [33]. Instead of scaling the laser to higher energy output they used an additional amplification stage for the laser pulses. Clearly, this would lead to similar problems if the intensity of the seed pulses would remain the same. But the main idea behind it is to temporally broaden (to stretch) the seed pulses by a dispersive material (to chirp) before seeding them into the amplification stage. This allows to reduce the peak intensities to a value that is well below the damage threshold of the amplifier crystal even after the pulses have been amplified. After the amplification, which usually is done in multiple passes, the pulses need to be compressed back. This can be done e.g. with a prism or a grating compressor which essentially reverses the dispersion that was previously introduced by the stretcher.

Even though CPA systems are operated with powerful pump lasers the repetition rate of the oscillator pulses still needs to be reduced in order to amplify the pulse energy from a nanojoule level to milijouls. To this end, a pulse picker is introduced, adjusting the repetition rate of the oscillator (typically MHz level) to the repetition rate of the pump laser which is typically set between a Hz-kHz level.

A major drawback of CPAs is the so called gain narrowing which means that the spectral components of the seed pulses are not amplified by the same amount. Instead, the gain profile has rather a Gaussian shape with a central frequency that is amplified preferentially. This gain narrowing, eventually, leads to reduced spectral bandwidth after amplification and, therefore, to pulse broadening even with a perfect compression stage. Typically, the pulse duration of a CPA system lies around 30 fs with central wavelength of 790 nm.

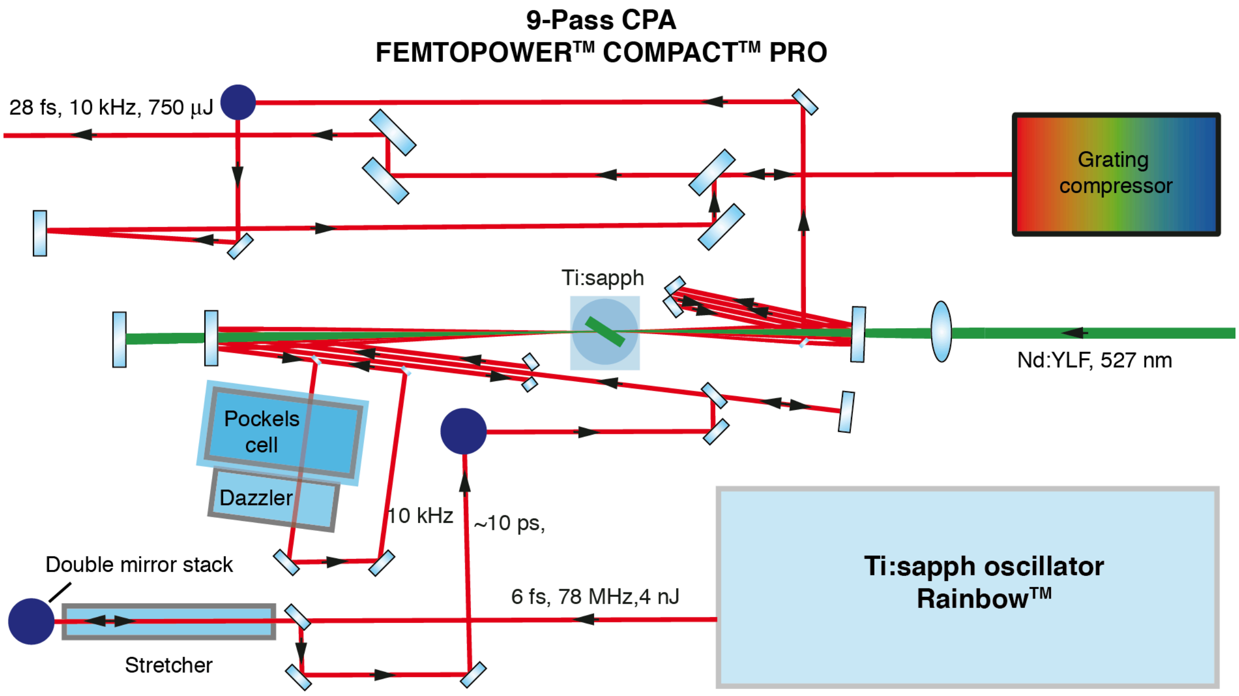
9-Pass CPA
FEMTOPOWER™ COMPACT™ PRO
28 fs, 10 kHz, 750 µJ
Grating compressor
Ti:sapph
Nd:YLF, 527 nm
Pockels cell
Dazzler
10 kHz
~10 ps,
Double mirror stack
6 fs, 78 MHz,4 nJ
Ti:sapph oscillator
Rainbow™
Stretcher

Figure 2.3. Simplified illustration of the commercial multipass amplifier system. The amplifier is seeded with the Rainbow™ oscillator described in section 2.1. After 9 amplification passes through the Ti:sapph crystal, pulses of 28 fs duration and 750 µJ pulse energy at a repetition rate of 10 kHz are generated. A detailed description can be found in the text.

Figure 2.3 shows a simplified scheme of the commercial multipass amplifier that is used for our experiments (FEMTOPOWER™ COMPACT™ PRO, Femtolasers Produktions GmbH). The oscillator pulses pass a dispersive bulk material leading to about 10 ps pulses. These pulses are amplified by 9 passes through a Ti:sapph crystal pumped with a Nd:YLF laser at 527 nm and about 80 W average power. The pump laser is operated in pulsed mode with a repetition rate of 10 kHz. In order to adjust the repetition rate of the oscillator pulses to the repetition rate of the pump a pulse picker (PC: Pockels Cell) is introduced before the 5th pass. Finally, after the 9th pass the beam is picked up and compressed in a transmission grating compressor. Since such compression techniques cannot compensate for higher order dispersion, which is generally introduced through the dispersive optics, the pulses are not transform limited. In order to compensate for this effect a so-called dazzler (FASTLITE) is installed after the PC. This device is a commercial ultrafast pulse shaper. It is able to introduce arbitrary dispersion by the modulation of the parameter of an acoustic wave applied to a crystal. Therefore, it is well suited to compensate for the residual chirp. The amplifier output finally delivers nearly transform limited pulses of 28 fs and $750\,\mu\mathrm{J}$ at a repetition rate of 10 kHz.

2.3 Carrier-envelope-phase stabilized CPA

The electric field of a light pulse is described by

$$\boldsymbol{E} = \boldsymbol{E}_0 f(t) \cos(\omega t + \varphi_{\mathrm{CEP}}).$$

Here, $\boldsymbol{E}$ is the electric field, $\boldsymbol{E}_0$ is the amplitude of the oscillation, $f(t)$ describes the envelope, ω is the carrier-frequency and φ_{CEP} is the CEP. According to this description, the CEP can be interpreted as the phase of the electric field oscillation with respect to the peak of the pulse envelope which eventually determines the waveform of the pulse. The pulses generated from a free-running laser oscillator exhibit pulse-to-pulse CEP fluctuation caused by several sources of noise, ranging from temperature- and air pressure changes or vibrations (low frequency) to pump laser intensity fluctuations (high frequency).

However, it is possible to stabilize the CEP of the output pulses. The Rainbow™ oscillator that has been used within this thesis employs a feedback scheme. Here, the output pulses are frequency doubled in a periodically poled lithium niobate (PPLN) crystal. Since the fundamental laser is octave spanning, the fundamental and the frequency doubled pulses have spectral components that overlap. These components generate difference frequencies (DFG) in the PPLN which can be detected using a photodiode (PD) illustrated in Fig. 2.2. It can be shown that this signal is proportional to the CEP [34]. A feedback scheme can now be applied in order to stabilized the signal. There are different approaches to induce CEP changes, e.g. the modulation of the pump power which is used in our case. To this end, an AOM is placed in the pump beam path. An error signal, generated by the comparison of the detected DFG with a reference frequency, is fed into the AOM allowing for fast correction of the CEP.

The short term CEP stability is maintained even after the amplification stage. Nevertheless, a residual long-term CEP drift is observed, which is primarily caused by the pointing instability of the seed beam. This leads to CEP changes since the beam travels through slightly different amount of dispersive material. In order to compensate for these slow changes, a commercial f-2f interferometer detection scheme (APS800, Menlo Systems) is placed after the amplifier. The error signal is then fed to an element that is able to change the CEP of the pulses. In our case it is a motorized prism pair integrated into the stretcher (see Fig. 2.3) of the amplifier. Applying the feedback signal to the piezo motor allows for changing the thickness of the prism pair and thereby the dispersion. With this approach the CEP of the amplified pulses can be stabilized down to 100 mrad root-mean-square (RMS) for several hours.

2.4 Temporal characterization of ultrashort pulses

The characterization of the temporal structure of laser pulses gets more challenging the shorter the pulses are. For pulse durations longer then about 20 ps this can still be done electronically using high-speed photodiodes and sampling scopes. For shorter pulses new schemes have been developed in the last decades. Today, among these the intensity autocorrelation [35], Frequency-Resolved Optical Gating (FROG) [36] and the Spectral Phase Interferometry for Direct Electric-field Reconstruction (SPIDER) [37] are the most established methods.

The principle of the second-harmonic generation (SHG) intensity autocorrelator is depicted in Fig. 2.4 (a). The pulses to be characterize enter a beam-splitter. One split part can be delayed with respect to the other by the adjustment of a delay stage. A lens is used to focus both beams into a nonlinear crystal that allows to induce sum frequency generation (SFG) if both pulses have a significant overlap. In order to determine the pulse duration the SFG signal (blue) is recorded with a photodiode (PD) as a function of the delay of both pulses. A characteristic signal can be detected on a sampling scope according to

$$I_{\text{SHG-auto}}(\tau) = \int P(t)P(t-\tau)\,dt\,, \tag{1.1}$$

where τ is the delay between both pulses. The pulse P(t) can only be determined when a certain pulse shape is assumed. For a Gaussian pulse profile the pulse duration is given by $1/\sqrt{2}$ the duration of the intensity autocorrelation signal. The autocorrelation technique is a powerful tool for a rough but reliable estimation of the pulse duration. However, it generally fails to determine the detailed pulse structure.

The setup of a SHG FROG device is very similar to an intensity autocorrelator. A schematic is shown in Fig. 2.4 (b). The main difference is the substitution of the PD with an optical spectrometer. The FROG technique therefore records spectra as function of time delay τ between the two pulses. Typical FROG spectrograms are pseudocolor representations of the time-frequency plots which are mathematically described by

$$I_{\text{SHG-FROG}}(\omega,\tau) = \left|\int E(t)E(t-\tau)\exp(-i\omega t)\,dt\right|^2\,, \tag{1.2}$$

where E(t) is the complex electric field of the pulse to be measured and ω is the angular frequency of the spectral components. The spectrogram contains unambiguously the information of the phase of the pulse and offers even redundant information that can be used for sanity checks. The most common way to extract the pulse duration (or phase of the pulse) from a FROG measurement is to use the generalized projection algorithm [38]. This is a powerful iterative method that reproduces the measured spectrogram using equation (1.2) and thereby determines the pulse field $E(t)$.

The SPIDER technique is based on a rather different approach then the other methods discussed above. Its principal setup is depicted in Fig 2.4 (c). The pulses to be measured enter an optical arrangement that allows to produce two beams, where one contains two replica of the pulse with a well defined temporal distance and the other containing only one replica. This can be done for instance by using an etalon. The single pulse beam then passes an element that introduces strong spectral dispersion (e.g. a thick bulk material). The two replica and the dispersed pulse are subsequently focused into a nonlinear crystal for SFG. As in the case of FROG the SFG signal is analyzed with a spectrometer but here, recorded without a delay scan.

(a) SHG intensity autocorrelator

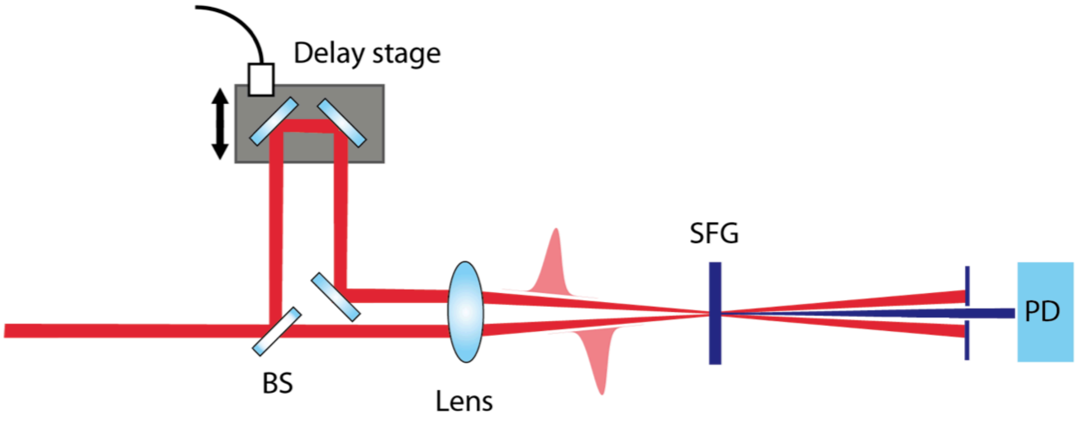
Delay stage
SFG
PD
BS
Lens

(b) SHG FROG

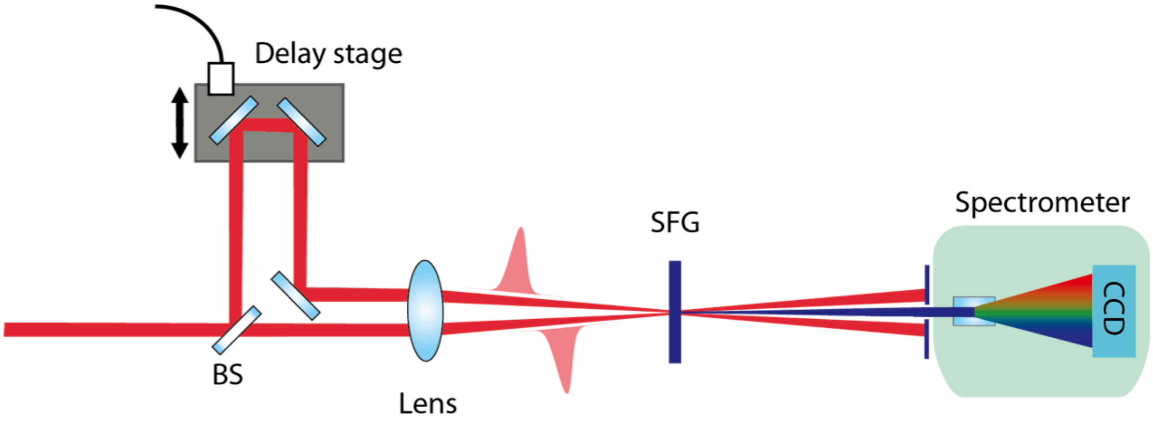
Delay stage
Spectrometer
SFG
CCD
BS
Lens

(c) SPIDER

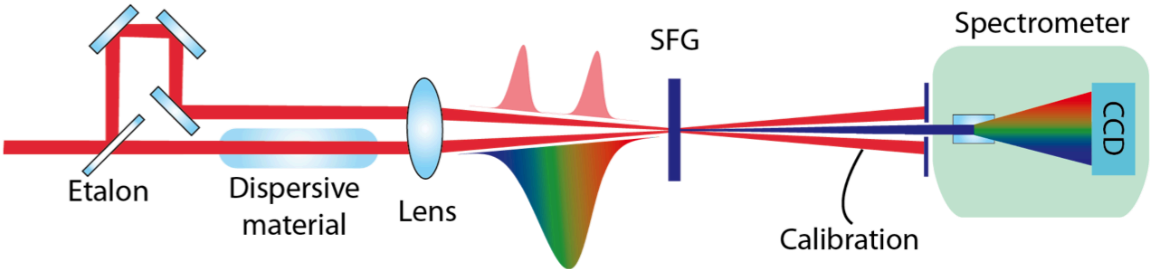
Spectrometer
SFG
CCD
Etalon
Dispersive material
Lens
Calibration

Figure 2.4. The most established schemes for the temporal characterization of ultrashort laser pulses. Details can be found in the text.

The extraction of the pulse duration i.e. the phase of the pulse relies on the so-called spectral shear interferometry: SFG occurs for each of the two pulses. But since the third replica is chirped the two others are up-converted with different frequencies. The spectral distance (shear) Ω between these components can be calculated by the known dispersion of the stretcher and the central wavelength of the pulse to be measured. The signal originating from the spectral interference of the up-converted pulse replica which is observed on the spectrometer is given by

$$\begin{aligned} I_{\mathrm{SPIDER}}(\omega) = {} & |E(\omega)|^2 + |E(\omega+\Omega)|^2 + \\ & + 2|E(\omega)||E(\omega+\Omega)|\cos\left[\varphi(\omega+\Omega) - \varphi(\omega) + \omega\tau\right] \end{aligned}, \tag{1.3}$$

where $E(\omega)$ is the spectral representation of the pulse. The oscillating term can be isolated by applying a Fourier filter. In order to access the phase difference $\varphi(\omega+\Omega)-\varphi(\omega)$, the $\omega\tau$ phase term needs to be eliminated. This procedure is referred to as the calibration which can be done by measuring the SFG of the two unsheared replica (see Fig. 2.4 (c)). Finally, the phase can be extracted by the standard concatenation procedure, setting e.g. the phase at the first frequency component ω_1 to zero.

In the scope of this thesis the SPIDER technique has been used to characterize the ultrashort pulses used for the attosecond pulse generation.

2.5 Hollow-core fiber compression stage

As already discussed in section 2.3 a CPA system suffers from gain narrowing. This limits amplifier pulses to pulse durations above 20 fs. However, in strong-field physics few-cycle pulses (<7 fs at 800nm) are of great interest since they offer many applications. This calls for a further compression stage. A common scheme is the use of self-phase modulation (SPM) [39] which is a nonlinear interaction of the ultrashort pulses with a medium. Through this process new frequency components are generated appearing symmetrically on either side of the spectrum. This potentially allows to compress the pulses.

There are essentially two different SPM compression schemes: The hollow-core fiber (HCF) [40] and the filament compression [41] technique. In the first case the amplifier pulses are coupled into a noble gas filled hollow-core fiber of typically 1 m length.

The fiber serves as a guide allowing for a strong interaction over a long distance. In the second case the pulses are simply loosely focused into a 1-2 m long gas cell which is also filled with a noble gas. Here, instead a so-called filament channel builds up providing the necessary strong interaction. The formation of this channel is explained by the counter acting processes of Kerr-type focusing and plasma defocusing leading to a strong confinement over a several tens of cm.

In both of the schemes the spectrally broadened pulses then need to be properly compressed in order to compensate the chirp introduced by the interaction with the gas and the optical windows used for the gas cell. Neither a grating nor a prism compressor are capable to compress such broadband spectra since both introduce significant higher-order dispersion. The common approach is the use of dispersive mirrors (also known as chirped mirrors). These dielectric mirrors are based on the different penetration depth of the spectral components. This concept allows to correct for the phase differences between the spectral components.

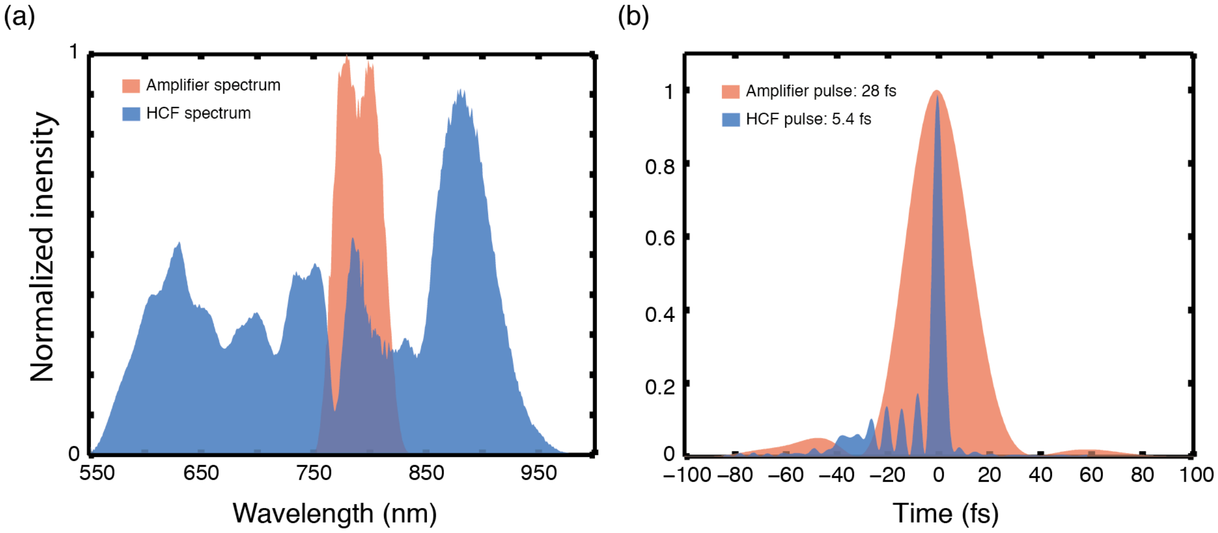

Figure 2.5. Hollow-core fiber compression. In (a) the spectra of the amplifier and the hollow-core fiber (HCF) using are presented. The spectral broadening has been achieved through SPM inside the HCF which was filled with 2.5 bar of Ne. Using the SPIDER technique the pulses were temporally characterized as shown in (b).

The scheme employed within this thesis is the HCF technique. We use a HCF with an inner diameter of 250 μm . In order to generate few-cycle pulses we fill the HCF with neon (Ne) at a pressure of about 2.5 bar. The spectrum of the amplifier pulses before the HCF and the spectrum at the output of the HCF for 2.5 bar of Ne are shown in

Fig. 2.5 (a). For the adjustment of the phase and for the pre-compensation of the chirp introduced by the optics before the experiment we use a set of 12 chirped mirrors (UltraFast Innovations GmbH, PC70). These mirrors are designed to compensate the chirp of the HCF setup and to pre-compensate 6 m of air as well as 6 mm of fused silica material. The characterization of the pulse duration is shown in Fig. 2.5 (b). Both measurements have been performed with the SPIDER method. The amplifier pulses have a FWHM of 28 fs. After the HCF compression we measure a FWHM of 5.4 fs with some slight satellites originating from uncompensated third-order dispersion.

Chapter 3

High harmonic generation

The interaction of intense laser fields with matter gives rise to nonlinear effects. This was shown soon after the first realization of the laser through the demonstration of second harmonic generation in a bulk crystal by Franken et al. [42]. The mechanism can be understood within perturbation theory where the polarization density of the medium is not directly proportional to the applied electric field of the laser. Instead it can be expanded in a Taylor series containing non-negligible quadratic and higher order dependence on the electric field. One of the important implications for such perturbative harmonics is their strongly decreasing yield with increasing order. In 1987 McPherson and co-workers studied the generation of harmonics in rare gases [16] and observed a rather different behavior (see Fig. 3.1): At low orders the harmonic yield follows the expected perturbative behavior while observing an almost flat yield (plateau) in the intermediate spectral region followed by a steeply falling high energy part. This unexpected discovery was explained in 1993 by Corkum et al. [17] in a semi-classical picture which is known as the three-step model.

The harmonics observed in the plateau were called high harmonics (HH). It took almost one decade until it was experimentally shown that these HH have a well defined phase relation corresponding to a train of attosecond pulses (APT) [6]. Already shortly after these measurements the isolation of single attosecond pulses (SAP) was demonstrated [43]. These breakthroughs were the starting point of attosecond time-resolved measurements at the beginning of the 2000s. Since then the unprecedented time resolution has been used to unravel the dynamics of electrons in atoms and molecules [44,45]. More recently the study of attosecond dynamics has also been extended to metal surfaces and condensed matter systems [3,46].

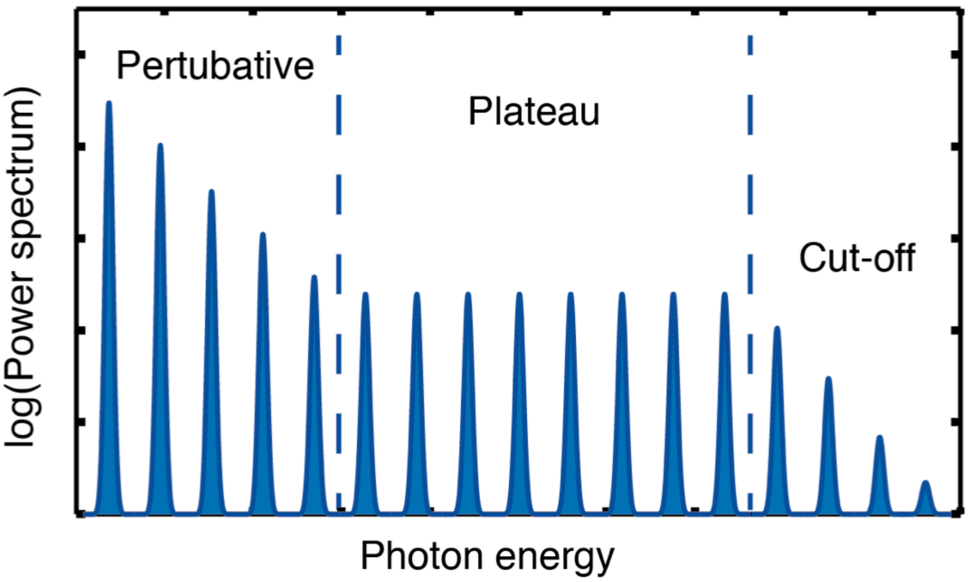

Figure 3.1. Simplified illustration of the characteristic HH spectrum. On the left side a steep decrease of the harmonic yield is observed corresponding to the classical perturbative regime. In the middle part a plateau appears which cannot be explained in the perturbative picture. The right part in which the yield drops is called the cut-off of the spectrum.

In this chapter the mechanism behind high harmonic generation is explained by introducing the three-step which resolves the most important observed features. However, the microscopic picture of the three-step model does not explain all the details in the HH spectrum. The subsequent section is therefore dedicated to the macroscopic response. In the temporal domain HHs correspond to a attosecond pulse train. Therefore, the last two sections adopt the time domain picture linked to HHs.

3.1 Semi-classical three-step model

In 1993 Paul Corkum introduced a semi-classical model [17] which is able to explain some of the most prominent features of high harmonic generation (HHG). Since the model suggests to divide the process in three different parts it is also well known as the three-step model or sometimes also simple man's model. Corkum assumes a quasi-static picture of the ionization process in which the tunneling time is considered to be much shorter then the cycle time of the ionizing field.

In the following, details of each step are described and the most important consequences are highlighted. In this context Fig. 3.2 provides a schematic illustration visualizing the process underlying the HHG.

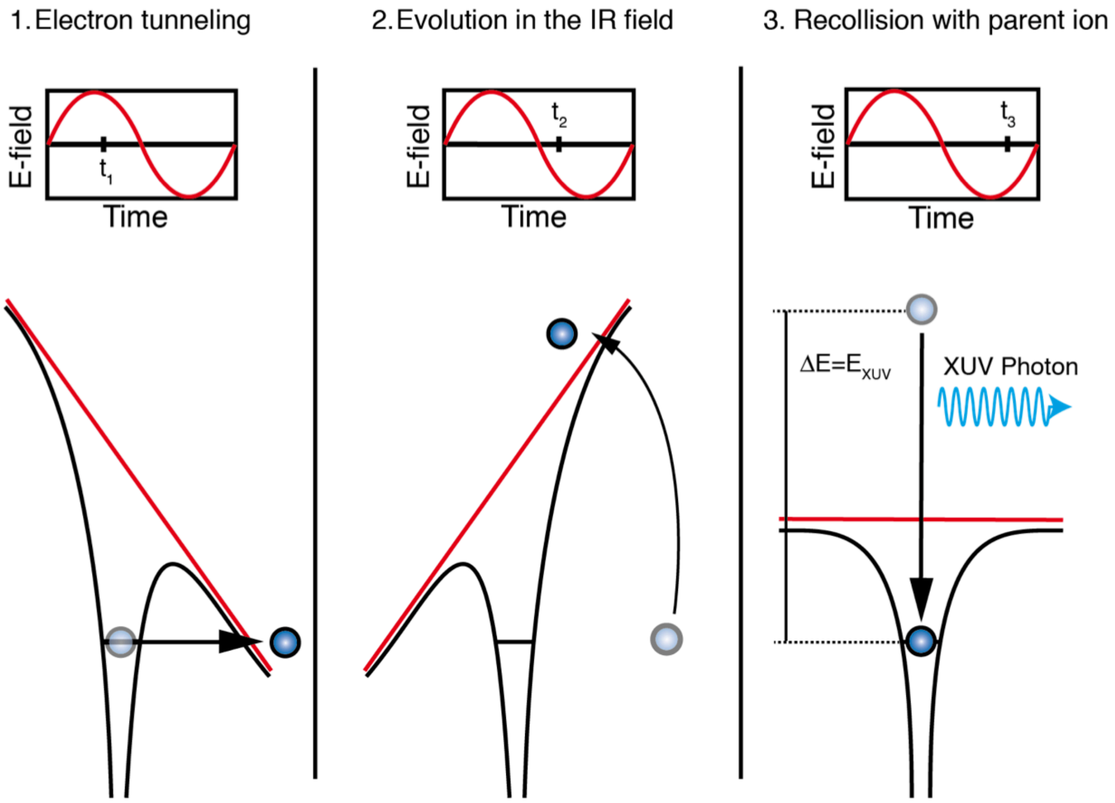
1. Electron tunneling
2. Evolution in the IR field
3. Recollision with parent ion
E-field
Time
t_1
t_2
t_3
ΔE=E$_{XUV}$
XUV Photon

Figure 3.2. Three-step model for HHG. Left panel: The IR field bends the ionic potential allowing for the electron to tunnel ionize. Middle panel: The IR field has changed sign, accelerating the electron back to the core. Right panel: The electron reaches the position of the ion core and hence recombines with it. Upon this process a photon is emitted. For details see text.

1) In the first step the IR ionizes the electron through tunnel ionization. The probability of ionization is calculated from the so-called Ammosov-Delone-Krainov-rate (ADK-rate) [47] W_{dc} which already assumes the quasi-static approximation

$$W_{\mathrm{dc}} = \omega_{\mathrm{S}} \left| C_{\mathrm{n}^{*}\mathrm{l}^{*}} \right|^{2} G_{\mathrm{lm}} \left(4\omega_{\mathrm{S}} / \omega_{\mathrm{t}} \right)^{2\mathrm{n}^{*}-\mathrm{m}-1} \exp(-4\omega_{\mathrm{S}} / 3\omega_{\mathrm{t}}), \tag{1.4}$$

where

$$\omega_{\mathrm{S}} = V_{\mathrm{S}}^0 / \hbar,$$
$$\omega_t = eE\left(2m_{\mathrm{e}}V_{\mathrm{S}}^0\right)^{1/2},$$
$$n^* = \left(V_{\mathrm{S}}^{\mathrm{h}} / V_{\mathrm{S}}^0\right)^{-1/2},$$
$$G_{lm} = (2l+1)(l+|m|)!\left(2^{-|m|}\right)/|m|!(l-|m|)! \text{ and}$$
$$\left|C_{n^*l^*}\right|^2 = 2^{2n^*}\left[n^*\Gamma\left(n^*+l^*+1\right)\Gamma\left(n^*-l^*\right)\right]^{-1}.$$

Here, V_{S}^0 is the ionization potential of hydrogen, l and m are the orbital angular momentum and magnetic quantum numbers and E is the electric field magnitude. The effective quantum number l^* is zero for $l << n$ and else $l^* = m^* - 1$. The ionization probability at a given time t in the interval dt is then determined by $W_{\mathrm{dc}}\left[E(t)\right]dt$. Since $E(t)$ is an oscillatory function in time the ADK-rate implies the generation of electron wave packets whenever $E(t)$ reaches its extremum without any delayed response.

2) In the second step the freed electron is treated classically as a point charge with initial velocity and position 0. The electron experiences the electric field of the IR

$$\boldsymbol{E}(t) = E_0\cos(\omega t)\boldsymbol{e}_x + \alpha E_0\sin(\omega t)\boldsymbol{e}_y. \tag{1.5}$$

Using Newton's equation of motion allows to determine the position

$$x = x_0\left[-\cos(\omega t)\right] + v_{0x}t + x_{0x}, \quad y = y_0\left[-\sin(\omega t)\right] + v_{0y}t + x_{0y} \tag{1.6}$$

and the velocity

$$v_x = v_0\sin(\omega t) + v_{0x}, \quad v_y = -\alpha v_0\cos(\omega t) + v_{0y}, \tag{1.7}$$

where the parameter α has been introduced to account for different possible IR polarization (linear polarization $\alpha = 0$ and circular polarization $\alpha = \pm 1$), $v_0 = qE_0 / m_e\omega$, $x_0 = qE_0 / m_e\omega$ and $x_{0x}, x_{0y}, v_{0x}, v_{0y}$ are given by the initial conditions.

3) In the third step the recombination of the electron with the parent ion is analyzed. If the IR polarization is linear along x and the electron is born at time t_0 we can rewrite equations (1.6) and (1.7)

$$x = x_0\left[\cos(\omega t_0) - \cos(\omega t)\right] + x_0\omega\sin(\omega t_0)(t_0 - t), \quad y = 0 \tag{1.8}$$

$$v_x = v_0\left[\sin(\omega t) - \sin(\omega t_0)\right], \quad v_y = 0. \tag{1.9}$$

Those electron trajectories that reach $x = 0$ will recollide with the ion and thereby emit a photon with an energy corresponding to the sum of its kinetic energy accumulated in the IR-field and the ionic potential. These photons are those observed as odd HHs of the fundamental field. Figure 3.3 (a) shows an illustration of the electron trajectories for different initial ionization time (blue and green). Depending on the time of birth within the IR cycle, the electron is either driven back to its parent ion (blue trajectories) giving rise to HHG or it will miss the ion (green trajectories). Overall, in this classical picture half of the trajectories eventually recombine.

The equation (1.8) has no analytic solution for $x = 0$. An explicit expression that connects the ionization time t_0 to the recombination time t_{Rec} therefore cannot be deduced. However, there is still an intuitive geometric solution to the equation

$$x_0\left[\cos(\omega t_0) - \cos(\omega t)\right] + x_0\omega\sin(\omega t_0)(t_0 - t) = 0. \tag{1.10}$$

We can rewrite equation (1.10) as

$$\cos(\omega t) = \frac{d}{dt}\left[\cos(\omega t)\right]_{t=t_0} \cdot (t - t_0) + \cos(\omega t_0). \tag{1.11}$$

The left side of the equation (1.11) is proportional to the electric field where the right side expresses the equation of the tangent of the electric field at the time of birth of the electron t_0. This allows for an elegant way to solve equation (1.11) as shown in Fig. 3.3 (b): The tangent at the time of birth may cross the electric field oscillation at another time t_{Rec} which is then the recombination time, solving the equation. Some important implication can be seen directly from this (here only discussed for the first half cycle): Electrons born at the maximum of the electric field have largest recombination time which amounts to one full cycle. Electrons born shortly before $t = T/4$ have shortest recombination times. And finally, as also illustrated in Fig. 3.3 (b) electrons born in the interval $T/4 < t_0 < T/2$ do not recombine.

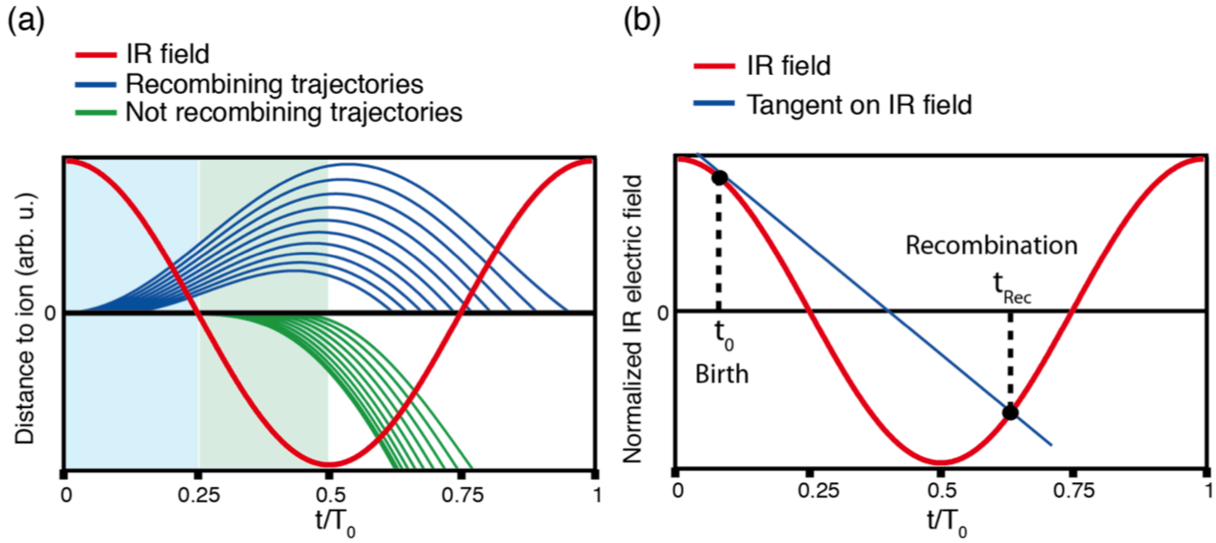

Figure 3.3. Electron trajectories in HHG. (a) Illustration of the electron trajectories after ionization. Those trajectories which eventually recombine with the ion core are shown in blue while the non-recombining ones are represented in green. (b) The recombination time of the electron can be determined by the tangent at the time of birth.

The three-step-model also reveals interesting information derived from the analysis of the kinetic energies of the recombining electron

$$E_{\mathrm{kin}} = \frac{1}{2} m_{\mathrm{e}} v^2 = 2 \cdot U_{\mathrm{p}} \left[\sin\left(\omega t_{\mathrm{Rec}}\right) - \sin\left(\omega t_0\right) \right]^2, \tag{1.12}$$

where $U_{\mathrm{p}} = (eE)^2 / (4 m_{\mathrm{e}} \omega^2)$ is the ponderomotive energy. The lack of an explicit expression that connects t_{Rec} and t_0 also prevents an analytic solution of (1.12) that would only depend on the time of birth. Nevertheless, an analytic expression can be derived by a fitting procedure. This has been done in [48] retrieving

$$t_{\mathrm{Rec}} / T = 1/4 - 3/2\pi \sin^{-1}\left(4 t_0 / T - 1\right). \tag{1.13}$$

Using equation (1.12) and (1.13) the kinetic energy of the electron can be plotted as a function of the time of birth. This is presented in Fig. 3.4. Two main conclusion can be drawn from this graph: Firstly, the highest return energy of the electron is given by $3.17 \cdot U_p$. The HH spectrum therefore is expected to extend to the cut-off energy

$$E_{\mathrm{cutoff}} = I_p + 3.17 \cdot U_p, \tag{1.14}$$

where I_p is the ionization potential of the atomic species used for the HHG. Equation (1.14) implies that the cut-off energy scales quadratically with the driving laser wavelength ($U_\mathrm{p} \sim \lambda^2$). This is the reason why many research groups have started extensive work on the development of long wavelength ultrashort high energy sources such as optical parametric amplifiers (OPAs).

Secondly, there are always two different trajectories leading to the same final energy called short- and long trajectories according to their excursion time. In section 3.3 we will also discuss how the long trajectories can be suppressed. This is favorable since the coexistence of both trajectories distorts the temporal structure of the attosecond pulses.

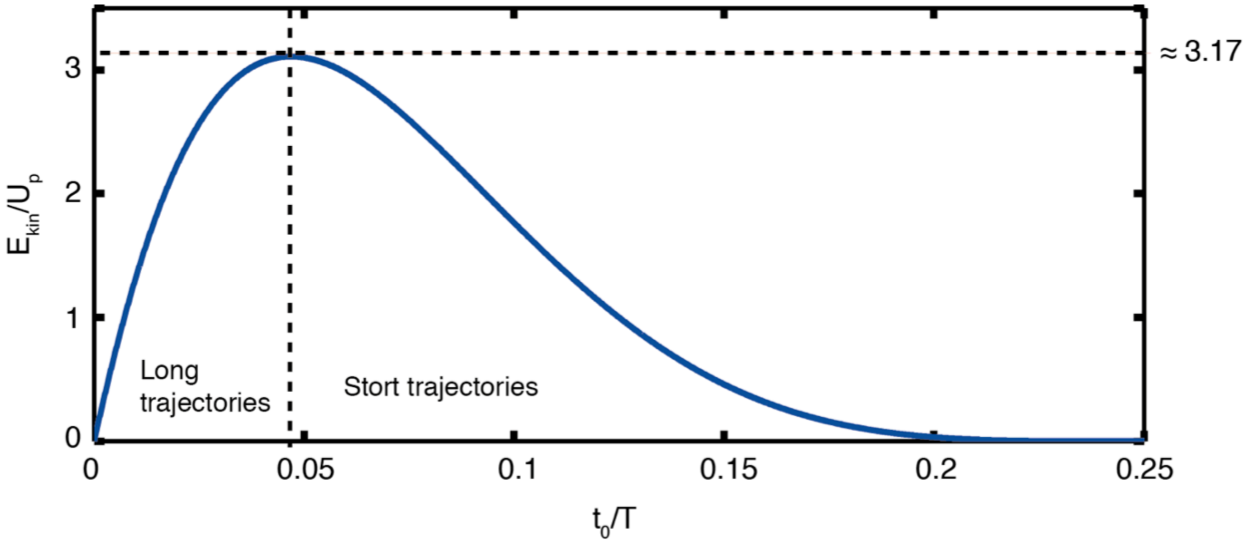

Figure 3.4. Return energies of the recombining electrons as a function of time of birth within the cycle. Two types of trajectories are generated (short and long trajectories) leading to the same final kinetic energy. The distribution shows a characteristic maximum of $3.17 \cdot U_\mathrm{p}$ which is referred to as cut-off energy.

3.2 Macroscopic response

The three-step-model deals with the atomic response due to the exposure of the light field known as the single atom or microscopic response. In order to model the overall harmonic yield in an experiment one needs to consider the effects of the whole ensemble of atoms in the gas target which is referred to as the macroscopic picture [49]. If propagation effects are neglected, the field strength of the q$^{\mathrm{th}}$ harmonic is given by the coherent sum of the signals produced by all the individual atomic emitters that are present in the (gas) target

$$N_{\text{out}} \sim \left| \int_{-\infty}^{\infty} \rho A_{\text{q}}(t)\,dt \right|^2 , \tag{1.15}$$

where $A_{\text{q}}(t)$ is the single atom response and ρ is the particle density. However, for a correct modeling of the process propagation effects have to be included: First, there will be always absorption of radiation along the propagation length L_{med} described by the absorption length L_{abs}. Second, a phase mismatch Δk between the harmonic radiation and the driving field

$$\Delta k = qk - k_q \tag{1.16}$$

can occur (see Fig. 3.5), where $k = 2\pi n / \lambda$ is the wave vector of the driving field, $k_q = 2\pi q n_q / \lambda$ is the wave vector of the q$^{\text{th}}$ harmonic and n, n_q are the respective indices of refraction. Constructive interference of the signals is only ensured for zero phase mismatch.

Taking the propagation effects into account, the overall harmonic yield for the q$^{\text{th}}$ harmonic is then given by

$$N_{\text{out}} \sim \left| \int_{-\infty}^{\infty} \int_{0}^{L_{\text{med}}} \rho A_{\text{q}}(t) \exp\left(-z / L_{\text{abs}}\right) \exp\left(iz / L_{\text{coh}}\right) dt\,dz \right|^2 , \tag{1.17}$$

where $L_{\text{coh}} = \pi / \Delta k$ is the coherence length accounting for the wave vector mismatch Δk and z is the direction of propagation.

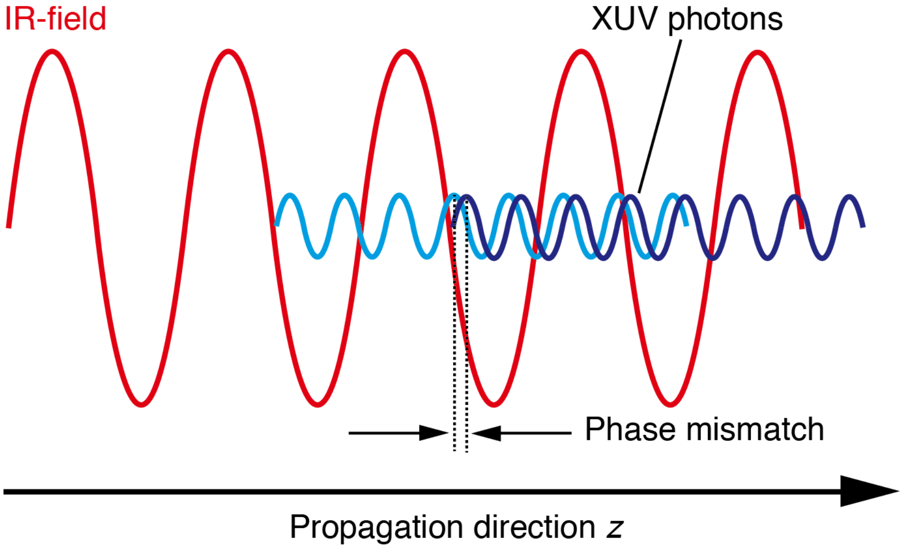

Fig 3.5. Illustration of the phase mismatch between emitted harmonic radiation. As the IR field propagates through the medium, harmonics at different positions are generated. Due to the difference in the refractive indices of the ionized medium for the IR and harmonic field, a phase mismatch can occur leading to a decrease of the harmonic yield.

The coherence length (or phase mismatch) can be calculated with the refractive index for a partially ionized gas [50]

$$n = 1 + P\left[(1-\kappa)\delta(\lambda) - \eta N_{\mathrm{Atm}} r_e \lambda^2 / 2\pi\right], \tag{1.18}$$

where $\lambda, \kappa, P, N_{\mathrm{atm}}, r_{\mathrm{e}}, \delta(\lambda)$ represent the fundamental wavelength, ionization fraction, gas pressure in atmospheres, atomic number density at one atmosphere, the classical electron radius and the neutral gas dispersion.

For the wave vector of the fundamental laser it follows therefore

$$k = \frac{2\pi}{\lambda} + \frac{2\pi P(1-\kappa)\delta(\lambda)}{\lambda} - P\kappa N_{\mathrm{atm}} r_{\mathrm{e}} \lambda . \tag{1.19}$$

The wave vector k_{q} for the q$^{\mathrm{th}}$ harmonic is determined by the substitution $\lambda \to \lambda / q$. The intrinsic phase mismatch originating from the difference in the refractive indices is hence given by

$$\Delta k_{\mathrm{int}} = qk - k_{\mathrm{q}} = \underbrace{P\kappa N_{\mathrm{atm}} r_{\mathrm{e}} \lambda (1/q - q)}_{\Delta k_{\mathrm{plasma}}} \underbrace{- 2\pi P(1-\kappa)\left(\delta(\lambda/q) - \delta(\lambda)\right) q/\lambda}_{\Delta k_{\mathrm{neutral}}} \tag{1.20}$$

containing a plasma and a neutral contribution.

Note that the parameters on which Δk_{int} depends are often linked via macroscopic effects. For instance the harmonic order and the ionization fraction cannot be tuned independently.

Despite the intrinsic there is also a geometric mismatch induced by the Gouy phase shift along the focus of the beam which amounts π over the whole focal range:

$$\phi_{\text{Gouy}} = \arctan\left(\frac{z}{z_0}\right) \approx \frac{z}{z_0} = \frac{\lambda z}{\pi w^2}, \tag{1.21}$$

where λ is the wavelength of the driving field, w is the $1/e^2$ beam radius and z is the distance to the focus along the propagation. Hence, the phase mismatch due to the Gouy phase is given by

$$\Delta k_{\text{Gouy}} \approx \frac{\lambda / q}{\pi w^2} - \frac{q\lambda}{\pi w^2} \approx -\frac{q\lambda}{\pi w^2}. \tag{1.22}$$

The contributions to the total phase mismatch are then

$$\Delta k = \Delta k_{\text{plasma}} + \Delta k_{\text{neutral}} + \Delta k_{\text{Gouy}}. \tag{1.23}$$

The plasma phase mismatch adds a positive and both the neutral and the Gouy phase mismatches add negative contributions. For low ionization fractions one usually tries to balance the net intrinsic with the geometrical phase mismatch. The optimizing criteria $L_{\text{med}} > 3L_{\text{abs}}$ and $L_{\text{coh}} > 5L_{\text{abs}}$ introduced by Constant et al. [51] ensure that the macroscopic response is more than half the maximum reachable (corresponding to $\Delta k = 0$). However, as the ionization fraction increases with intensity, the plasma dispersion becomes too large to be compensated for by the geometrical contribution alone and the optimizing conditions cannot be fulfilled anymore.

3.3 Attosecond pulse trains

The temporal characteristics of HHs are not accessible by established classical techniques known from ultrafast optics such as intensity autocorrelation, FROG or

SPIDER (see chapter 2). This is mostly due to the lack of sufficient photon flux which is necessary to measure nonlinear interaction involving a two photon process.

However, there has been a great interest in the temporal characterization of HHs. The three-step-model itself suggests the possibility of a sub-femtosecond pulse structure of the HHs since in the HH process recombination occurs in less then a half-cycle of the IR.

If the HHs were emitted in phase, a train of attosecond pulses would be expected. Early theoretical studies [52] demonstrated that the contribution from long- and short trajectories are not in phase, preventing the production of attosecond pulses. However, it was also shown that this problem can be overcome by properly placing the target position with respect to the focus of the driving laser.

Ultimately, in 2001 Paul et al. [6] succeeded to experimentally demonstrate the attosecond nature of the HHs. They applied a pump-probe method using the HHs and a delayed IR field[6]. Paul and co-worker were able to show that the mean full width at half maximum (FWHM) pulse duration was about 250 as. This technique is nowadays well established and known as the Reconstruction of Attosecond Beating By Interference of Two- photon Transitions (RABBITT) which is the topic of the next section.

3.4 The RABBITT technique

The principle of the RABBITT method is shown in Fig. 3.6 (a). A HH beam is focused onto an atomic target. Since the HHs have photon energies above the ionization threshold this will excite the ground state electrons into the continuum. The electrons that are created can be measured using different techniques such as a time-of-flight (TOF) spectrometer, a velocity-map-imaging spectrometer (VMIS) or the cold target recoil ion momentum spectroscopy (COLTRIMS) technique. The electron spectrum will mostly resemble the XUV spectrum being only shifted in energy by the ionization potential of the atomic species. Now if we add a moderately strong IR on the order of $10^{10}\,\mathrm{W/cm^2}$, overlapping in time and space, a signal between two consecutive odd harmonic appears in the electron spectrum. This signal is called sideband (SB) and is found to oscillate with varying XUV-IR delay. As the total electron counts are only created by the HHs they have to stay constant even if SBs are created. SB creation will therefore always lead to depletion of the HH bands.

---

[6] The RABBITT method was already proposed in [53] V. Véniard, R. Taïeb, and A. Maquet, Physical Review A **54** (1996).

A typical RABBITT spectrogram, here measured with our COLTRIMS detector, is shown in Fig. 3.6 (b). As can be seen, e.g. the SB18 (that was already highlighted in (a)) oscillates as a function of the XUR-IR delay. The neighboring HH signals are oscillating as well due to the depletion process described above. The frequency of the oscillation turns out to be twice the frequency of the IR laser.

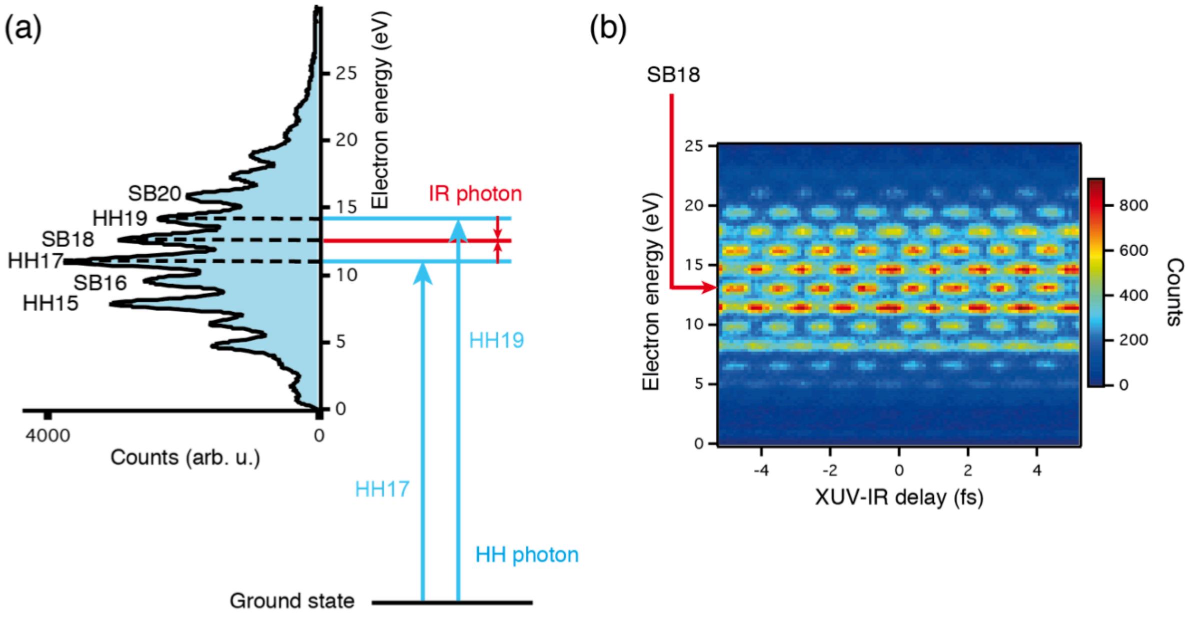

Figure 3.6. (a) Principle of the RABBITT technique illustrated by two consecutive HH. The SB18 can be populated upon the excitation path HH17 plus absorption of one IR photon or upon absorption of HH19 plus emission of one IR photon. (b) RABBITT spectrogram. Recording electron spectra for different XUV-IR delays leads to a typical spectrogram, here measured with the COLTRIMS apparatus.

In order to understand the mechanism behind the generation of the SB the problem has been treated in second-order perturbation theory [6] assuming monochromatic harmonics and IR fields. In this picture the appearance of the oscillating SB is due to the interference of two different quantum paths leading to the same final state. The paths involve the simultaneous absorption of the $(2q-1)^{\text{th}}$ HH plus one IR photon or the absorption of the $(2q+1)^{\text{th}}$ HH and the emission of one IR photon. Following this approximation the 2q$^{\text{th}}$ SB oscillation can be calculated analytically [6] and is given by

$$S_{2q} = \alpha + \beta \cos\left(2\omega\tau - \Delta\varphi_{2q} - \Delta\varphi_{\text{atomic}}\right). \tag{1.24}$$

Here, α and β are constants, ω is the angular frequency of the IR, τ is the XUV-IR delay, $\Delta\varphi_{2q}$ is the difference of the XUV phase between two neighboring harmonics and $\Delta\varphi_{\text{atomic}}$ is a intrinsic phase contribution (called atomic phase) which originates from the difference of the phases of the transition matrix elements associated to the paths HH+IR and HH-IR.

The atomic phase is considered usually to be a small contribution. For most noble gases these were calculated using lowest-order perturbation theory and by solving the time-dependent Schrödinger equation (TDSE) in the single-active-electron (SAE) approximation (for argon, neon and helium) [54]. Using this small value equation (1.24) allows to access the XUV phase differences $\Delta\varphi_{2\text{q}}$ by analyzing the phase shift of the SB signals at different energies. These phase differences can be used to evaluate an XUV phase $\varphi_{2\text{q}+1}$ at the position of the harmonic 2q+1 with an arbitrary phase offset φ_0 (e.g. $\varphi_0 = 0$ for a randomly chosen harmonic energy).

Even though $\varphi_{2\text{q}+1}$ can be retrieved for each harmonic energy, the assumption of monochromatic fields within the RABBITT approximation leads to some limitations. The pulse intensity I_{XUV} of this approximated field is given simply by the sum over monochromatic waves

$$I_{\text{XUV}}(t) = \left| \sum_{\text{q}} A_{2\text{q}+1} \exp\left[i\left(\frac{E_{2\text{q}+1}}{\hbar} t + \varphi_{2\text{q}+1} \right)\right] \right|^2, \tag{1.25}$$

where $E_{2\text{q}+1}$ is the energy, $A_{2\text{q}+1}$ is the spectral Amplitude and $\varphi_{2\text{q}+1}$ is the spectral phase of the (2q+1)$^{\text{th}}$ harmonic. The spectral amplitudes can be most easily extracted by a photon spectrometer, where the spectral phase can be extracted by the SB oscillations. Using equation (1.25) for the pulse reconstruction results in a infinitely long pulse train with identical pulses. The RABBITT technique therefore does not allow to determine the number of pulses within the pulse train. It only allows to determine the average pulse duration of the individual pulses.

Chapter 4

Single attosecond pulses

For pump-probe experiments with true[7] attosecond resolution the generation of single attosecond pulses (SAPs) is highly desirable. Unfortunately, the HH process intrinsically delivers APTs since an attosecond pulse is generated in each half cycle of the driving field. In order to overcome this limitation, a method has to be developed to force the process to emit HH only once within the driving IR pulse or alternatively to select a single attosecond pulse from the pulse train. This was already successfully demonstrated shortly after the first RABBITT measurements [7,18]. Here, the isolation of a SAP was achieved by the use of few-cycle IR pulses (5 fs) in combination with the spectral filtering of the HH cut-off. The latter is only generated by the most intense half-cycle of the IR pulse. For a proper CEP the cut-off therefore appears continuous. Filtering of this part should in principle correspond to a SAP. The generation of a continuous spectrum is a good indication of SAP generation but not a proof. The temporal structure of the cut-off spectrum was therefore analyzed with a pump-probe technique known as the attosecond streaking [55] in conjunction with a reconstruction algorithm known as Frequency-Resolved Optical Gating for Complete Reconstruction of Attosecond Bursts (FROG-CRAB) [56]. Both of these technique are the topic of this chapter.

The first section of this chapter presents today's most common schemes for the production of SAPs. The topic of the subsequent sections is the attosecond streaking technique and the FROG-CRAB which is shown to be capable not only to characterize the attosecond pulse duration, but also to extract ionization time delays between electron.

---

[7] True in this context refers to the fact that APTs e.g. do not allow to resolve the sub-cycle (attosecond) structure of the IR-probe field in a XUV-IR pump-probe experiment. However, the interference pattern in APT-IR experiments still allows to access attosecond dynamics.

4.1 Schemes for SAP generation

Even in the ideal case of mono-cycle driving pulses HHG would occur twice per pulse. Therefore, schemes have to be developed in order to confine HHG to a half-cycle or to post-select a SAP from the APT. Today there are various competing techniques. Some of the most important are illustrated in Fig. 4.1. In the following these scheme are discussed.

The polarization gating (PG) technique was initially proposed by Corkum et al. [57] and eventually experimentally demonstrated by Sola et al. [58] and Sansone et al. [59]. It is based on the dependence of the ellipticity of the generating field on the HHG process. Early experimental studies already demonstrated that the HH yield is strongly ellipticity dependent [60]. The measurements suggest that HHG does not occur for ellipticities $\varepsilon \geq 0.13$ (the exact value depends on the harmonic order). In the semi-classical picture of the three-step-model this can be easily explained: The classical trajectories of the electrons do not recombine if the field changes its orientation during a half-cycle. HHG is therefore not expected. Due to the finite spread of the ion core and the electron wavepacket the recombination with the parent ion can still occur up to a certain degree of ellipticity $\varepsilon_{\mathrm{thr}}$. This can be used in order to isolate a SAP by preparing the time-dependent polarization state such that it would only have a half-cycle window (gate) τ_{g} in which its ellipticity would be smaller than 0.13.
Experimentally, this can be done e.g. using a broadband quarter waveplate and a birefringent plate of proper thickness as shown in Fig. 4.1 (a). The optic axis (OA) of the quarter waveplate is oriented in $45°$ relatively to the incoming linear laser polarization. This generates a circular pulse that enters the birefringent delay plate. The latter has its OA parallel to the initial laser polarization. This allows to generate two delayed replica of the circular pulse having opposite helicity. If both parts overlap in time a linear intermediate part is generated. The thickness of the delay plate determines the temporal shift δ of the circular pulses.
In reference [61] it was shown that the temporal gate τ_g is given by

$$\tau_g = \frac{\varepsilon_{\mathrm{thr}} T_{\mathrm{p}}^2}{\ln(2)\delta}, \tag{1.26}$$

where T_{p} is the pulse duration. For the PG technique there is an upper limit for the pulse duration determined by two conditions [62]:

i. The gate needs to be smaller than one half-cycle: $\tau_g < T_0 / 2$.
ii. The contrast between the peak intensity within the gate and outside needs to be reasonable: $\delta < T_{\mathrm{p}}$. Otherwise, the elliptical leading edge can deplete the ground state population before the linear part starts.

Applying these conditions to equation (1.26) leads to

$$\tau_g = \frac{\varepsilon_{\mathrm{thr}} T_{\mathrm{p}}^2}{\ln(2)\delta} < \frac{\varepsilon_{\mathrm{thr}} T_{\mathrm{p}}}{\ln(2)} < T_0 / 2, \tag{1.27}$$

where T_0 is the laser cycle time. Rearranging equation (1.27) delivers an estimate for the minimum pulse duration necessary for PG

$$T_{\mathrm{p}} = \frac{\ln(2) T_0}{2\varepsilon_{\mathrm{thr}}} \approx 7\,\mathrm{fs}, \tag{1.28}$$

where the numerical value is retrieved by supposing $T_0 = 2.7\,\mathrm{fs}$ (800 nm) and $\varepsilon_{\mathrm{thr}} = 0.13$. Hence, for PG few-cycle pulses are necessary.

Nowadays, few-cycle pulses shorter than 5 fs (at 800 nm) are produced in many laboratories mostly by the HCF-technique. Nevertheless, these pulses are sensitive to many parameters making them challenging to use on a daily basis. The double optical gating (DOG) [63] relaxes the requirement on the pulse duration by supplementing the PG technique with a two-color field. Figure 4.1 (b) illustrates its principle scheme. A delay plate (OA in 45°) generates two linear polarized IR pulses orthogonally polarized to each other. These pulses then pass a second quartz plate and a BBO crystal where both OAs are aligned with the initial polarization. Since the quartz plate is positive and the BBO is negative uniaxial the thicknesses can be chosen such that they effectively form a quarter wave-plate. This configuration then generates a polarization gate as in Fig. 4.1 (a) with an additional second harmonic (SH) field produced by the BBO crystal. In the inset of Fig. 4.1 (b) the x- and y-component of the superposed electric fields are shown. As can be seen the SH field breaks the symmetry of the driving field leading to only one emission per laser cycle. This allow to use e.g. 8 fs or even longer pulses which can be routinely generated with the HCF technique. Since the DOG technique has no strong limitations (e.g. on the bandwidth or scalability) it is seen as one of the most promising schemes for shortest and highest energy SAPs.

The amplitude gating was the first scheme that successfully allowed for SAP generation [7,18]. Its idea is based on the observation of a CEP dependent cut-off. The cut-off shows a modulated spectrum for certain CEP values, where for others it appears almost perfectly smooth. This can be understood from Fig. 4.1 (c): In case of a few-cycle pulse with a cosine type CEP the strongest half-cycle has a significantly higher intensity then all others. Therefore, this particular half-cycle cut-off corresponds to the highest energies appearing in the HH spectrum. For a sine type CEP there are two consecutive half-cycle with same intensity. Each cut-off energy therefore is generated by two trajectories leading to the observation of HH peaks. Filtering of the cut-off part of the spectrum hence allows to generate SAPs. In order to do so an XUV multilayer mirror can be used acting as a bandpass filter. Today the amplitude gating is used in several laboratories.

The idea behind the ionization gating technique is to confine HHG by ionization effects. For this purpose, above-saturation intensity few-cycle driving pulses are necessary. In [64] SAPs were generated and explained by a rapid loss of phase matching for half-cycles occurring after the first powerful one(s) (see Fig. 4.1 (d)). SAPs from ionization gating were also demonstrated by Ferrari et al. [65]. Here, the underlying ionization gating mechanism is attributed rather to the single-atom response allowing only for one or two trajectories depending on the CEP.

The so-called ‘attosecond light house’ [66] is a spatio-temporal gating technique. It relies on the possibility to generate rapidly changing wavefronts in the focus of the driving pulse. If the wavefront rotates significantly during one half-cycle of the laser period, SAPs are emitted in different spatial directions (see Fig. 4.1 (e)). A wavefront rotation can be generated e.g. using a pair of glass wedges where one wedge is strongly tilted against the other or by a slightly misaligned grating compressor.

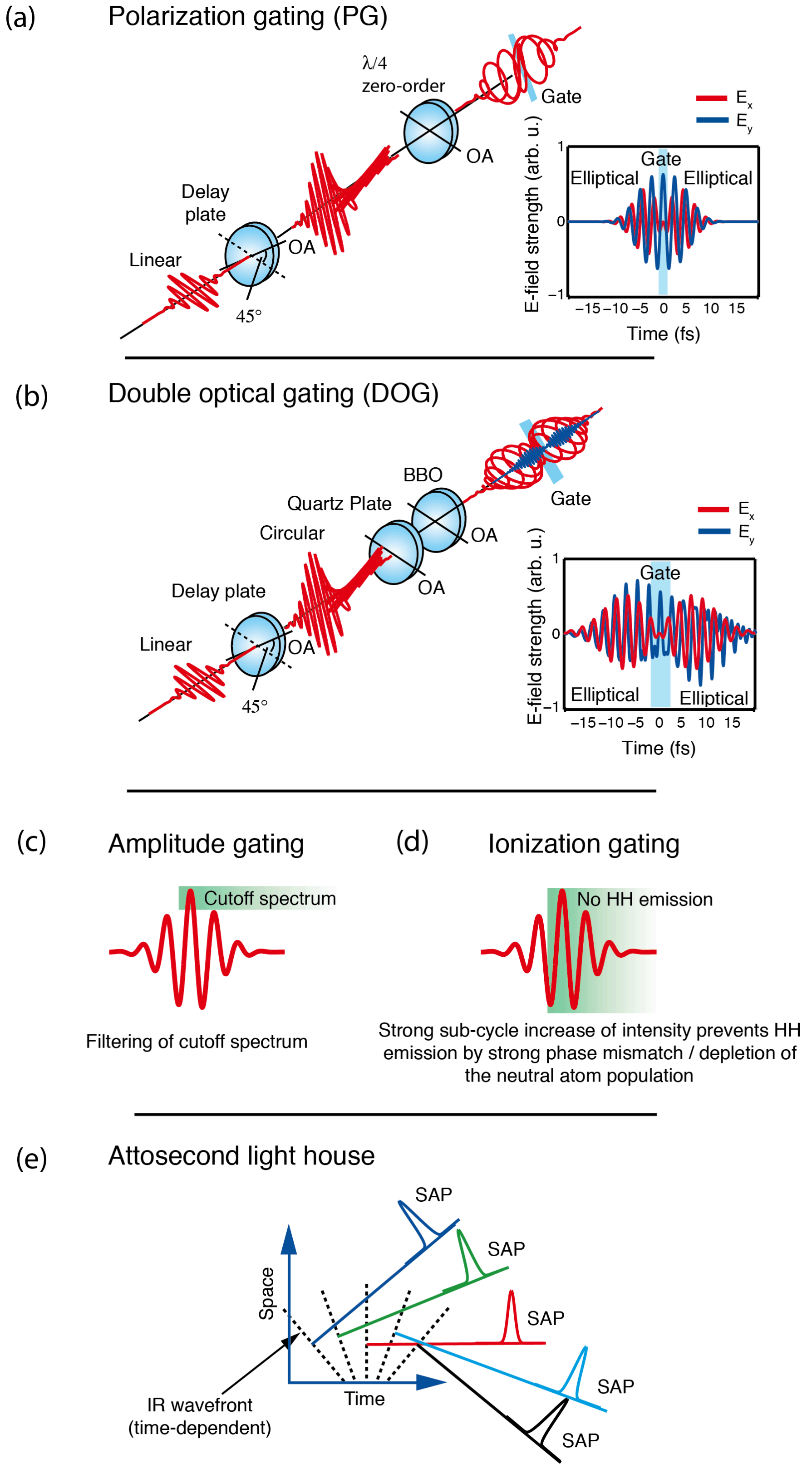
(a)
Polarization gating (PG)
λ/4
zero-order
Gate
OA
Delay
plate
OA
Linear
45°
E-field strength (arb. u.)
Gate
Elliptical
Elliptical
1
0
−1
−15 −10 −5 0 5 10 15
Time (fs)
E_x
E_y
(b)
Double optical gating (DOG)
BBO
Quartz Plate
Circular
OA
OA
Gate
Delay plate
Linear
OA
45°
E-field strength (arb. u.)
Gate
Elliptical
Elliptical
1
0
−1
−15 −10 −5 0 5 10 15
Time (fs)
E_x
E_y
(c)
Amplitude gating
Cutoff spectrum
Filtering of cutoff spectrum
(d)
Ionization gating
No HH emission
Strong sub-cycle increase of intensity prevents HH emission by strong phase mismatch / depletion of the neutral atom population
(e)
Attosecond light house
SAP
SAP
SAP
SAP
SAP
Space
Time
IR wavefront
(time-dependent)

Figure 4.1. Illustration of important gating schemes for SAP generation. Detailed information can be found in the text.

4.2 The attosecond streaking technique

The attosecond streaking technique is conceptually very similar to (or even an extension of) the traditional streak cameras [45,67] developed to measure the temporal profile of light pulses: The pulse, to be measured, in directed onto a biased metal plate thereby liberating electrons. The electron bunch is assumed to be a perfect replica of the optical pulse shape. These electrons are then exposed to a fast (e.g. microwave) field perpendicular to their propagation direction created by a voltage ramp on a plate capacitor. If the field ramp is fast enough the temporal axis of the electron distribution is mapped to position space. This can be detected e.g. by a phosphor screen.

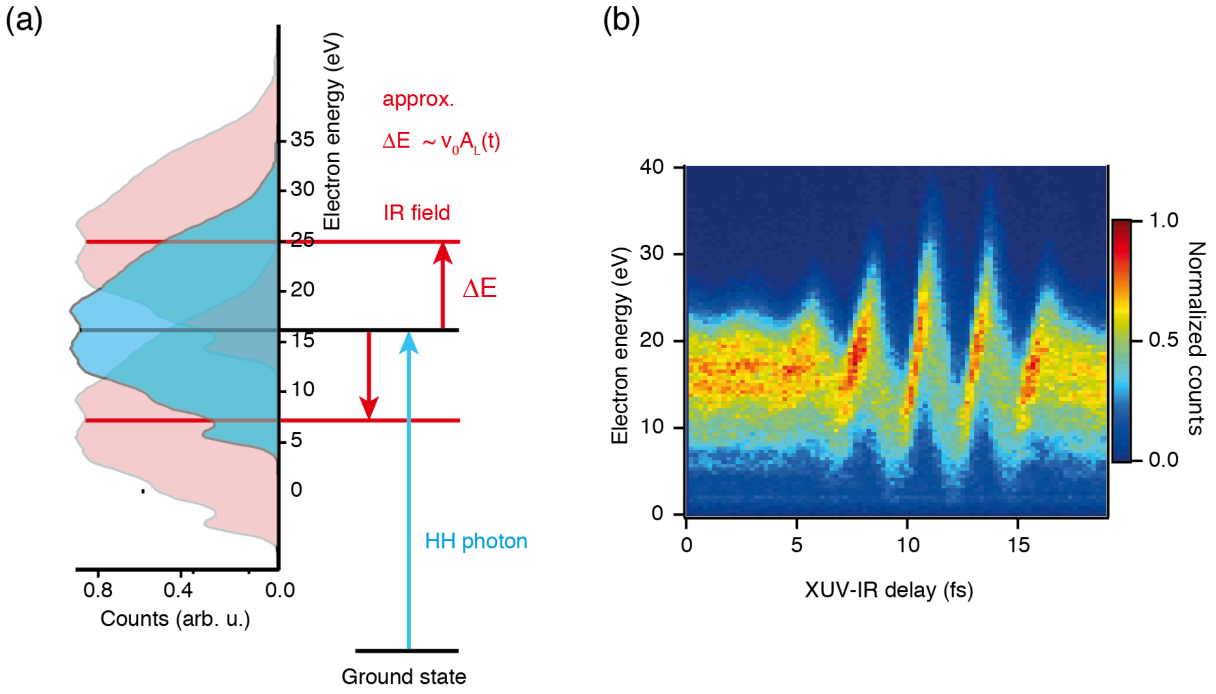

Figure 4.2. Principle of the attosecond streak camera. (a) The SAP produces a continuous electron distribution (blue) upon ionization of a ground state atom (here Ar). If an additional IR field is used the whole spectrums shifts according to the product $v_0 A_L$. (b) Recording the electron spectrum as a function of XUV-IR delay reveals a spectrogram with a modulation that follows approximately the vector potential of the IR field.

The principle of the 'attosecond streak camera' [7] is presented in Fig. 4.2 (a). Starting from the ground state e.g. of a noble gas atom an electron replica is generated upon excitation with an SAP leading to a continuous electron spectrum (blue shaded area). This electron distribution is observed to shift as an additionally moderately strong IR pulse (typically $10^{12}\,\mathrm{W/cm^2}$) is spatially and temporally overlapped. Recording the electron distribution as a function of XUV-IR delay leads to a characteristic spectrogram as shown in Fig. 4.2 (b), here measured with our COLTRIMS detector.

The mechanism can be understood in a classical picture: Each liberated electron experiences a force that is given by the electric field of the IR

$$\boldsymbol{F}_{\mathrm{el}} = -e\boldsymbol{E}_{\mathrm{IR}} = m\boldsymbol{a}\,. \tag{1.29}$$

This leads to the differential equation $\dot{\boldsymbol{v}} = e/m\,\boldsymbol{E}_{\mathrm{IR}}$. Hence, for the velocity change of electrons born at time t_0 it follows

$$\Delta\boldsymbol{v}(t_0) = -\frac{e}{m}\int_{t=t_0}^{\infty} \boldsymbol{E}_{\mathrm{IR}}\,dt = -\frac{e}{m}\boldsymbol{A}_{\mathrm{L}}(t_0)\,, \tag{1.30}$$

where $\mathbf{A}_{\mathrm{L}}$ is the vector potential of the IR field.

Or if expressed in terms of kinetic energy of the electron with initial velocity $\mathbf{v_0}$

$$E_{\mathrm{kin}}(t_0) = \frac{1}{2}m_{\mathrm{e}}\left(\boldsymbol{v_0} - \frac{e}{m}\boldsymbol{A}_{\mathrm{L}}(t_0)\right)^2. \tag{1.31}$$

Reducing equation (1.31) to 1D, we can approximate for $v_0 >> \Delta v$

$$E_{\mathrm{kin}}\left(t_0\right) = E_0 - v_0 e A_{\mathrm{L}}\left(t_0\right), \tag{1.32}$$

where $E_0 = 1/2 m_{\mathrm{e}} v_0^2$. In an XUV–IR pump-probe experiment t_0 corresponds to the time delay τ of the two pulses. Hence, the modulation of the electron spectrum in Fig. 4.2 (b) is in this approximation a direct measure of the vector potential of the IR laser field.

The attosecond streaking technique can obviously be used to characterize the electric field of an ultrashort pulse. But it also allows to reconstruct the temporal characteristics of the SAP. For this purpose, a method dubbed FROG-CRAB was developed by Y. Mairesse and F. Quéré [56]. It allows to decompose the vector potential and the complex electron spectrum thereby allowing to reconstruct the attosecond pulse structure. A detailed description can be found in the next section.

4.3 The FROG-CRAB technique

The FROG-CRAB technique [56] aims at reconstructing the attosecond pulse from an attosecond streaking experiment. To this end, a proper formalism has to be developed to describes the appearance of such a spectrogram. Using the strong field approximation (SFA) [68] the measured spectrogram intensity $I(\boldsymbol{p},\tau)$ for a electron with momentum $\boldsymbol{p}$ and at a XUV-IR delay τ can be described in atomic units by

$$\begin{gathered} I(\boldsymbol{p},\tau)=\left|\int_{-\infty}^{\infty}\boldsymbol{d}_p\boldsymbol{E}_{\mathrm{XUV}}(t-\tau)\exp\left(i\phi_{\mathrm{L}}(t)\right)\exp\left[i\left(\boldsymbol{p}^2/2+I_{\mathrm{p}}\right)t\right]dt\right|^2, \\ \phi_{\mathrm{L}}(t)=-\int_t^{\infty}\left[\boldsymbol{p}\boldsymbol{A}_{\mathrm{L}}+\boldsymbol{A}_L{}^2/2\right]dt. \end{gathered} \tag{1.33}$$

Here, $\boldsymbol{d}_p$ is the transition dipole matrix element connecting the ground state with the continuum state, $\boldsymbol{E}_{\mathrm{XUV}}(t)$ is the electric field of the XUV pulse, $\boldsymbol{p}$ is the momentum of the electron and $\boldsymbol{A}_{\mathrm{L}}(t)$ is the vector potential of the IR. The following assumption are made in order to simplify the problem:

1) The equation is reduced to 1D. This approximation is valid for attosecond streaking experiments since the electrons are collected within a small solid angle.
2) The product $d_pE(t)$ represents the electron pulse that is created upon excitation with the attosecond pulse, where d_p is a complex quantity. In general this can lead to a different spectral distribution (cross-section) and it can also introduce a phase. However, for the FROG-CRAB pulse reconstruction d_p is set equal to 1.
3) The momenta of the electrons are approximated with the central momentum of the distribution $p \approx p_{\mathrm{C}}$ (as if all electrons would be streaked as the electrons with initial momentum p_{C}).

With these assumptions equation (1.33) can be rewritten as

$$I(p,\tau)=\left|\int_{-\infty}^{\infty}E_{\mathrm{XUV}}(t-\tau)\exp(i\phi_{\mathrm{L}}(t))\exp\left[i\left(p^2/2+I_{\mathrm{p}}\right)t\right]dt\right|^2,$$
$$\phi_{\mathrm{L}}(t)=-\int_{t}^{\infty}\left[p_{\mathrm{C}}A_{\mathrm{L}}+A_{\mathrm{L}}{}^2/2\right]dt \tag{1.34}$$

Figure 4.3 shows a typical simulated trace produced by evaluating equation (1.34).

In practice, the trace $I(p,\tau)$ belongs to an unambiguous pair of E_{XUV} and A_{L}. Using an iterative procedure such as the generalized projection algorithm [38] therefore allows to extract both quantities.

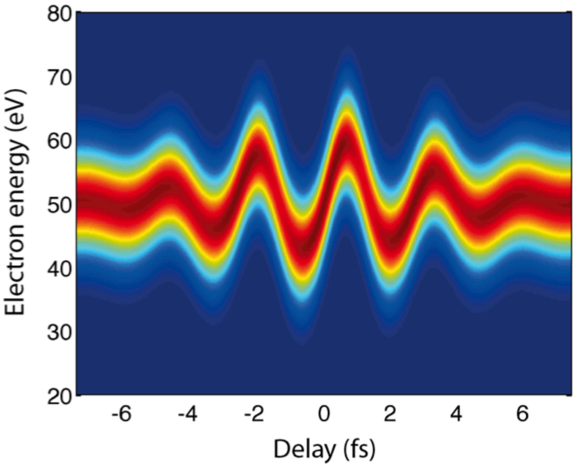

Figure 4.3. Simulated FROG-CRAB trace. Following parameter were used: A $5\,\mathrm{fs}$ IR pulse with $10^{13}\,\mathrm{W/cm^2}$ intensity and a chirped attosecond pulse with a transform-limit of $150\,\mathrm{as}$ and a GDD of $2000\,\mathrm{as}^2$.

Within this thesis the FROG-CRAB technique was applied to the streaking traces measured with the COLTRIMS detector in order to characterize the single attosecond pulses. The results are presented in section 6.5.

Additionally, in chapter 8 the FROG-CRAB technique has been used to extract ionization time delays between the valence electrons of different atomic species by accessing the group delay. Indeed, time delays are encoded in the reconstructed phase of the electron wavepacket generated upon photoionization. In order to demonstrate the capability of the FROG-CRAB algorithm to reconstruct time-delays, a seed matrix has been prepared containing two energetically separated attosecond streaking traces. These traces have different spectral bandwidth with the same amount of chirp and are shifted by a certain delay $\Delta\tau$. Such traces can result in experiments if e.g. two different initial states are excited by the same attosecond pulse and streaked by the same field. The FROG-CRAB algorithm allows to extract the spectral phase of the two traces which are in the following referred to as φ^{up} and φ^{low} for the upper and lower trace, respectively. This allows to determine the time delay through the derivative of the phases

$$\Delta\tau_g = \frac{\partial\varphi^{up}}{\partial\omega} - \frac{\partial\varphi^{low}}{\partial\omega} = \hbar\left(\frac{\partial\varphi^{up}}{\partial E} - \frac{\partial\varphi^{low}}{\partial E}\right). \tag{1.35}$$

Two examples have been prepared. In Fig. 4.4 a large delay of 200 as has been chosen between the two traces, where the example of Fig. 4.5 shows the same for a small delay of 10 as. It can be seen that the FROG-CRAB algorithm reliably reconstructs the time delays even if the values are relatively small.

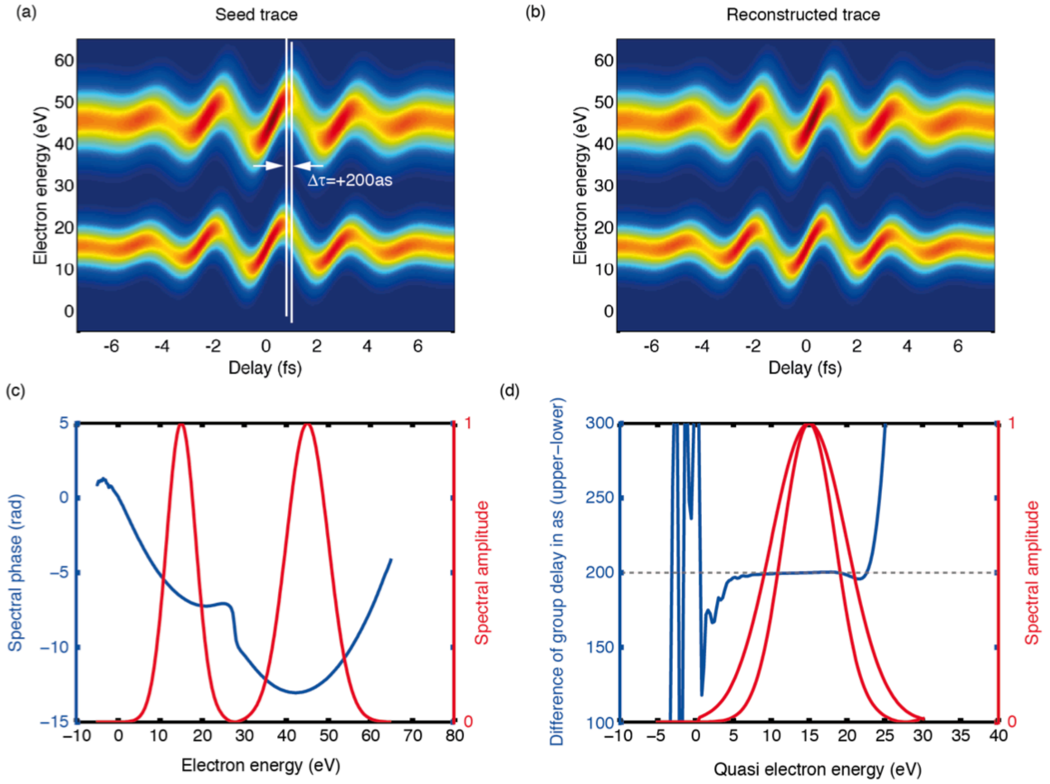

Figure 4.4. Testing the time delay extraction from FROG-CRAB. In (a) a matrix has been prepared containing two attosecond streaking traces delayed by 200 as. The reconstructed phases of both parts φ^{up} and φ^{low} (c) allows to determine the time delay between both traces (d).

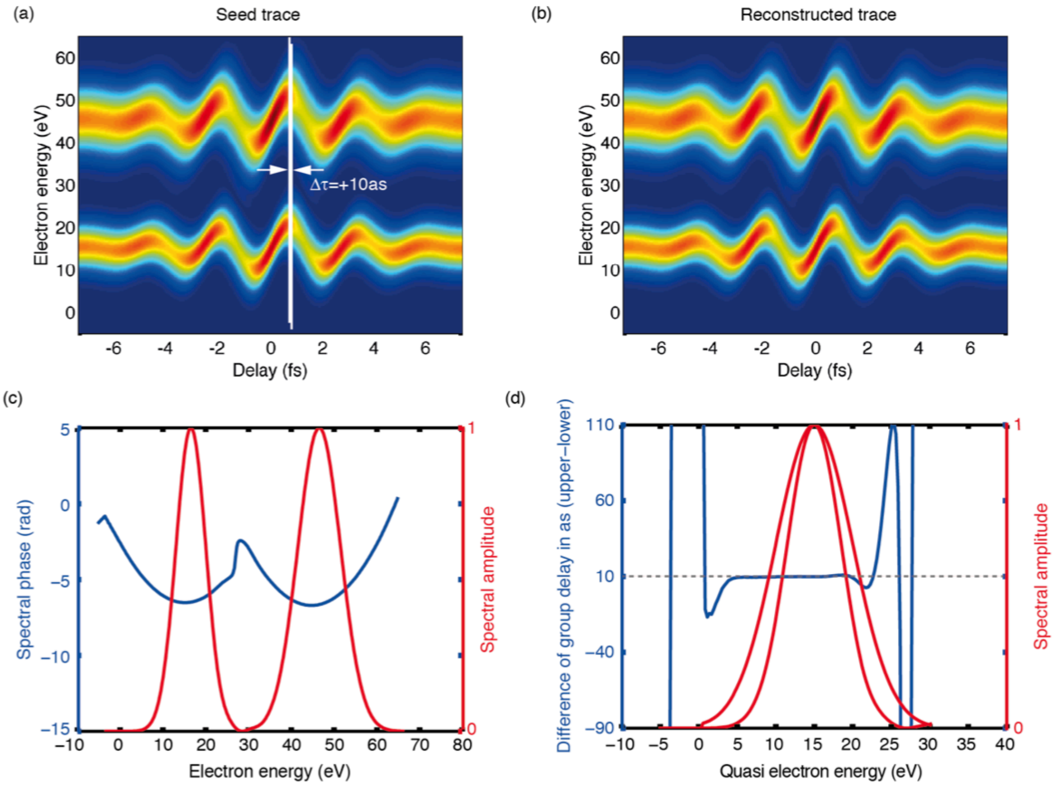

Figure 4.5. Testing the time delay extraction from FROG-CRAB. Same plots as in Fig. 4.4 except that a time delay of only 10 as has been chosen.

As mentioned above, in the framework of this thesis this method has been applied to streaking traces measured simultaneously in a two species target (Ar and Ne). In this case the traces mostly overlap energetically. The use of coincidence detection has nevertheless allowed us to distinguish between the two types of electrons. As described in chapter 8 both traces have been patched on top of each other allowing to follow the same procedure as described in this section.

Chapter 5

The COLTRIMS detector

The COLd Target Recoil Ion Momentum Spectroscopy (COLTRIMS) [8,9] detector (also called reaction microscope) was developed in the 1980s for spectroscopic studies on fragmentation processes in gas phase. It offers unique possibilities such as the access to the 3D momentum vector of each individual charged fragment after a break-up reaction and the possibility to measure the fragments in coincidence allowing to assign an electron to its parent ion. In the ultrafast community the COLTRIMS technique is already well established and e.g. used for strong-field experiments involving IR pulses. In the last couple of years a lot of effort was put into the development of a combination of an attosecond front-end with a COLTRIMS detector, because such a symbiosis opens the way to full kinematic time-resolved studies with attosecond resolution.

5.1 The COLTRIMS apparatus

This section gives a brief overview of the COLTRIMS apparatus. Details can be found in various review articles such as in [8,9]. For more specific information about the setup used within this thesis the reader is referred to reference [69].

A schematic of the apparatus is shown in Fig. 5.1. In the framework of this thesis an XUV pulse (illustrated in blue) ionizes atoms or molecules within the gas jet. The jet chamber geometry allows to provide a cold and narrow stream of atoms/molecules with small transverse velocity spread enabling high resolution spectroscopy. The charged fragments experience an electric field generated by biased copper plates. Depending on the sign of their charge, the fragments are, therefore, guided either to the left or to the right detector. An additional magnetic field generated from a pair of Helmholtz coils (not shown) forces the electrons onto helical trajectories allowing to collect all electrons independent of their emission direction. The trajectories of the ions are generally less influenced by the magnetic field due to their much larger mass. Each of the detectors consists of a micro-channel plate (MCP) and a delay line anode (HEX anode or QUAD anode), and are therefore time- and position sensitive.

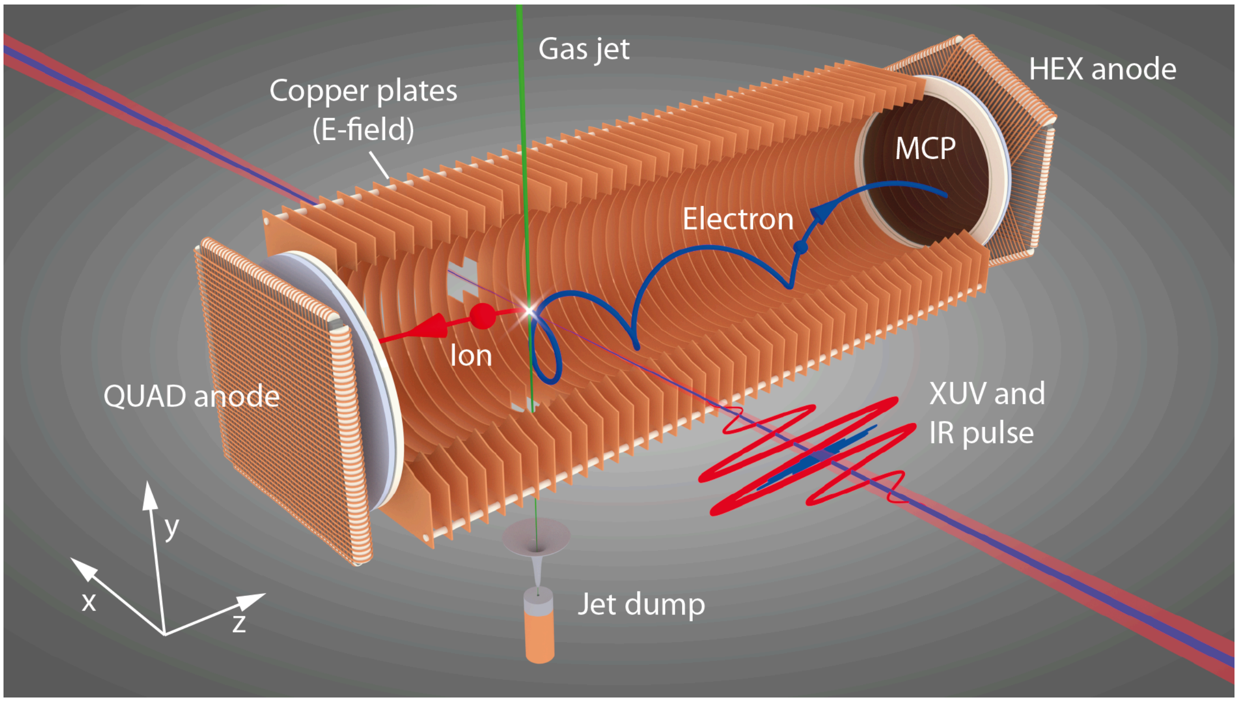

Figure 5.1. Schematic of a COLTRIMS detector. An XUV pulse (blue) ionizes atoms or molecules in the supersonic gas jet inside the COLTRIMS detector. A delayed IR pulse is used as a probe. The fragments arrive either on the left or the right detector depending on the sign of the charge. Detailed information can be found in the text.

This combination permits reconstructing the 3D momentum vector of each of the fragments. Since the COLTRIMS detector is able to measure the ionization fragments simultaneously, momentum conservation allows to perform coincidence spectroscopy. This means that e.g. in any single ionization event an electron can always be assigned to its parent ion.

5.2 Reconstruction of the 3D momenta of fragments

Upon ionization with attosecond pulses charged fragments are created. These fragments are first exposed to the fields of the ionizing attosecond and the probing IR pulse. Both of these interactions occur within a few femtoseconds. The particle movement is therefore restricted to the nanometer range which is negligible compared to the focal dimensions of the beams. It is therefore valid to assume that all fragments are generated in one single spot that we will define as the origin of the coordinate system. The particles then only experience the external electric and magnetic fields generated with the COLTRIMS apparatus. In the following discussion a coordinate system is used as shown in Fig. 5.1 with its origin defined at the intersection of the jet with the laser focus.

Using Newton's equation of motion we can determine the trajectory $\left(x(t),y(t),z(t)\right)$ of the particle with the initial momentum $\mathbf{p}=(p_x,p_y,p_z)$:

$$x(t)=\frac{1}{Bq}\left[p_x\sin\left(\frac{Bqt}{m}\right)+p_y\left(1-\cos\left(\frac{Bqt}{m}\right)\right)\right]$$

$$y(t)=\frac{1}{Bq}\left[p_y\sin\left(\frac{Bqt}{m}\right)-p_x\left(1-\cos\left(\frac{Bqt}{m}\right)\right)\right] \tag{2.1}$$

$$z(t)=\frac{1}{2}\frac{Eq}{m}t^2+\frac{p_z}{m}t.$$

Here, E and B are the field strength applied in the experiment, q is the charge of the fragment under investigation and m is its mass.

After the TOF $t=t_{\mathrm{TOF}}$ the particle reaches the detector and hence $\left(x(t_{\mathrm{TOF}}),y(t_{\mathrm{TOF}})\right)=(X,Y)$ defines the position of impact on the delay line anode and $z(t_{\mathrm{TOF}})=Z$ is given by the distance between the intersection of the laser with the jet and the detector plate. Equations (2.1) can be rearranged such that the initial momentum can be calculated from the measured quantities:

$$p_x = -\frac{1}{2}Bq\left(Y - \frac{X}{\tan\left(\frac{Bqt_{\mathrm{TOF}}}{2m}\right)}\right)$$

$$p_y = \frac{1}{2}Bq\left(X + \frac{Y}{\tan\left(\frac{Bqt_{\mathrm{TOF}}}{2m}\right)}\right) \tag{2.2}$$

$$p_z = \frac{mZ}{t_{\mathrm{TOF}}} - \frac{1}{2}Eqt_{\mathrm{TOF}}.$$

Together with a proper method for the calibration of the quantities $t_{\mathrm{TOF}}, B, E, X, Y, Z$ this set of equations allows for the reconstruction of the initial 3D momenta.

5.3 Calibration of the detector

For the extraction of the momentum vectors $\boldsymbol{p}$ of the charged fragments the exact knowledge of the quantities $t_{\mathrm{TOF}}, B, E, X, Y,$ and Z is required. This calibration is usually done after the experiments.

The TOF-spectrum of the ions and electrons are recorded during the whole experiment. However, the time zero is generally unknown. In XUV experiments usually a large amount of XUV hits on the MCP are registered. Since these events arrive much faster then the charged particles they can be used as a first calibration of the time zero. In Fig. 5.2 the ion TOF measured in a Ar/Ne gas mixture is exemplarily shown. The photon peak at the left can be used as a reference to determine the TOF of all other species.

The magnetic field experienced by the fragments can be determined by the cyclotron trajectory of the electrons (ions are much less influenced). It can be seen from equation (2.1) that the electrons cross the zero of the *x*-*y*-plane whenever $Bqt_c / m = 2\pi \cdot N$ holds, independent of their transvers momenta p_x and p_y, where t_c is the cyclotron time and *N* is an integer number. This zero interceptions can be observed e.g. in a *x* vs TOF plot allowing to access t_c. In order to get a good estimate for B one can plot the different zero crossing time differences t_c against their estimated index N (see Fig. 5.3). If the latter turns out to be correct the indicated discrepancy δt should be smaller then t_c which gives at the same time a correction to the estimated time zero calibration extracted from the photon peak.

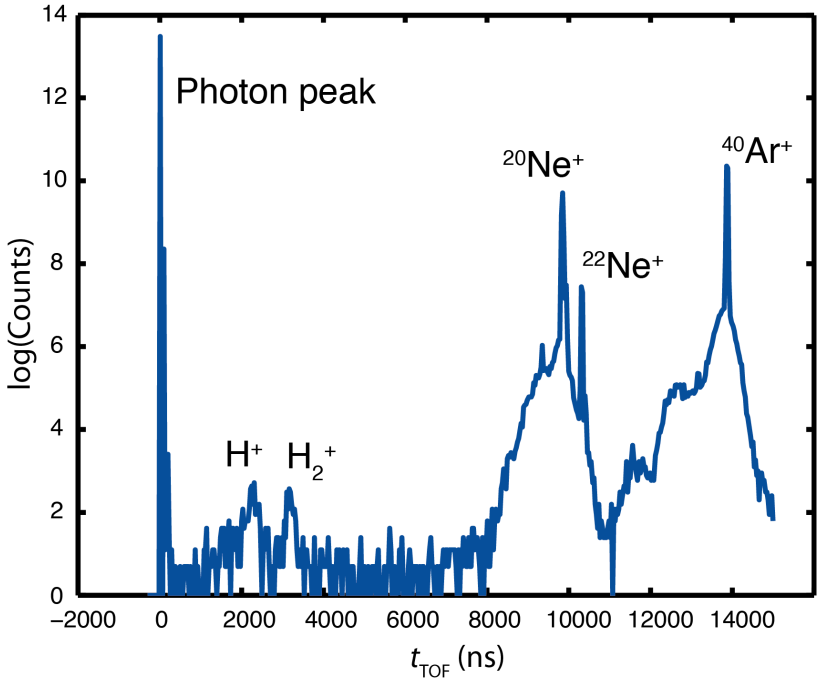

Figure 5.2. Typical TOF distribution in a Ar/Ne gas mixture. The peak appearing for very small TOF values corresponds to strayed XUV photons hitting the MCP detector. These counts can be used for a first estimation of the time-zero calibration.

The homogenous electric field E applied by the biased copper plates can be determined from the center of the TOF distribution t_{center} of a specific species. These ions have zero initial momentum which implies, together with the last part of equation (2.1): $E = 2mZ/qt_{\text{center}}^2$.

The position of impact (X,Y) on the delay line detector can be calibrated with respect to the defined coordinate system by determining the center of the particle distribution on the detector.

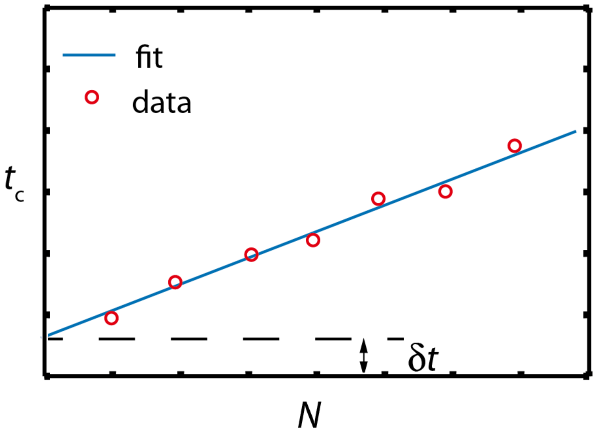

Figure 5.3. Schematic illustration of the cyclotron time t_c vs. index N. This plot can be used to determine the B-field strength from the acquired data. A residual offset δt can be caused either from a wrong estimation of N or from inaccuracies of the time zero calibration depending on the size of δt.

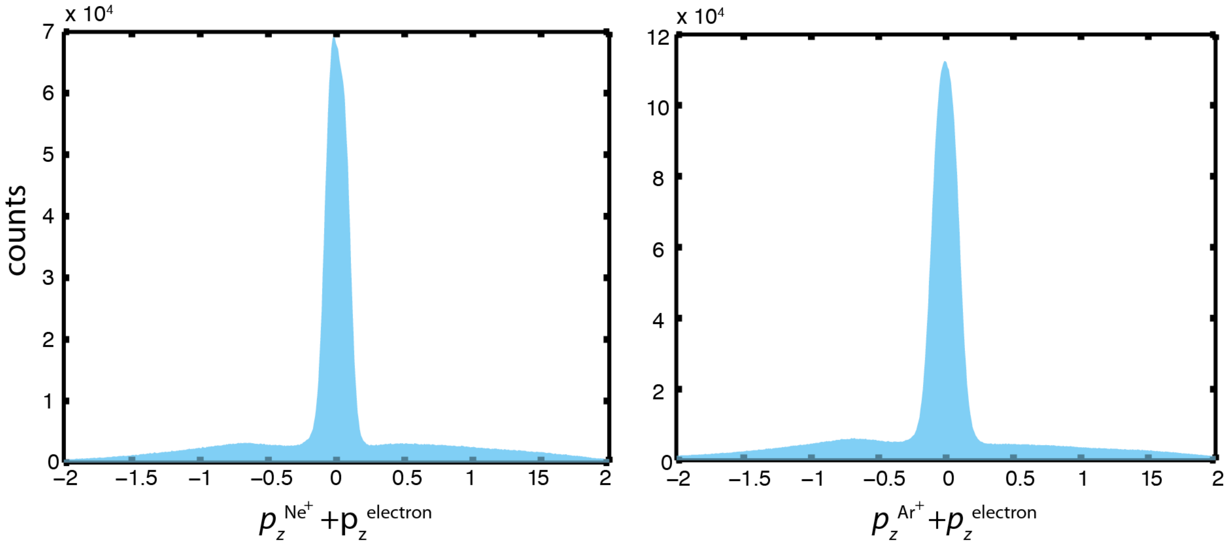

Figure 5.4. Sum of the momentum distributions along the z-direction for Ar and Ne. Due to momentum conservation after single photon ionization, this distribution has to peak at 0 momentum.

Finally, the distances between the interaction region and either detector Z_e (electron side) and Z_{Ion} (ion side) can be determined through the sum of the momentum distributions of ions and electrons e.g. along the z-direction. As shown in Fig. 5.4 due to momentum conservation upon single photon ionization the momentum sum of the measured ions and electrons exhibit a strong peak. The position of this peak has to be centered at 0, which can be used to fine tune not only Z_e and Z_{Ion} but also the electric field strength.

5.4 Coincidence detection

The sum of the ion and electron momenta (see Fig. 5.4) measured in each fragmentation process allows not only for a proper calibration but also to perform coincidence detection. In the course of this thesis a gas mixture of Ar and Ne has been prepared and used to perform simultaneous time-resolved measurements on both species. For this purpose, a narrow filter around the zero momentum has been applied to the sum distributions shown in Fig. 5.4 which allows distinguishing both types of electrons. The resulting momentum distribution is presented in Fig. 5.5, where $p_{\mathrm{perp}} = \sqrt{p_x^2 + p_y^2}$. Once the coincidence filter is applied isolated electron distributions can be extracted.

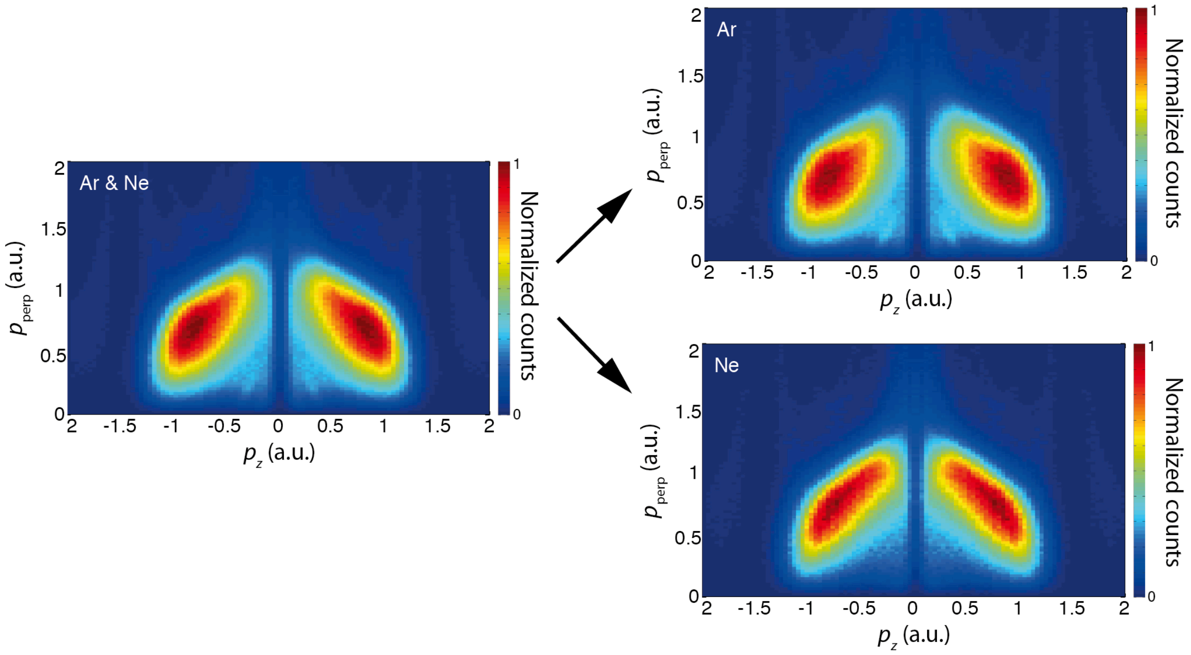

Figure 5.5. Applying a coincidence filter on the 3D electron momentum distribution measured in a gas target containing Ar and Ne. The plot on the left panel shows the momentum distribution as measured for both species. On the right panel the distributions are shown as obtained by applying a coincidence filter on the momentum sum.

Chapter 6

Combining attosecond pulses with coincidence spectroscopy

In attosecond science the detector that is used to carry out the pump-probe measurement substantially determines the type of experiment that can be addressed. There are two types of detectors that are commonly used: Spectrometers based on the measurement of photons and such that measure the momentum distribution of charged particles. Using XUV photon spectrometers pump-probe experiments can be conducted by attosecond transient absorption (ATA) spectroscopy [20-22]. In this method the absorption of the XUV spectrum in a dense target is recorded as function of the XUV-IR delay. Charged particle spectrometers instead are based on the fact that XUV pulses or intense light fields can ionize atoms or molecules in single photon or multi-photon ionization, respectively. The detection of the charged fragments allows then to record the momentum distribution as a function of the pump-probe delay. The most common charged fragment detector is the time-of-flight (TOF) spectrometer [23]. Here, the particles are physically collected within a small solid angle which effectively corresponds to the extraction of a 1D momentum distribution. More advanced spectrometers like the velocity-map imaging spectrometer (VMIS) [24] are able to resolve a 2D projection of the momentum distribution.

Access to the full 3D momentum distribution can be achieved with a COLd Target Recoil Ion Momentum Spectroscopy (COLTRIMS) detector. Here, the 3D momentum vector of each fragment is measured at the same time and in each fragmentation event. Moreover, it offers unique possibilities such as to assign an electron to its parent ion through momentum conservation which is usually referred to as coincidence spectroscopy. This potentially allows to address a broad range of open questions in attosecond science.

In the course of this thesis an attosecond beamline has been built for XUV-IR pump-probe experiments with a COLTRIMS detector. This combination is referred to as AttoCOLTRIMS. This chapter provides an overview and details of the AttoCOLTRIMS setup including the optical arrangement, vacuum system and active interferometer stabilization. In the last section we present the first attosecond streaking experiment conducted in a COLTRIMS detector which allowed to characterize the temporal structure of the pulse.

6.1 Overview

A schematic drawing of the AttoCOLTRIMS apparatus is shown in Fig. 6.1. The laser system used in our setup is a commercial CEP stabilized Ti:sapph amplifier (FEMTOPOWER compact V PRO CEP, Femtolasers). It provides pulse energies of 750 µJ with a pulse duration of 30 fs at a repetition rate of 10 kHz. These pulses are spectrally broadened in a Ne-filled hollow-core fiber [40] and subsequently compressed by chirped mirrors [70]. This results in few-cycle pulses of 5-6 fs with 400 µJ pulse energy and a spectral bandwidth that ranges from 550-950 nm at a central wavelength of about 770 nm.

The IR beam (red line in Fig. 6.1) passes a broadband beam-splitter, which has a reflectivity of 20%. The 80% portion, which is transmitted through the beam-splitter (pump), is used for HHG. For this purpose, we focus the IR beam into an Ar filled gas target of 1 mm thickness using a spherical mirror with a radius of curvature of -1000 mm. The target itself is mounted in the vacuum chamber (labeled HHG in Fig. 6.1). To precisely control its position the target is mounted on a manual xyz-translation-stage. The collinearly propagating HH radiation and the generating IR beam are then exposed to a filter unit which is described in detailed in section 6.4. The unit contains a drilled 1 mm thick fused silica plate which has an outer diameter of 10 mm. The hole has a diameter of 3 mm and is covered by an aluminum (Al) foil of 300 nm thickness. The fused silica plate itself is mounted inside a vacuum valve allowing to seal the connection between the HHG chamber and the subsequent

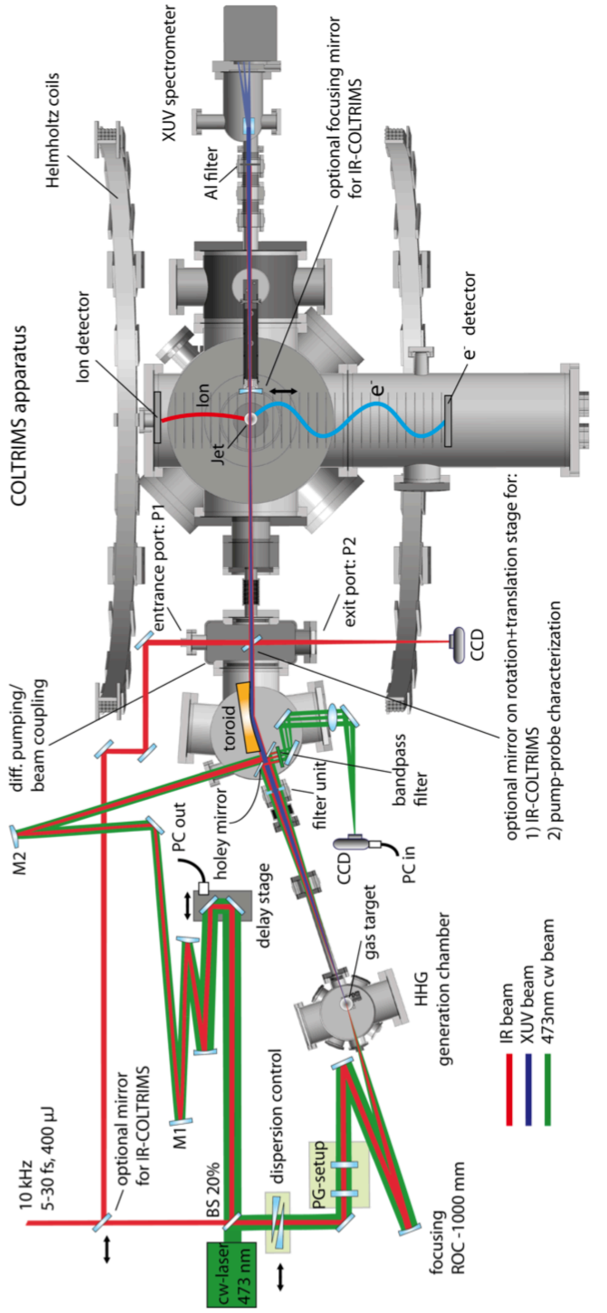
COLTRIMS apparatus
Helmholtz coils
XUV spectrometer
Al filter
optional focusing mirror for IR-COLTRIMS
Ion detector
Ion
Jet
e⁻
e⁻ detector
entrance port: P1
exit port: P2
CCD
diff. pumping/ beam coupling
toroid
optional mirror on rotation+translation stage for:
1) IR-COLTRIMS
2) pump-probe characterization
bandpass filter
filter unit
holey mirror
PC out
M2
CCD
PC in
delay stage
gas target
HHG generation chamber
IR beam
XUV beam
473nm cw beam
10 kHz
5-30 fs, 400 µJ
optional mirror for IR-COLTRIMS
M1
BS 20%
dispersion control
PG-setup
cw-laser 473 nm
focusing ROC -1000 mm

Figure 6.1. Schematic representation of the combined attosecond beamline (left side) and COLTRIMS apparatus (right side). The IR driving pulses are divided into two using a 20% beam-splitter. The more intense part is focused in the gas target in order to generate HH. The weaker part is sent through a delay line and then recombined with the XUV light by a holey mirror. Both beams are sent on a toroidal mirror which has its focus in the interaction region of the COLTRIMS. The beam of the active interferometer stabilization system is depicted by the green line. A more detailed description can be found in the text.

recombination/focusing chamber (filter unit in Figs. 6.1 and 6.2). In this way the purpose of the filter unit is twofold. On the one hand it serves as a high-pass filter for the HH radiation, blocking the IR. On the other hand it ensures that the vacuum pressure in the subsequent chambers is independent of the high pressure load in the HHG-chamber caused by the gas jet.

After passing the Al foil the HH beam recombines with the previously split-off part of the IR (20%, probe) on a holey mirror with a central hole of 2.5 mm. Therefore, the beam path from the initial beam-splitter to this point forms a Mach-Zehnder type interferometer. To adjust the delay between the pump and probe arm we use a stack of two different translation stages. The first one is equipped with a DC motor with a long travel range allowing for a coarse adjustment of the temporal overlap. The second one is a piezo positioner (PZ 38 CAP, piezosystem Jena) used for the experiments. The piezo motion is controlled through a voltage between 0-10 V where a voltage increment of 1 mV corresponds to 22.4 as in delay, leading to a full travel range of 224 fs. Finally, a toroidal mirror focuses both beams into the supersonic jet of the COLTRIMS detector creating charged fragments of the gas under investigation. Additionally, we have installed an XUV photon spectrometer at the rear side of the COLTRIMS chamber. This allows for a fast and simultaneous acquisition of the high harmonic spectrum. An additional Al foil of 500 nm thickness mounted on a mesh covers the entrance of the spectrometer in order to filter the residual IR radiation.

6.2 Vacuum chambers and vacuum system

Coincidence detection requires the count rate to be lower than the repetition rate of the laser in order to prevent multiple ionization events per laser shot. The total amount of counts measured in an experiment is composed of events origination from the supersonic jet and from the residual gas. For a good signal-to-noise ratio the background counts from the residual gas in the COLTRIMS chamber have to be reduced to a minimum, such that they are much smaller then the ones measured from the jet. Therefore, it has to be ensured that a very high vacuum is provided, preferentially on the order of 10^{-10} mbar.

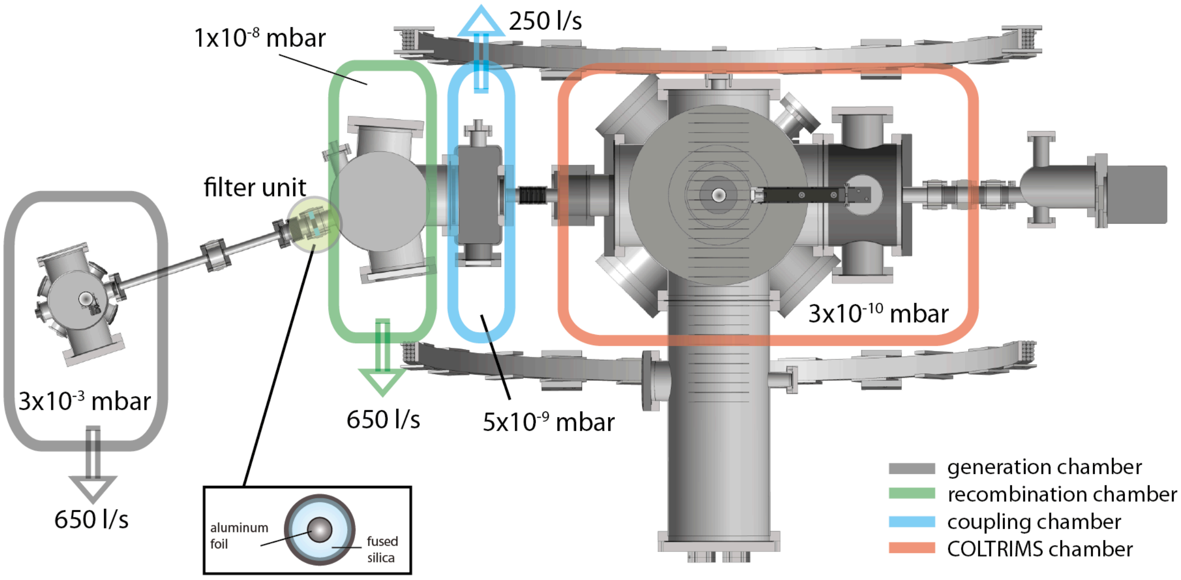
250 l/s
1x10-8 mbar
filter unit
3x10-10 mbar
3x10-3 mbar
650 l/s
5x10-9 mbar
650 l/s
aluminum foil
fused silica
generation chamber
recombination chamber
coupling chamber
COLTRIMS chamber

Figure 6.2. Schematic of the vacuum system of the AttoCOLTRIMS. A high vacuum in the COLTRIMS chamber needs to be guaranteed for the conduction of experiments with a good signal-to-noise ratio. A detailed description can be found in the text.

The COLTRIMS at ETH was previously used for strong-field experiments and is proven to provide pressures in the lower 10^{-10} mbar. However, the extension with an attosecond front-end comes along with some vacuum design challenges. This is mostly due to the high pressure load produced in the generation chamber for gas phase HHG. Figure 6.2 presents a schematic of the vacuum-system of the AttoCOLTRIMS. A turbomolecular pump (TMP) with 650 l/s pumping speed is used to maintain the pressure in the ‘generation chamber’ at around $3 \cdot 10^{-3}$ mbar. In order to prevent the gas load to enter into the subsequent ‘recombination chamber’ a valve is used containing a filter unit as shown in the inset of Fig. 6.2. This and the use of another TMP with a pumping speed of 650 l/s allows to keep the pressure at about $1 \cdot 10^{-8}$ mbar while HH are generated. The recombination chamber is followed by the ‘coupling chamber’. From the vacuum-system point of view this chamber serves as a differential pumping stage. To this end, it is equipped with two blades, one at the entrance and one at the exit, with a hole of diameter of 1.5 inch. Together with a TMP with a pumping speed of 250 l/s this finally makes sure that the COLTRIMS can be operated with a vacuum that lies at about $3 \cdot 10^{-10}$ mbar.

6.3 IR-only experiments

The COLTRIMS setup was previously used for IR-only experiments e.g. in an 'Attoclock' configuration using close-to-circular polarized IR pulses in combination with tight back-focusing, thus achieving intensities up to several units of 10^{14} W/cm^2. At such intensities the ionization process in atoms is dominated by the tunneling process. Extensive studies on this topic have been carried out in our group using this detector [5,71-73]. To maintain the option of performing IR-only experiments, we incorporate the necessary details: The IR beam may alternatively be sent into vacuum via the entrance port P1 of the coupling chamber, where a movable mirror can be introduced in the beam path to reflect the light into the COLTRIMS chamber. The back-focusing mirror necessary for the IR-only experiments has been mounted on a manipulator placed in the COLTRIMS chamber, which allows for precise alignment of its position as well as complete removal while XUV-IR experiments are performed.

6.4 Active interferometer stabilization

Attosecond interferometric stability of the pump-probe setup is a technical challenge. For instance changing the length of one arm of the interferometer by 30 nm with respect to the other already introduces a temporal delay of 100 as. There are two established approaches in order to achieve such a stability: Passively stable setups where all mechanical components of the interferometer are carefully chosen and placed on a single-, temperature stabilized optical table within a vacuum chamber [74] or actively stabilized setups in which the length of one arm of the interferometer is actively adjusted with respect to the other by using a frequency-stable reference laser [75]. While it has been demonstrated that passively stable setups can provide a short-term stability of well below 100 as, long-term stability and repeatability cannot be guaranteed. Since a COLTRIMS apparatus needs to be operated at a count rate, which is lower than the laser repetition rate in order to avoid potential false coincidences, measurements generally can take much longer compared to other detectors. Therefore, the use of an active interferometer stabilization (AIS) is highly desirable for reliable pump-probe measurements.

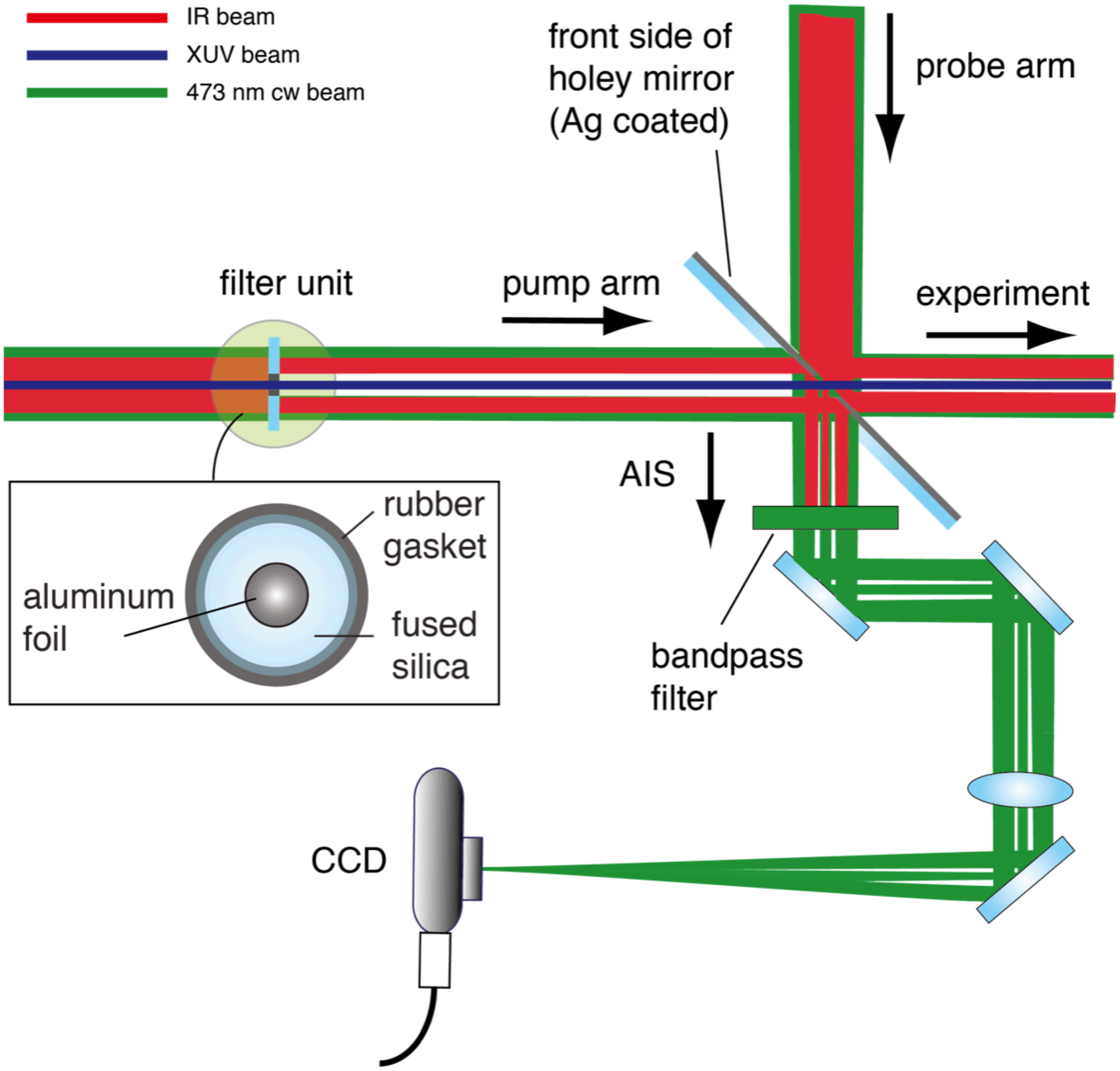
IR beam
XUV beam
473 nm cw beam
front side of holey mirror (Ag coated)
probe arm
filter unit
pump arm
experiment
AIS
rubber gasket
aluminum foil
fused silica
bandpass filter
CCD

Figure 6.3. Illustration of the beam paths for the AIS. The filter unit removes the central part of the IR beam and cw light in the pump arm. The remaining donut-shape beam is reflected by the rear side of the holey mirror. Here, it recombines with the light coming from the probe arm which passes through the hole of the mirror. After removal of the residual IR by the band-pass filter, the cw light is focused onto the CCD camera used to image the interference fringes. See the text for a more detailed description.

We have implemented such an AIS allowing the use of few-cycle pulses at 10 kHz repetition rate adapting some of the ideas mentioned by Chini et al. [75]. We use a continuous wave (cw) laser with a wavelength of 473 nm (Cobolt Blues, Cobolt AB) coupled into the interferometer via the 20 % beam-splitter (green beam path in Fig. 6.1). Both split parts of the beam are exposed to the same optics as the IR and finally recombine on the rear side of the holey mirror. The Al filter unit is designed to allow part of the cw laser to reach the rear side of the holey mirror and at the same time to prevent the generating IR beam from passing. As can be seen in the inset of Fig. 6.3, we use an Al foil mounted on a drilled fused silica ring. The donut-shaped cw- and IR beams are then reflected on the rear side of the holey mirror. Since the holey mirror has a substrate thickness of only 1 mm a substantial fraction of the cw beam in the probe arm passes through the hole. A bandpass filter at 470 nm with a bandwidth of 10 nm is then used to filter out the residual IR beam. In order to detect the interference pattern, the cw beams are subsequently imaged onto a charged-coupled device (CCD) camera. A home-built software stabilizes the spatial interference fringes by a feedback voltage to the piezo translation stage of the delay unit. With this approach we exclude any long-term drift and we can compensate for a potential hysteresis of the piezo. The AIS has also been characterized quantitatively as can be seen in Fig. 6.4. For this purpose, we have recorded the phase variation over approximately 7 h. The analysis reveals that the standard deviations is smaller than 60 as.

It is worth emphasizing that the implementation of our AIS is different from others reported so far. First of all we use a blue cw-laser at 473 nm instead of a Helium-Neon-Laser or a frequency-doubled green laser. The reason is the following: Provided that the reference laser is co-propagating with the IR it needs to be ensured that the IR can be filtered out. This allows imaging the interference pattern of the cw beam onto the CCD camera without a superimposed IR. The filtering can be achieved with a chopper which mechanically blocks the IR pulses at its repetition rate. Since choppers at 10 kHz produce significant vibrations we decided to use a cw laser at a frequency that does not overlap with the spectral region of the output of our hollow-core fiber compression setup. The use of a bandpass filter for the cw therefore allows blocking the IR pulses. Another important difference is that we have used a holey mirror with a thin substrate and a silver coating instead of a dielectric mirror as reported in reference [75]. This allows us to employ broadband, few-cycle laser pulses since the reflectivity of dielectric mirrors is limited to a relatively small spectral bandwidths.

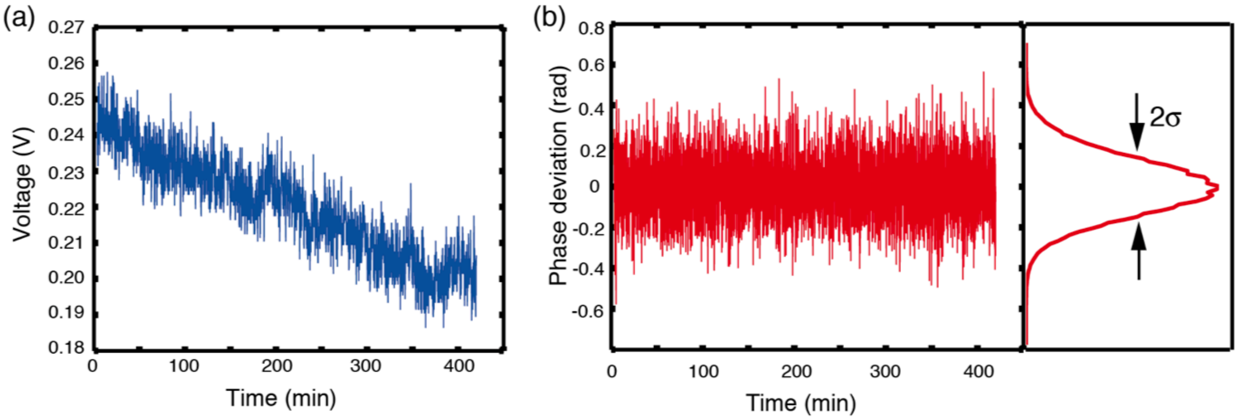

Figure 6.4. Characterization of the AIS. (a) Evolution of the control voltage applied to the piezo translation stage while operating the AIS over 7 h. (b) Phase variation of the recorded phase over the same time interval yielding a standard deviation of about 60 as.

6.5 XUV-IR pump-probe experiments and single attosecond pulse characterization

We generate APTs by focusing the linearly polarized IR beam into an Ar gas jet. For the generation of SAPs we employ a polarization gate [19] before generating the HH: By manipulating the polarization of the IR field with the help of a quartz plate and a broadband quarter-wave plate it is possible to confine the HHG to one half-cycle of the IR field and thereby to select only one SAP. For the pump-probe alignment we use the same optional mirror in the coupling chamber that also allows for the IR-only experiments described in section 6.3 (see Fig. 6.1). Turning it by 180° and removing the filter unit allows coupling out the IR pump and probe beams via the exit port P2. Both beams are subsequently imaged onto a CCD camera. The temporal overlap of the pulses from both arms is adjusted through the delay stage by monitoring the appearance of spectral fringes. The spatial overlap is achieved by the alignment of two motorized mirrors in the probe arm labeled as M1 and M2.

APTs and SAPs can be temporally characterized by two different measurement techniques namely the RABBITT (Reconstruction of Attosecond Beating By Interference of Two-photon Transitions) [6] and the attosecond streaking technique [7]. Both of them are experimentally similar, but their theoretical description relies on different approaches corresponding to different intensity regimes of the IR. In both methods, the collinearly propagating XUV and IR pulses (overlapping both in time and space) are focused into the (supersonic) gas jet of, e.g., noble gas atoms inside the COLTRIMS chamber. The gas is ionized by single photon excitations by the part of the XUV photon energies that lies above the ionization threshold. Thus, an (truncated) electron replica of the photon spectrum is generated. In the case of streaking, when pump and probe beams overlap in time, the IR beam, not intense enough to ionize the atoms, acts as an ultrafast phase modulator on the electron spectrum. Recording the modulated spectra as a function of the XUV-IR delay delivers a spectrogram (see Fig. 6.5), which can be used to extract the temporal properties of the XUV pulse(s). The IR energetically shifts the continuous electron spectrum by a value that is proportional to its instantaneous vector potential. This effect can be explained in a classical picture where the electrons experience a force given by the electric field of the laser. In the case of RABBITT, when pump and probe are not overlapping, the photon spectrum is characterized by discrete peaks at the harmonics positions. For small values of the XUV-IR delay, an oscillatory signal, so called sidebands (SB), appears between the main peaks. The SB signal results from the interference of two different excitation pathways involving the absorption of one harmonic photon and absorption or emission of one IR photon. The pathways interfere and give rise to an oscillatory signal with a frequency that is given by twice the IR carrier frequency. The group delay of the HH is encoded in the phase of the SB signal.

In the following we will present the temporal characterization of the SAPs produced in the COLTRIMS. As will be explained in the following, the first step is to define a filter on the measured 3D momentum distribution to ensure that the FROG-CRAB algorithm can be applied reliably.

Figure 6.5 illustrates the difficulty of extracting a streaking trace from a detector with 3D momentum resolution. In (a) the schematic of the electron momentum distribution generated by a broadband excitation pulse is shown (blue area). Here, $p_{\mathrm{perp}} = \sqrt{p_x^2 + p_y^2}$ with x being the beam propagation direction and z being the direction of the IR streaking polarization. Electrons of the same energy $E = \boldsymbol{p}_1^2 / 2m_{\mathrm{e}} = \boldsymbol{p}_2^2 / 2m_{\mathrm{e}} = \boldsymbol{p}_0^2 / 2m_{\mathrm{e}}$ can be emitted in different directions. If an IR streaking field is overlapped, the whole distribution is shifted according to the vector potential of the IR (equation (1.30)). Hence, electrons that share the same initial energy are shifted to differing final energies $\left(\boldsymbol{p}_1^{'2}/2m_\mathrm{e} \neq \boldsymbol{p}_2^{'2}/2m_\mathrm{e}\right)$. Consequently, in a streaking experiment electrons of the same initial energy would not exactly follow the vector potential. This in turn prevents a reliable reconstruction from the FROG-CRAB technique. To avoid this energy ambiguities one can define a small cone around the IR polarization axis (*z*-axis). Using only these electrons significantly reduce the above-mentioned effect. Besides this requirement there is also the need to restrict the analysis to either positive or negative values of p_z. This can be exemplarily seen in Fig. 6.5 (b): The electrons emitted to the left side loose energy while the other half gains kinetic energy if the distribution shift to the right.

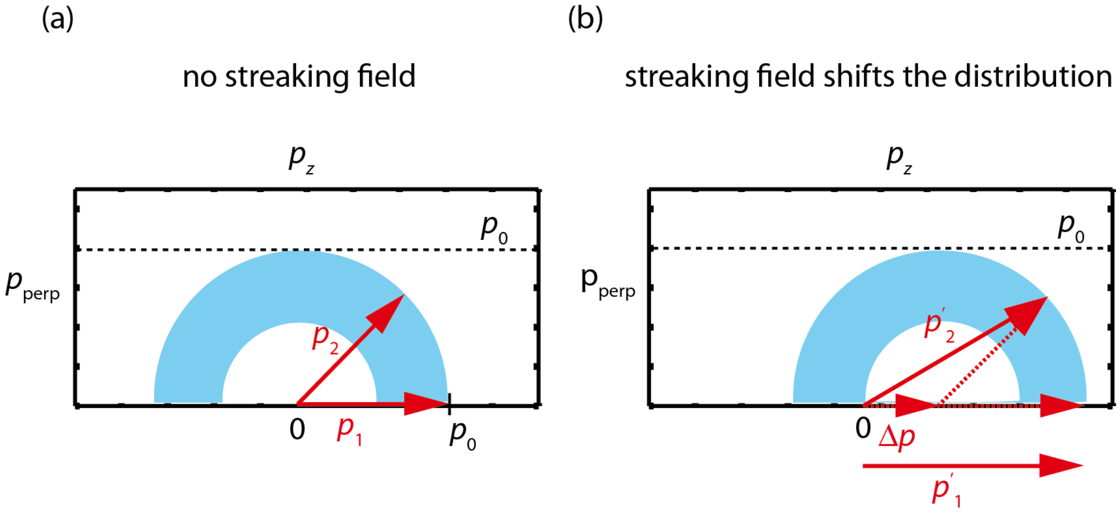

Figure 6.5. Schematic illustration of the 3D momentum distribution of electrons (blue shaded area) in attosecond streaking. In (a) the IR-unperturbed distribution is shown. Electrons of same energy can have momenta in different direction (red arrows). (b) If an IR field, polarized along the *z*-direction is overlapped, a momentum shift will be introduced leading to different final energies even though both electrons had the same initial energy.

The experimentally measured momentum distribution is shown in Fig. 6.6 (averaged over all delays in the streaking experiment). In reference [76] it has been shown that the phase retrieval from FROG-CRAB is still precise for cone angles up to $40°$. In the framework of this thesis the angle was therefore set to 40° which allows both, precise reconstruction of the phase and a maximum amount of usable counts for the streaking trace.

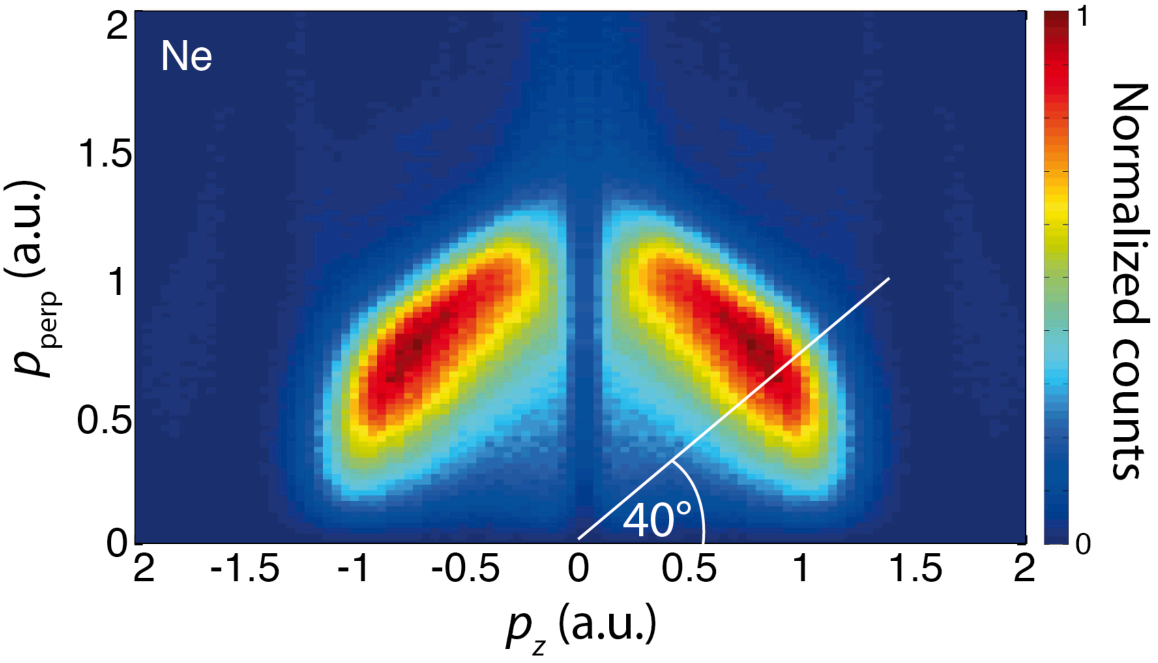

Figure 6.6. Momentum distribution of electrons in an attosecond streaking measurement conducted in Ne. The distribution contains all elections counts measured during the complete experiment. Here, z is the direction of the IR streaking polarization. For the extraction of the streaking trace, only those electrons are considered that lie within the illustrated 40° cone with positive values of p_z .

The above-mentioned procedure allows to extract the attosecond streaking spectrogram in Ne shown in Fig. 6.7 (a). Among the few existing reconstruction algorithms we chose the most established one called FROG-CRAB [56]. Similar to the classical FROG method [38] used for visible and IR pulses it is based on an iterative routine that generates a 2D streaking spectrogram, which converges to the measured data taking into account the constraints of the measurement process. One of the resulting quantities is the pulse's phase. As shown in Fig. 6.7 (d) the pulse has a duration of 280 as. The reconstruction also reveals that the pulses suffer from overcompensated chirp of about 16000 as^2 . Using a thinner Al foil in the XUV beam path would allow to compress the pulses closer to their transform-limit, which is about 165 as [77].

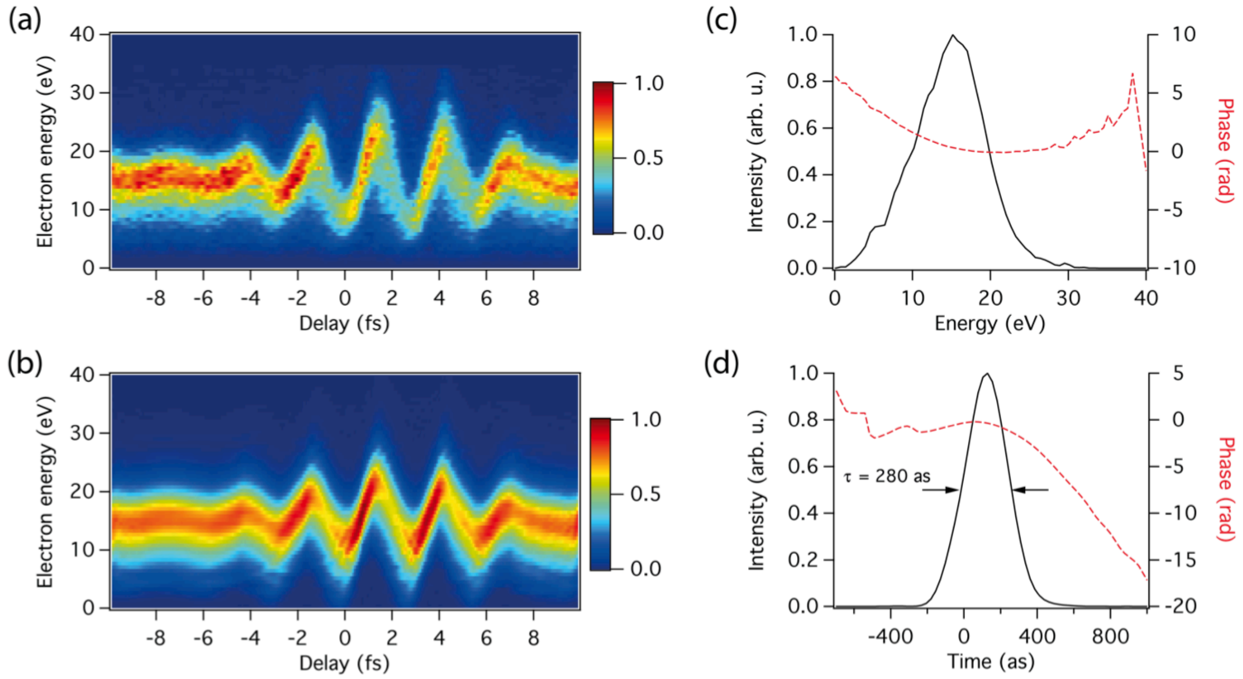

Figure 6.7. Reconstruction of a SAP produced with the AttoCOLTRIMS. (a) Attosecond streaking spectrogram measured with the COLTRIMS apparatus using Ar for the HH generation and Ne as the target gas. (b) FROG-CRAB reconstruction of the trace. (c) Reconstructed spectrum and phase of the pulse. (d) The time-domain representation reveals a pulse duration of 280 as with a GDD of $\sim 16000\,\mathrm{as}^2$.

Chapter 7

3D attosecond streak camera

In this chapter it will be demonstrated how the combination of attosecond streaking and a coincidence detection naturally allows to extract the rotating electric field vector of an elliptically polarized IR streaking light field in 3D.

7.1 Introduction

In conventional attosecond streaking experiments the electrons are detected in a TOF detector. These detectors are equipped with a skimmer in front of the MCP in order to only collect electrons within a small angle and thereby avoiding any ambiguities of the electron energies. In this configuration it is always preferential to choose both the XUV and the streaking field polarization such that they are parallel to the skimmer-MCP axis. This ensures best collection efficiency and highest energy streaking amplitudes. In the limiting case where the streaking polarization is perpendicular to the aforementioned axis there will not be any measurable streaking effect. In a COLTRIMS apparatus the electron momenta are measured within the full solid angle. The latter allows streaking to be measured equally in every direction. Using this principle the complete time-dependent polarization state of the streaking field can be characterized.

7.2 Ellipticity adjustment via above threshold ionization

In a proof-of-principle experiment the polarization of the IR has to be modified to generate elliptically polarized pulses. This can be done using broadband polarization optics which are commercially available. In the setup presented within this thesis these have to be placed before the recombining holey mirror (see Fig. 6.1). An initially close to circular polarized pulse therefore will be strongly modified after being reflected from the 45° holey and grazing incidence toroidal mirror. Therefore, in the experiment we have used a combination of a $\lambda/4$- and a $\lambda/2$-plate. The latter allows to partly compensate for the effects on the IR polarization of the optics following the holey and toroidal mirrors.

For a fast but rough characterization of the degree of ellipticity, we made use of a multi-photon effect known as Above-Threshold Ionization (ATI). Here, atoms are ionized by the simultaneous absorption of several photons thereby generating electrons and ions which are detectable with the COLTRIMS apparatus. This effect scales nonlinearly with the peak intensity of the IR pulses which was set to generate sufficient ATI signal. Therefore, to obtain an elliptically polarized field the ATI signal needs to be minimized with the help of the wave plates, ensuring the highest degree of ellipticity.

7.3 Resolving the rotating electric field vector in 3D

Using the above-mentioned procedure to obtain elliptically polarized IR pulses we have then performed an attosecond streaking measurement to retrieve the vector potential of the IR. Here, the liberated electrons are accelerated by the force $\boldsymbol{F}_{\mathrm{el}} = -e\boldsymbol{E}_{\mathrm{IR}}(t)$ according to the IR field $\boldsymbol{E}_{\mathrm{IR}}(t)$ at the instant of ionization. Hence, depending on their time of birth t_0 the final electron momenta are given by

$$\boldsymbol{p}(t_0) = \boldsymbol{p}_0 - \frac{e}{m}\int_{t_0}^{\infty} \boldsymbol{E}_{\mathrm{IR}}(t)\,dt = \boldsymbol{p}_0 - \frac{e}{m}\boldsymbol{A}_L(t_0), \tag{2.3}$$

where e is the electron charge, m is the electron mass, $\boldsymbol{p}_0$ is the initial momentum of the electron and $\boldsymbol{A}_{\mathrm{L}}(t_0) = \int_{t_0}^{\infty} \boldsymbol{E}_{\mathrm{IR}}(t)\,dt$ is the vector potential at the moment of birth of the electron. Performing a center-of-mass (COM) analysis on the streaking traces along each momentum component of the electron spectra therefore allows identifying $-(e/m)\boldsymbol{A}_{\mathrm{L}}(t)$ approximately as the oscillation around the central momentum $\boldsymbol{p}_0$.

Figure 7.1 shows the *y*- and *z*- components (IR polarization plane) of the electron momentum distribution as a function of the SAP-IR delay. Both components are retrieved by a COM analysis (Fig. 7.1, open circles). A phase shift close to 90° between the two traces already indicates the elliptical nature of the polarization.

Quantitatively we have extracted an ellipticity of $\varepsilon = 0.69$ and an angle $\beta = 104.5^\circ$ of the ellipse`s major axis relative to the p_y-axis by fitting an analytic expression to the data (Fig. 7.1, solid line).

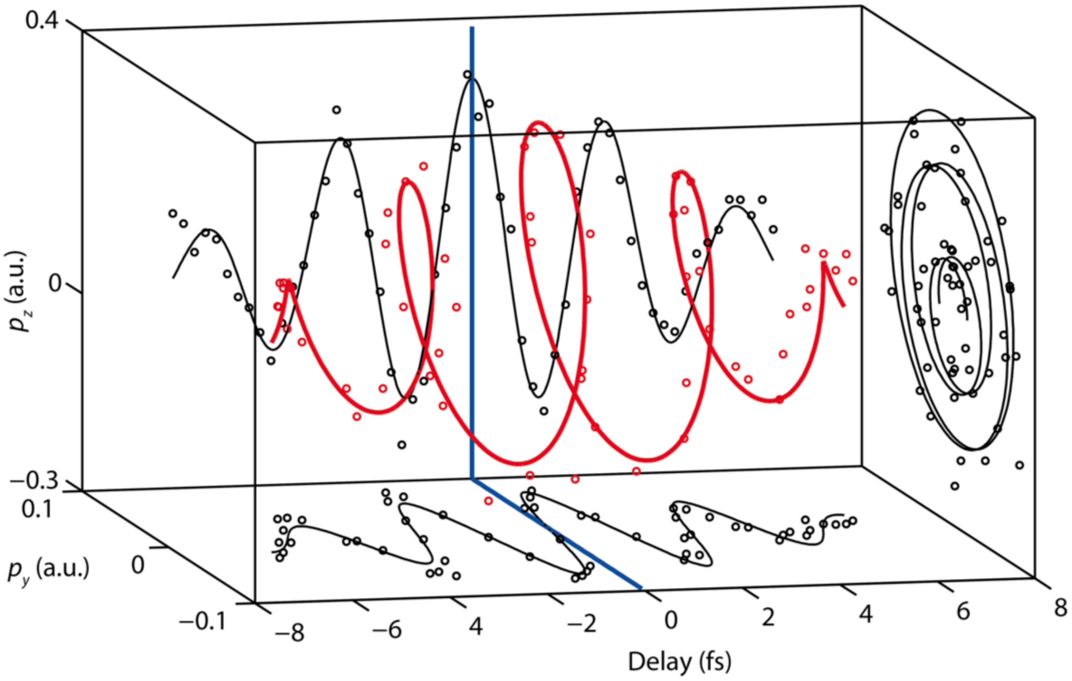

Figure 7.1. 3D reconstruction of the vector potential of an elliptically polarized few-cycle IR pulse by attosecond streaking in the COLTRIMS apparatus. The red circles/line show the motion of the COM of the electron distribution modulated by the IR pulse. The projection of the oscillations is presented in black. The expected phase shift of about 90° between the y- and z- component of the light field can already be seen from the blue lines drawn at a delay position of 0 fs.

7.4 Conclusion

This method can easily be extended to more complex electric field configurations with time-dependent polarization states, as there are no constrains to the IR pulse shape. This allows for a range of novel studies in which the influence of time-dependent polarization can be investigated. It is worth to emphasize that in this way attosecond streaking studies can be performed on atomic and molecular targets while the polarization at the instant of ionization is recorded simultaneously using a second target as for example Ne.

Chapter 8

Attochirp-corrected ionization time delays using coincidence spectroscopy

Recent measurements have demonstrated the possibility of probing single-photon ionization time delays of electrons originating from different initial states [1,4]. Within this thesis the importance of the temporal structure of the ionizing single attosecond pulse (i.e. attochirp) in the extraction of time delays in attosecond streaking experiments has been shown for the first time. We have demonstrated this by measuring the time delay between valence electrons from different atomic species by combining attosecond streaking with a coincidence detection scheme. This novel technique allows for the simultaneous measurement of both species under identical conditions. We find that the attochirp introduces an artificial time delay that may exceed the atomic time delay and present a general procedure, which corrects for this contribution. Our analysis, exemplarily applied to argon (Ar) and neon (Ne), reveals an energy-dependent atomic time delay of a few tens of attoseconds in agreement with theoretical predictions.

The chapter is organized as follows. First the concept of Eisenbud-Wigner-Smith time delays is introduced. This allows for the further discussion of the time delays measured in attosecond streaking. Thereafter, the delay extraction from attosecond streaking in the context of the attochirp and ionization cross-sections is explained. Finally, the results for Ar and Ne are presented and discussed.

8.1 Introduction and motivation

In recent years, the great progress in ultrafast science has lead to the generation and application of extreme ultraviolet (XUV) attosecond pulses, which allow initiating, controlling and probing electron dynamics in atomic and molecular systems [44,45]. Today, researchers are able to address one of the most fundamental questions in quantum mechanics: How fast can light remove a bound electron from an atom, a molecule or a solid target [1,3]?

The three main experimental techniques that have addressed this question are the attoclock [71], attosecond streaking [7] and RABBITT (reconstruction of attosecond beating by interference of two-photon transitions) [6,78]. The attoclock is a method well suited to study fundamental attosecond dynamics like strong-field ionization in the multi-photon and tunneling regime. It has been employed to estimate the tunneling delay time in helium [5,79] since it allows to access the instant in time when the tunneling process starts (i.e. time zero) with very high accuracy. The clock is provided by the rotation of the elliptically polarized laser light with a defined period. Time zero is defined as the moment in the laser cycle when the tunnel probability is highest. For elliptical polarization this occurs when the electric field points along the major axis of the polarization ellipse. Instead, attosecond streaking and RABBITT are based on single-photon ionization, realized in a pump-probe scheme where the XUV attosecond pulses (pump) ionize the target and interaction of the freed electrons with an IR pulse (probe) provides the timing information of the ionization process. In these measurements the time zero, i.e. the exact instant in time when the XUV pump triggers ionization, is generally unknown. However, relative timing information between electrons, e.g., originating from different states, can be extracted.

In attosecond streaking, the measurement consists of recording the final momenta of the photoelectrons after their ionization by a single attosecond pulse (SAP) and interaction with a few-cycle IR probe pulse for different SAP-IR time delays [7,10,55]. Depending on the value of the IR vector potential at their release time, the photoelectrons are accelerated to different final momenta, thus mapping the temporal structure of the IR onto the electron energy (see section 4.2).

For a long time, one of the most important applications of attosecond streaking was the complete characterization of the SAP by extracting the XUV spectrum and phase via a retrieval algorithm, called Frequency-Resolved Optical Gating for Complete Reconstruction of Attosecond Bursts (FROG-CRAB) [56,80]. However, two different spectrograms recorded simultaneously and composed by different types of electrons, for instance originating from different states of the same target or from different targets, can also yield relative timing information about the atomic photoionization time delay, even without the knowledge of the time zero, which represents the moment in time, when the ionization process is initiated. Pioneering experiments conducted on solids [3] or gas targets [1] reveal unexpected time delays. In Ref. [1] a time delay in atomic photoemission of about 21 as has been extracted between electrons emitted from the 2s and 2p shells of Ne. Theoretical calculations based on different approaches predict such a delay to be on the order of 10 as [1,81,82]. The discrepancy is still part of ongoing discussions and constitutes a starting point of our investigation.

In this chapter, we discuss for the first time the role of the temporal structure of the ionizing single attosecond pulse (i.e. attochirp) in the extraction of photoionization time delays. For this purpose, we have measured the photoionization time delays between valence electrons originating from different atomic species using a novel attosecond streaking technique relying on coincidence detection. The approach is based on a reaction microscope, also known as a COLd Target Recoil Ion Momentum Spectroscopy (COLTRIMS) detector [8,9], in combination with a gas target containing a mixture of both species. The coincidence detection allows assigning the electrons to their parent ion, thereby enabling the extraction of two streaking traces out of one single measurement. This ensures that systematic errors in the comparison of photoionization time delays from the two species are significantly reduced since electrons ionized from both gases are exposed to the same XUV and IR fields.

8.2 The Wigner time delay

Revealing experiments in recent years have shown that photoemission is not an instantaneous process [1,4]: The electron wavepacket formation is delayed relative to instant of excitation. But how can these delays be described theoretically? Photoemission can be understood as half a scattering process in which the entrance channel is not a continuum but a bound state with an exit channel corresponding to the freed electron. In a paper from 1955 [83] Eugene P. Wigner addressed the scattering of waves. He showed that the time delay associated with the scattering process is given by the derivative of the acquired phase shift η with respect to its energy E: $\tau_W = 2\hbar\partial\eta/\partial E$ (group delay). For photoemission the Wigner time reduces to half of this value

$$\tau_W = \hbar\frac{\partial\eta}{\partial E}. \tag{2.4}$$

In a simplified but intuitive example for scattering the ionic potential can be modeled as a potential well. The corresponding time-independent Schrödinger equation (TISE) reads

$$\left(-\frac{\hbar}{2m}\frac{d^2}{dx^2}+V(x)\right)\psi(x)=E\psi(x). \tag{2.5}$$

The analytic solution for continuum states can be found in text books as e.g. [84]. In Fig. 8.1 the solution $\psi(x)$ is plotted for a wave entering from the left (blue line) together with the wave function of a free electron (red line). The potential well obviously introduces a scattering phase shift η from which the time delay can be extracted using equation (2.4).

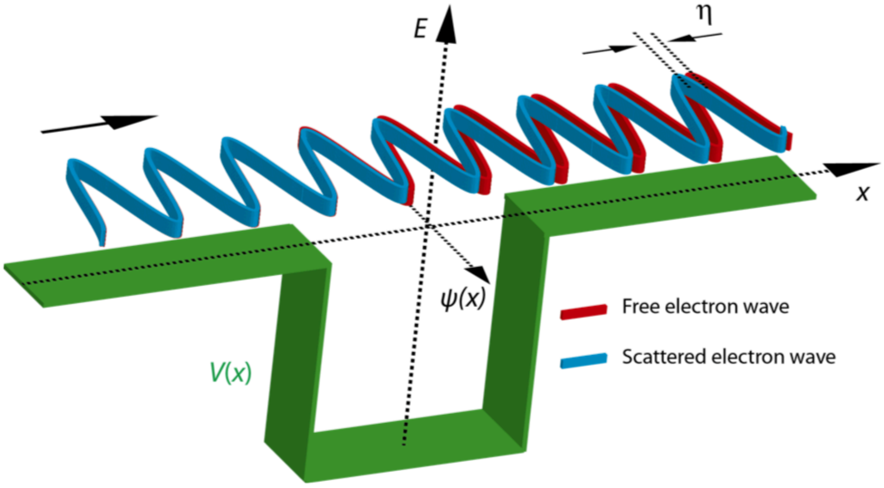

Figure 8.1. Photoemission process modeled with a potential well. Solving the TISE for scattering of an electron entering from left yields the blue result. The potential well introduces a phase shift η onto the scattered relative to the free wave function (red line).

The recent development of attosecond sources allowed to access these time delay by the use of pump-probe schemes based on an attosecond XUV- and a delayed IR pulse. The two techniques used in this context are the attosecond streaking and the RABBITT. The following discussion will focus on the attosecond streaking which has been the method used in the scope of this thesis.

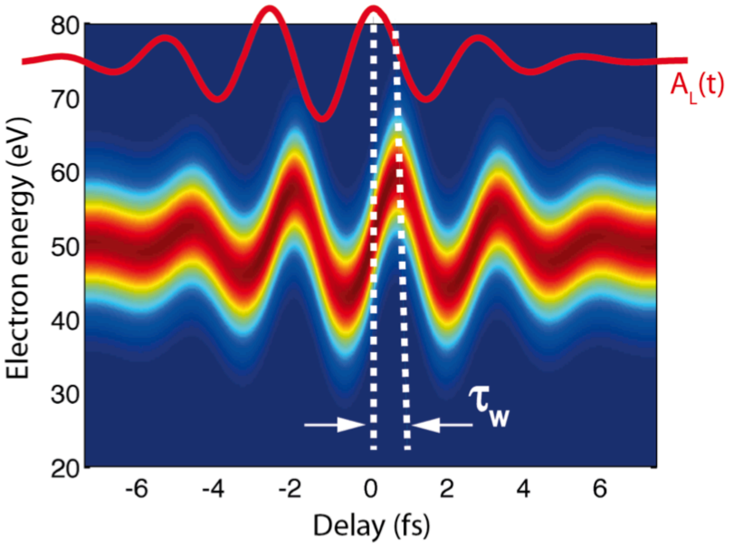

Figure 8.2. Extraction of time delays from attosecond streaking assuming a short-range Yukawa-potential. It can be shown that in this case the Wigner delay τ_W is given directly by the difference of the vector potential A_L and the streaking trace itself.

The intriguing experiments that have been conducted on this topic have triggered extensive theoretical investigations leading to the successful development of new concepts for solving the time-dependent Schrödinger equation (TDSE) [85]. As has already been discussed in section 4.2 in attosecond streaking an attosecond pulse liberates electrons which are subsequently exposed to the IR field. The latter modulates the electron momenta leading to a final energy proportional to the vector potential at the instant of ionization. In the discussion of section 4.2 it was assumed that the ionization process occurs instantaneously. Taking the finite ionization time into account a delay between the vector potential and the modulation of the electron spectrogram is expected (see Fig. 8.2). However, as was shown in reference [86] this only holds for a short-range potential. Simulation considering also the long-range Coulomb tail demonstrated a relatively large contribution originating from the coupling of the streaking field with the long-range potential which was dubbed τ_{CLC}.

Fortunately, this contribution can be calculated and it turned out to be universal for Coulomb potentials, where the only parameters that enter are the net charge of the ion, the final electron energy and the central frequency of the streaking field.

Since in experiments the exact temporal position of the IR vector potential is unknown, it is impossible to extract the absolute Winger time for the photoemission of a single electron. Instead in references [1,4] the Wigner delay difference of electrons of different subshells within an atom have been addressed.

8.3 Experimental setup

For the coincidence attosecond streaking experiments we have used the setup described in chapter 6. Here, waveform controlled few-cycle IR laser pulses of approximately 5 fs are coupled into an interferometer through a beam-splitter of 20%. The 80% portion is used to generate SAPs (pump) while the other part (probe) is used as a streaking field. The SAPs are generated by the polarization gating technique [19] and are typically centered at about 35 eV with a bandwidth of 10 eV. The XUV-pump beam is first recombined with the IR-probe through a holey mirror. A translation stage in the probe arm allows to control the delay between both pulse. After the holey mirror both beams are collinearly focused by a toroidal mirror into the supersonic gas jet of a COLTRIMS detector. Here, ions and electrons are separated by the electric field of its spectrometer and guided towards space and time sensitive detectors. This allows to retrieve the full momentum vector - and therefore the kinetic energy - of each individual particle at the moment of ionization. Thus, applying a filter to the time-of-flight of the parent ions as well as to the momentum sum of ions and electrons allows for coincidence detection.

In the measurements presented in this chapter, the coincidence technique enables to distinguish between electrons generated from Ar and Ne even though they energetically overlap. Figure 8.3 (a) shows the streaking trace that is obtained when all electrons are measured that are emitted from both species within a cone of 40° (Fig. 6.6), which cannot be used to extract any meaningful timing information. However, assigning each electron to the corresponding parent ion (Ar^{+} or Ne^{+}) allows obtaining separate streaking traces for each species (Fig. 8.3 (b)) from which a relative time delay in photoionization can be retrieved.

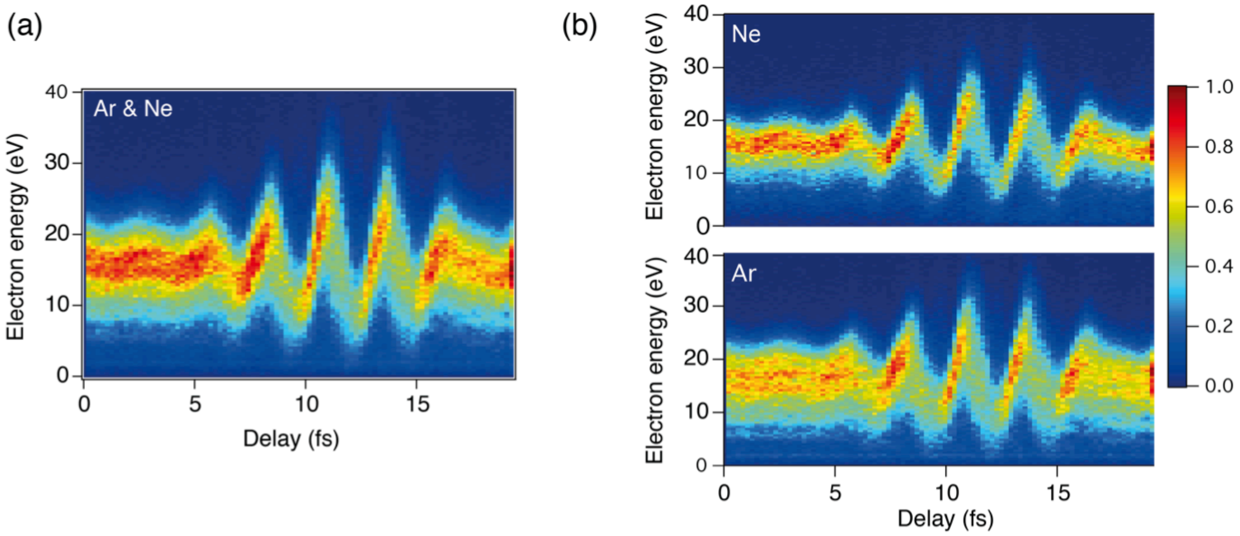

Figure 8.3. Attosecond coincidence streaking. (a) Streaking photoelectron spectrogram obtained from photoelectrons originating from simultaneous ionization of Ne and Ar streaked by an IR intensity of about $3\cdot10^{12}$ W/cm^2. Only those electrons are considered that lie within an cone angle of $40°$ with positive values of p_z. (b) If each photoelectron is assigned to its parent ion by applying a coincidence filter, two separate streaking spectrograms are obtained.

8.4 Time delay extraction from attosecond streaking

Based on our coincidence streaking measurement on Ar and Ne we will show in this section that time extraction from attosecond streaking is not straightforward. We will review different methods that have been applied so far and we will point out the missing treatment of the attochirp.

In a first intuitive approach, the timing information is readily obtained by quantifying the relative shift between the two streaking spectrograms along the time axis. This was adopted from [3] and is illustrated in Fig. 8.4 (a). More quantitatively, for each delay step and target atom species, we calculate the center-of-mass (COM) of the photoelectron energy spectrum between 0 and 40 eV. The result of this procedure is shown in Fig. 8.4 (b). The photoionization time delay between the two species can be extracted from the phase differences obtained by an analytic fit to the COM oscillation. This yields a time delay $\Delta\tau^{\mathrm{Ar/Ne}} \doteq \tau^{\mathrm{Ar}} - \tau^{\mathrm{Ne}}$ of about -113 as. The sign indicates that the emission of photoelectrons from Ne is delayed relative to that from Ar. The analysis based on the COM returns a time delay $\Delta\tau^{\mathrm{Ar/Ne}}$, which is expected to correspond to the spectrally weighted average value. However, in the following we will show that in general this resulting time delay might be meaningless.

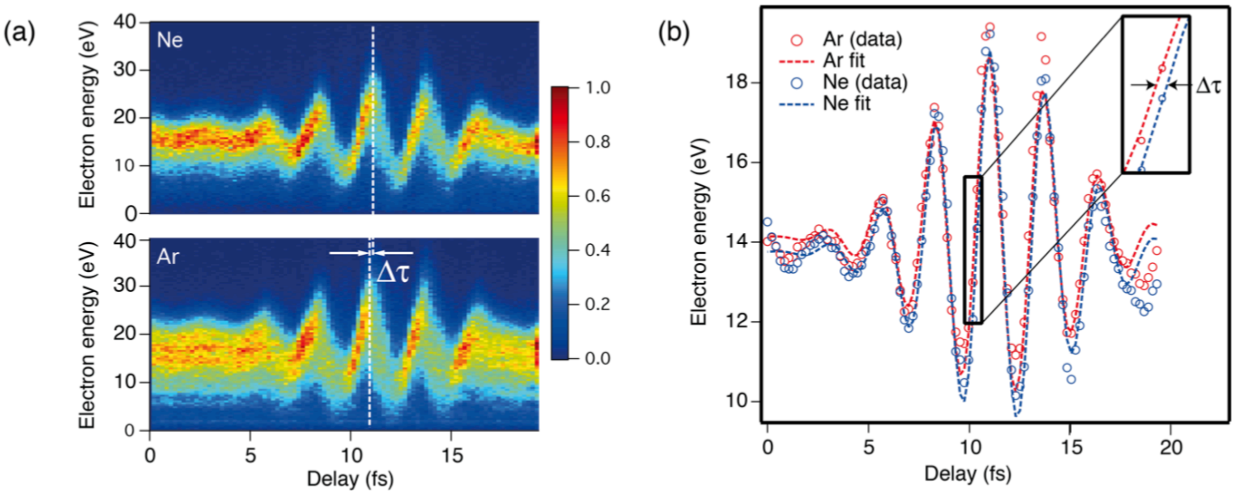

Figure 8.4 Time delay extraction from two traces obtained from coincidence streaking. (a) Simultaneously measured streaking traces for Ar and Ne obtained by applying a coincidence filter. An apparent time shift $\Delta\tau$ can be retrieved by comparing the delay position of the central maximum. (b) Time dependent COM energy shift extracted from the spectrograms (open circles) for Ar (red) and Ne (blue) with corresponding fit (dashed line).

It is often assumed that the photoelectron spectrum is a replica of the XUV spectrum, just shifted in energy by the ionization potential of the target. However, this conclusion can only be drawn if the spectral response (cross-section) of the target across the complete bandwidth of the ionizing pulse shows a uniform behavior. In general, the absorption cross-section is non-uniform, leading to preferential absorption of photons at certain energies. As a consequence, the resulting COM of the photoelectron spectrum can be shifted in energy. The photoionization cross-sections σ_{Ar} and σ_{Ne} are known from literature [87] and have been plotted in Fig. 8.5 (a). It can be clearly seen that the Ar cross-section exhibits a strong non-uniform behavior for the photon energies of interest. Therefore, the measured peak of the Ar photoelectron distribution is expected to shift to lower energies compared to the case of a uniform cross-section. We have used the FROG-CRAB algorithm to reconstruct the photoelectron spectra unperturbed by the IR for both species from the spectrogram shown in Fig. 8.4 (a). The resulting spectra are presented in Fig 8.5 (b) as a function of the energy of the ionizing photon by adding the corresponding ionization potential to the kinetic energy spectrum of the electrons (Ar: red solid line, Ne: blue solid line). As expected due to the non-uniform cross-section of Ar the peaks of the two uncorrected distributions do not overlap. However, if the corresponding photoabsorption cross-sections are taken into account, the corrected spectra, shown with dashed lines in Fig. 8.5 (b), look very similar: Both peak at about 37 eV and show comparable bandwidth.

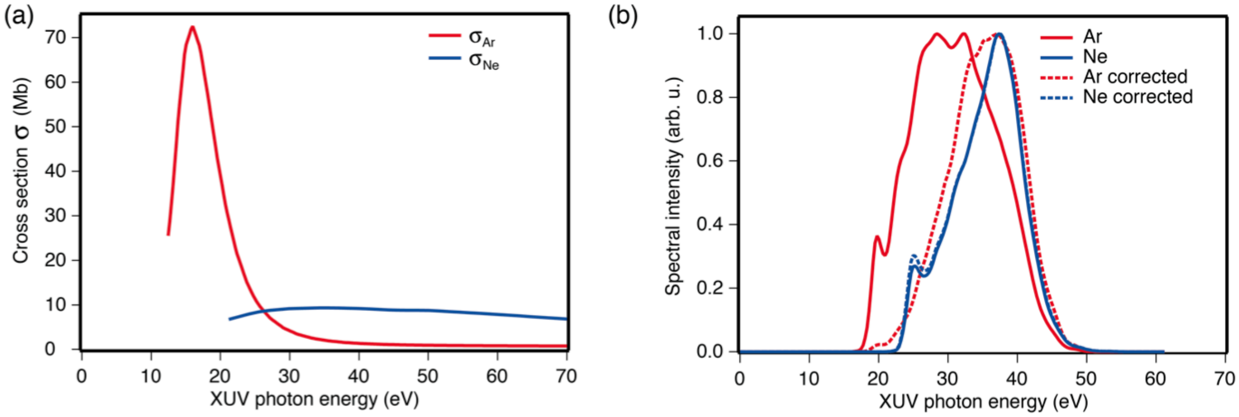

Figure 8.5. Influence of the ionization cross-section on the electron distribution of Ar and Ne. Cross-sections and electron spectra as retrieved by applying the FROG-CRAB algorithm to the data shown in Fig. 8.4 (a). (a) Ionization cross-section of Ar (red line) and Ne (blue line). (b) Photoelectron spectra of Ar (blue solid line) and Ne (red solid line) as retrieved by the FROG-CRAB algorithm. If the corresponding photoabsorption cross-sections (Fig. 8.5 (a)) are considered, the corrected spectra (red dashed line for Ar, blue dashed line for Ne) are similar and in particular peak at the same XUV photon energy of about 37 eV.

From the above discussion we can conclude that the COM of the two streaking traces does not correspond to the same photon energy if the photoionization cross-section shows a significant dependence on photon energy. Consequently, a chirped attosecond pulse can lead to artificial delays. By definition, photons of certain energies appear in a chirped pulse at earlier instances in time than others. Comparing electrons that have been ionized from photons of different energies therefore corresponds to starting the attosecond streak camera (or the 'clock' of the experiment) at different instances in time. Remarkably, even a small attochirp can cause a significant error in the determined time delay. An estimate shows that, for electron liberated by photons separated by 7 eV, a relatively small attochirp of $2000\,\mathrm{as}^2$ introduces a time delay of more then 20 as, which is on the order of the expected physical delay [86,88]. The COM analysis is therefore not appropriate for time delay extractions.

Fortunately, the previously mentioned FROG-CRAB technique allows an alternative route to access time delays from a streaking measurement by exploiting both the electron spectrum and its phase φ. As we will show in the following discussion this method is capable to extract correct time delays provided that the attochirp is taken into account.

In the pioneering work of Schultze et al. [1] it was shown that the group delay difference

$$\Delta\tau_g(\omega)=\frac{\partial\varphi^{\mathrm{Ar}}}{\partial\omega}-\frac{\partial\varphi^{\mathrm{Ne}}}{\partial\omega}=\left[\tau_0^{\mathrm{Ar}}-\tau_0^{\mathrm{Ne}}\right]+\left[\mathrm{GDD}^{\mathrm{Ar}}-\mathrm{GDD}^{\mathrm{Ne}}\right]\cdot(\omega-\omega_0)+\ldots, \qquad (2.6)$$

accessible through the electron phase $\varphi(\omega)$, coincides with the time delay between the two traces. Here, $\omega = E/\hbar$ is the electron angular frequency, $\tau_0 = \partial\varphi/\partial\omega\big|_{\omega_0}$ is an arbitrary time zero and $\mathrm{GDD} = \partial^2\varphi/\partial\omega^2\big|_{\omega_0}$ is the group delay dispersion.

However, in reference [1] the temporal structure of the pulse has not been taken into account. As the above-mentioned example has demonstrated this can lead to systematic errors in the time delay extraction. In the next section we will show how this problem can be solved.

8.5 Attochirp-corrected time delays from coincidence streaking

The SAPs used for the Ar-Ne coincidence streaking measurement exhibit a relatively strong chirp. Similar pulses have been used before in the FROG-CRAB reconstruction in section 6.5. It was shown that the GDD amounts about $16000\,\mathrm{as}^2$. This value makes the SAPs very suitable for the demonstration of its influence on the time delay extraction.

In the following we will extend FROG-CRAB method in [1] to account for the temporal structure of the pulse. Following reference [1], we first fed the FROG-CRAB algorithm with a matrix containing both, the Ar and the Ne trace and extract the group delays. The traces were patched together at an arbitrarily chosen energy of 40 eV in order to use one common energy axis. The reason for this procedure is twofold. First, it assures the same reconstructed IR vector potential for both traces consistent with the simultaneous measurement. Second, due to the ambiguity of the time zero τ_0 in FROG reconstructions this ensures that at least the same arbitrary value is used for both traces. After the reconstruction, the spectra and phases are disentangled at their patched energy of $40\,\mathrm{eV}$ by shifting the Ne data back to its original spectral position. The result of the FROG-CRAB analysis is shown in Fig. 8.6 (c) and can now be used to extract time delays. For both target atoms the slope of the group delay curve is quite steep, on the order of $25\,\mathrm{as/eV}$, indicating that the XUV pump pulse has a relatively strong chirp.

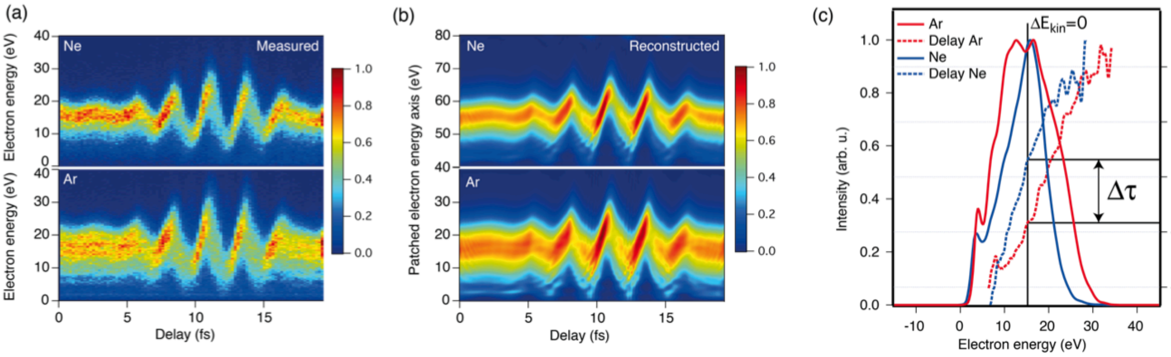

Figure 8.6. FROG-CRAB reconstruction of time delay between Ar and Ne. Measured (a) and reconstructed (b) spectrograms for Ne and Ar photoelectrons; before running the retrieval algorithm the two traces are patched together onto a common energy axis in order to ensure consistency in the reconstruction (see main text). (c) Retrieved spectra (solid lines) and group delay (dashed lines) of the photoelectron wavepacket for Ar (red) and Ne (blue). The vertical and horizontal black lines indicate that comparing the group delays for both species at the same photoelectron energy results in a time delay $\Delta\tau^{\mathrm{Ar/Ne}} \approx -100\,\mathrm{as}$.

At this point it is tempting to pursue the approach presented in [1] and compute a time delay $\Delta\tau^{\mathrm{Ar/Ne}}$ between the two species either for photoelectrons having the same kinetic energy $\Delta E_{\mathrm{kin}} = E_{\mathrm{kin}}^{\mathrm{Ar}} - E_{\mathrm{kin}}^{\mathrm{Ne}} = 0$ or at the peak of the photoelectron spectra as indicated in Fig. 8.6 (c). However, it was already shown with the help of Fig. 8.5 that this procedure does not guarantee that Ar and Ne photoelectrons have been ionized by XUV photons of the same energy and therefore it does not eliminate the contribution of the attochirp. This method of extracting time delays is equivalent to the one presented above based on the COM analysis; indeed, the value $\Delta\tau^{\mathrm{Ar/Ne}} = -117\,\mathrm{as}$ that we have obtained at the photoelectron spectrum peak position of about 15 eV using this method agrees well with the estimation obtained by the COM analysis that yielded $\Delta\tau^{\mathrm{Ar/Ne}} = -113\,\mathrm{as}$.

The key to the attochirp-corrected time delay extraction is to compute $\Delta\tau^{\mathrm{Ar/Ne}}$ at the same XUV photon energy, such that $\Delta E_{\mathrm{XUV}} = 0$ even if $\Delta E_{\mathrm{kin}} \neq 0$. The photoelectron spectra and group delays depicted in Fig. 8.6 (c) are therefore first shifted in energy according to the different ionization potential of the two species (Fig. 8.7 (a)), thus retrieving the 'quasi photon spectra' as shown in Fig. 8.5. Then, for any photon energy, the difference between the group delays extracted for Ar and Ne is calculated, resulting in an energy-dependent group delay curve presented in Fig. 8.7 (b). For the considered energy range the computed difference $\Delta\tau^{\mathrm{Ar/Ne}}$ is positive indicating that the emission of Ar-photoelectrons is delayed with respect to the emission of Ne-photoelectrons - a result opposite to the one obtained by the flawed COM method.

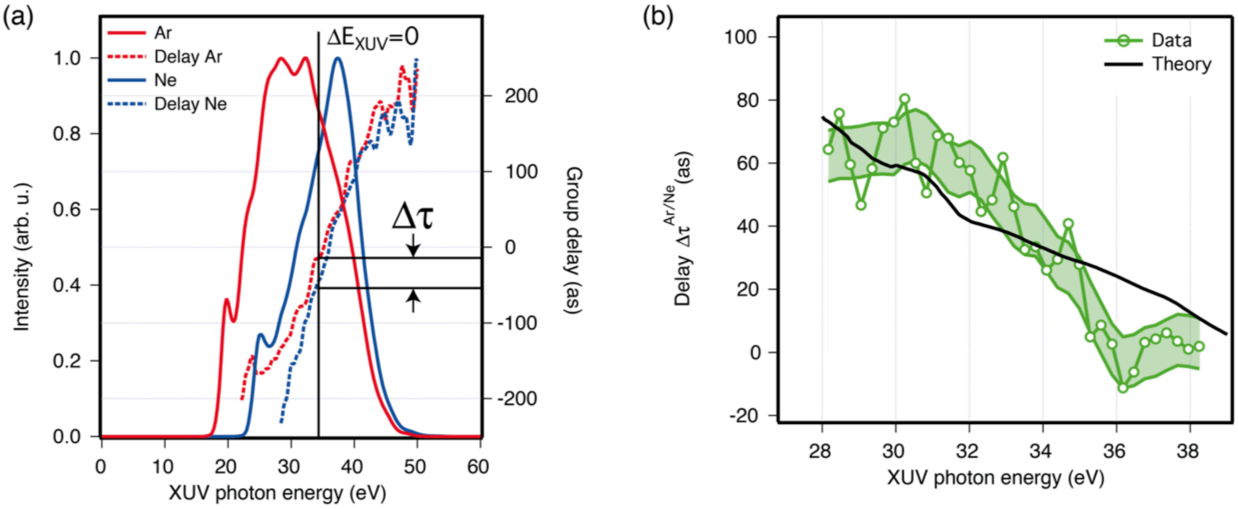

Figure 8.7. Ionization time delays reconstructed from FROG-CRAB. (a) XUV spectra (solid lines) and group delays (dashed lines) for Ar (red) and Ne (blue) computed from the reconstruced streaking spectrograms shown in Fig. 3 (c) adding the ionization potential of the two targets. (b) For any XUV energy within a range where the spectral intensity of Ar and Ne spectra overlaps (between 28 and 38 eV), a time delay $\Delta\tau^{\mathrm{Ar/Ne}}$ is calculated for a total number of 33 independently measured traces. The green band represents the one-sigma confidence interval of the reconstructed time delays using smoothed streaking traces, which agrees well with the mean value extracted from the noisy raw traces (green open circles). The black solid line is a theory curve obtained by computing the contributions of one-photon matrix elements within the random-phase approximation (RPAE) [81] and of the continuum-continuum laser driven transition [89] for both gas targets.

The energy-dependent photoionization delays extracted with our method are in good agreement with theoretical predictions, as shown in Fig. 8.7 (b). The theory curve is obtained by computing the difference between the atomic delays τ_{atomic} for Ar and Ne. The atomic delays in turn are calculated by adding the contributions given by the one-photon dipole matrix element [81], representing the Wigner photoionization time delay τ_{W} [83,90], and the continuum-continuum delay τ_{cc} representing the measurement-related time delay induced by laser-driven transitions connecting two continuum states [89]. Even though the τ_{cc} contribution was originally introduced to describe two-photon transitions involving only one IR photon, recently, it has theoretically been shown that this contribution remains the same even if more IR photons are involved [91,92].

8.6 Influence of data processing on time delay extraction from FROG-CRAB

For the results presented in this chapter a total amount of 33 patched Ar/Ne traces has been measured and analyzed. This large number of traces has been only possible at the expense of long integration time. Hence, the statistics in each of the measurement is not as good as in the sample measurement presented throughout this chapter.

Figure 8.8 presents the resulting delay for one arbitrarily chosen patched trace if different filters are applied. We have tried in total three filters to reduce the noise of the resulting time delays and to improve the convergence of the algorithm:

1. Low-pass filtering of spectra:
   The spectra at each delay position have been smoothed applying a Savitzky-Golay-filter.

2. Low-pass filtering of the reconstructed attosecond pulse:
   After each iteration step the attosecond pulse has been smoothed using a low-pass Fourier filter (avoiding possible unphysical high frequency oscillations).

3. Low-pass filtering of the reconstructed gate (vector potential):

> After each iteration step the gate has been smoothed using a low-pass Fourier filter (avoiding possible unphysical high frequency oscillations).

In the following a notation is introduced consisting of three binary digits to simplify the assignment of the applied combination of filters: e.g. 110 stands for the application of filters 1 and 2 only.

As can be seen in Fig. 8.8 the low-pass filtering of the spectra (red curves) allows to reduce the noise significantly, whereas the influence of the other filters is rather negligible.

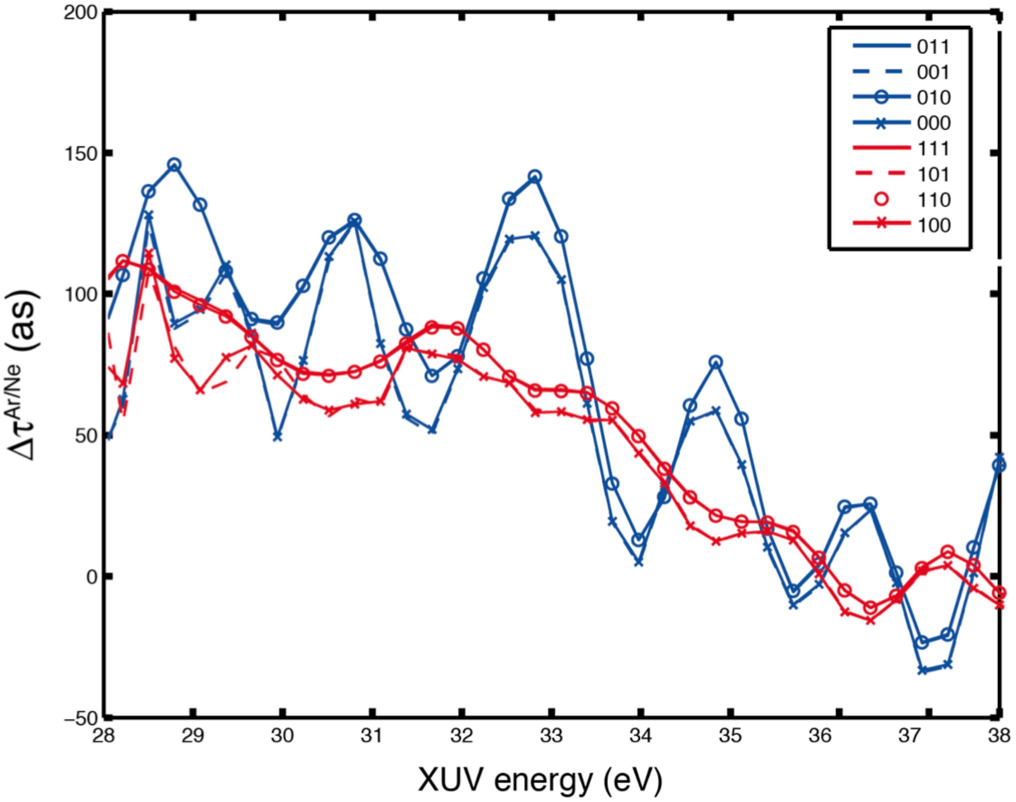

Figure 8.8. Time delays for an arbitrarily chosen patched trace from the dataset containing 33 traces.

The open circle result in Fig. 8.7 (b) corresponds to the time delays obtained taking the average value of all 33 measured traces without any filter (000) and the green band represents the one-sigma confidence interval of the reconstructed time delays using smoothed streaking traces according to the different filters shown in Fig. 8.8. Since both results are in agreement we can conclude that smoothing of the data is not necessarily needed if the large number of 33 traces are analyzed.

8.7 Discussion

In conclusion, we have used a novel scheme to access photoionization time delays using the unique capabilities of a COLTRIMS detector. We have presented a detailed description of how to extract photoionization time delays between electrons from different states or species when attosecond streaking is employed. In particular, we have shown that any existing chirp of the a SAP manifests itself in the same way as the atomic photoionization time delay and therefore can lead to wrong interpretations if its contribution is not properly taken into account. We have measured photoionization time delays between electrons originating from Ar and Ne, revealing Ar-photoelectrons to be delayed by tens of attosecond across a wide range of XUV photon energies. These results are in agreement with theoretical predictions, based on the calculation of the transition matrix elements for two-photon ionization. We expect our results to contribute towards resolving the controversies about single-photon ionization delays.

Chapter 9

Conclusion and outlook

The focus of this thesis has been the development of attosecond pulse sources and their application to time-resolved studies on atomic and molecular systems. To this end, initial work has been done on the already existing attosecond beamline called ‘Attoline’ [74]. Setting up a filament pulse compression setup in conjunction with the polarization gating (PG) technique led to the production of the first single attosecond pulses (SAPs) on this beamline. Among others this allowed for a range of experiments conducted on the transient absorption- and surface science project. In this thesis this know-how was transferred to the COLTRIMS detector sub-group in order to combine attosecond resolution with the unique possibilities of a COLTRIMS detector.

The combined knowledge enabled us to build up the ’AttoCOLTRIMS’ which is a symbiosis of an attosecond beamline and a COLTRIMS apparatus capable for XUV-IR pump-probe experiments using attosecond pulse trains (APTs) or SAPs. The COLTRIMS setup was previously used for IR-only experiments e.g. in an ‘Attoclock’ configuration using close-to-circular polarized IR pulses in combination with tight back-focusing. A number of interesting studies have been carried out [5,71-73]. Therefore, care was taken to keep the option to perform IR-only experiments by incorporating the possibility to bypass the XUV front-end setup.

Due to the relatively long acquisition times necessary when experiments are conducted with coincidence detection it is important to ensure stable interferometric conditions. Therefore, an active interferometer stabilization (AIS) has been installed providing long-term stability. Both the stability and reliability were demonstrated by two-color experiments, involving an XUV pump and an IR probe, showing excellent performance. The accuracy of the AIS has been determined more quantitatively revealing a standard deviation of less then 60 as over more then 7 hours.

The production of SAPs allowed to perform the first streaking measurements recorded with a COLTRIMS detector. The SAPs were generated by few-cycle IR pulses in conjunction with the PG technique. The streaking measurements have been used to characterize the temporal structure of the SAPs by the Frequency-Resolved Optical Gating for Complete Reconstruction of Attosecond Bursts (FROG-CRAB) technique. The reconstruction revealed a clean SAP with a pulse duration of 280 as. The observed chirp suggests further pulse compression by the use of a thinner aluminum foil.

Unlike time-of-flight (TOF) or velocity map imaging (VMI) spectrometers a COLTRIMS detector is able to reconstruct the full 3D momentum vector of charged fragments. Streaking measurements, therefore, can be conducted for a randomly oriented streaking field. Particularly, the energy streaking of an elliptically polarized IR can be measured equally in each direction. This capability was used within this thesis to perform an in situ measurement of the rotating electric field vector of an elliptically polarized IR field. For the experiment a high degree of ellipticity was preferential. Due to the constraints of the setup wave plates could only be placed before the grazing incidence toroidal and $45°$ holey mirror which strongly modify an initially close to circular polarized field. A combination of a $\lambda/4$- and a $\lambda/2$-plate was therefore used to compensate at least for part of the changes. For a fast but rough determination of the ellipticity the pulse energy was ramped up in order to generate so-called above-threshold ionization (ATI) electrons that can be easily detected with the COLTIMS apparatus. ATI is a strongly nonlinear effect scaling rapidly with the field intensity. Minimization the signal by the two wave plates, hence, allowed to find the configuration for highest in situ ellipticity. The measurement revealed that the two components of the electron momentum distribution in the polarization plane of the IR oscillate (streak). The center-of-mass (COM) analysis of these traces directly exhibited a $\pi/2$ phase shift. A quantitative analysis yielded an ellipticity of 0.69.

The above mentioned scheme is also straightforwardly applicable to complex time-dependent electric fields. We believe that this method can substantially contribute to studies in which the exact knowledge of the electric field structure of the IR is of significance.

The characterization of the IR streaking field makes use of the 3D momentum resolution of the COLTRIMS. But also the coincidence capability of the detector was exploited within the scope of this thesis.

The single-photon ionization time-delay between 3p argon and 2p neon electrons was measured with attosecond streaking experiments. Here, a gas mixture was used containing both species. Thanks to the coincidence detection it is possible to distinguish between both types of electrons even though they mostly overlap in energy. Hence, two streaking traces were extracted out of one single measurement allowing for identical conditions for both species. A direct comparison between the traces is possible thereby eliminating the intrinsic problem of a time zero definition in delay measurements. As shown the analysis of the data is not straightforward. It is well known that the single-photon ionization time-delays are energy-dependent. Therefore, a COM analysis can give no more then an averaged delay. But in many cases it can also easily yield misleading results due to non-uniform ionization cross-sections. The latter prevent the electron spectra to be a perfect replica of the XUV photon spectrum leading to shifts of the COM of the electron distributions. The comparison of the COM therefore contains not only the intrinsic time-delay but also a time-delay originating from the XUV phase.

The FROG-CRAB technique has been applied in order to retrieve the energy-dependent time-delay out of the measurements. This is possible since FROG-CRAB allows the extraction of the phases of either traces. Time-delays are therefore determined by the subsequent calculation of the group delay differences given by the derivative of the phases. But also here, it was shown that results can be incorrect if the two resulting electron group delay curves are subtracted directly: Assuming a fixed photon energy electrons generated from the 3p state of argon and the 2p state of neon will have different kinetic energies. Hence, the group delay difference determined at the same electron energy contains a contribution of the XUV phase. This problem can be solved by re-plotting the group delays as a function of the photon energy using the known ionization potential of both species.

As presented in chapter 8.1 a total number of 33 measurements have been performed containing each one argon and one neon trace. Using all measurements allowed to improve the accuracy of the result which reveals an energy-dependent time-delay ranging from 0–70 as in the energy region between 28-38 eV. This result has been compared to theoretical calculations and was found to be in good agreement.

With these measurements it has been demonstrated that the AttoCOLTRIMS setup is well suited to address a range open questioned that cannot be answered by today's established detectors in attosecond science.

The simultaneous streaking of different target species is a rather general approach that can also be used to measure photon ionization time-delays from other atomic species or even from molecules.

In the long-term one could think of extending the AttoCOLTRIMS with a double optical gating scheme which will allow to generate SAPs centered at higher energy having still sufficient pulse energy. This is favorable for two reasons: First, the FROG-CRAB reconstruction relies on the central momentum approximation which assumes that the bandwidth of the electron spectrum is narrow compared to the central energy of the distribution (see chapter 4.1). Second, low-energy electrons are created for species with high ionization potential or for those with a strong preference to absorb low-energy photons (Ar, H_2). A moderately strong IR field therefore already streaks the electrons to quasi-negative energies.

Ongoing experiments explore the angular resolution of the COLTRIMS detector to study the dependence of time-delays on the electron emission angle relatively to the XUV polarization. These measurements are self-referencing allowing to determine time-delays for different solid angles. Theoretical calculation show that Wigner time-delays should have a significant angular dependence [93]. This is a good test case to evaluate the validity of the theoretical models.

Another fascinating aspect of the COLTRIMS technique is that it allows in some cases to study molecular reactions not only in the laboratory but also in the molecular frame. This is possible e.g. for diatomic molecules when one of the atoms is ionized upon excitation followed by dissociation. The momentum of the charged ion can be determined and therefore the molecular axis due to momentum conservation. A range of theoretical proposals have been made, e.g. aiming to resolve the dynamics of the Q1 autoionizing doubly-excited state of molecular hydrogen [94,95] which is expected to decay within about 2 fs femtoseconds. Initial XUV-only studies have been already conducted by Fischer et al. [96] while time-resolved measurements are still pending. These measurements are challenging due to the extremely long acquisition times necessary for a reasonable signal–to-noise level (less than 5% of the electron counts correspond to dissociation of H_2). However, the AttoCOLTRIMS developed within the scope of this thesis has proven to be capable of long term-stability both in terms of the laser and interferometer. Therefore, it is expected to have the potential to address these open questions.

References

[1] M. Schultze *et al.*, Science **328**, 1658 (2010).

[2] G. Sansone *et al.*, Nature **465**, 763 (2010).

[3] A. L. Cavalieri *et al.*, Nature **449**, 1029 (2007).

[4] K. Klünder *et al.*, Phys. Rev. Lett. **106**, 143002 (2011).

[5] P. Eckle, A. N. Pfeiffer, C. Cirelli, A. Staudte, R. Dörner, H. G. Muller, M. Büttiker, and U. Keller, Science **322**, 1525 (2008).

[6] P. M. Paul, E. S. Toma, P. Breger, G. Mullot, F. Augé, P. Balcou, H. G. Muller, and P. Agostini, Science **292**, 1689 (2001).

[7] R. Kienberger, E. Goulielmakis, M. Uiberacker, A. Baltuska, V. Yakovlev, U. Heinzmann, M. Drescher, and F. Krausz, Nature **427**, 817 (2004).

[8] R. Dörner, V. Mergel, O. Jagutzki, L. Spielberger, J. Ullrich, R. Moshammer, and H. Schmidt-Bocking, Phys. Rep. **330**, 95 (2000).

[9] J. Ullrich, R. Mooshammer, A. Dorn, R. Dörner, L. P. H. Schmidt, and H. Schmidt-Böcking, Rep. Prog. Phys. **66**, 1463 (2003).

[10] E. Goulielmakis *et al.*, Science **320**, 1614 (2008).

[11] K. Zhao, Q. Zhang, M. Chini, Y. Wu, X. Wang, and Z. Chang, Optics Letters **37**, 3891 (2012).

[12] E. Goulielmakis *et al.*, Nature **466**, 739 (2010).

[13] N. F. Scherer, J. L. Knee, D. D. Smith, and A. H. Zewail, J. Phys. Chem. **89** (1985).

[14] M. Dantus, M. J. Rosker, and A. H. Zewail, J. Chem. Phys. **87** (1987).

[15] A. H. Zewail, Pure Appl. Chem. **72**, 2219 (2000).

[16] A. McPherson, G. Gibson, H. Jara, U. Johann, T. S. Luk, I. A. McIntyre, K. Boyer, and C. K. Rhodes, J. Opt. Soc. Am. B **4**, 595 (1987).

[17] P. B. Corkum, Phys. Rev. Lett. **71**, 1994 (1993).

[18] M. Hentschel *et al.*, Nature **414**, 509 (2001).

[19] I. J. Sola *et al.*, Nature Physics **2**, 319 (2006).

[20] E. Goulielmakis *et al.*, Nature **466**, 739 (2010).

[21] H. Wang, M. Chini, S. Chen, C.-H. Zhang, F. He, Y. Cheng, Y. Wu, U. Thumm, and Z. Chang, Phys. Rev. Lett. **105**, 143002 (2010).

[22] M. Holler, F. Schapper, L. Gallmann, and U. Keller, Phys. Rev. Lett. **106**, 123601 (2011).

[23] S. B. W. O. Hemmers, P. Glans, H. Wang, D. W. Lindle, R. Whlitz, I.A. Sellin, Rev. Sci. Instrum. **69** (1998).

[24] A. T. J. B. Eppink and D. H. Parker, Rev. Sci. Instrum. **68**, 3477 (1997).

[25] T. H. Maiman, Nature **187**, 493 (1960).

[26] F. P. Schäfer, F. P. W. Schmidth, and J. Volze, Appl. Phys. Lett. **9**, 306 (1966).

[27] P. M. W. French, J. A. R. Williams, and J. R. Taylor, Optics Lett. **14**, 686 (1989).

[28] D. K. Negus, L. Spinelli, N. Goldblatt, and G. Feugnet, in *Advanced Solid-State Lasers*, edited by G. Dubé, and L. Chase (Optical Society of America, Washington, D.C., 1991), pp. 120.

[29] R. Szipöcs, K. Ferencz, C. Spielmann, and F. Krausz, Optics Lett. **19**, 201 (1994).

[30] A. Wirth *et al.*, Science **334**, 195 (2011).

[31] C. Vozzi, F. Calegari, E. Benedetti, S. Gasilov, G. Sansone, G. Cerullo, M. Nisoli, S. De Silvestri, and S. Stagira, Opt. Lett. **32**, 2957 (2007).

[32] U. Keller, Nature **424**, 831 (2003).

[33] D. Strickland and G. Mourou, Optics Communications **56**, 219 (1985).

[34] H. R. Telle, G. Steinmeyer, A. E. Dunlop, J. Stenger, D. H. Sutter, and U. Keller, Appl. Phys. B **69**, 327 (1999).

[35] J.-C. Diels, E. W. V. Stryland, and D. Gold, in *First international conference on picosecond phenomena*Hilton Head, South Carolina, USA, 1978), pp. 117.

[36] D. J. Kane and R. Trebino, IEEE J. Quantum Elect. **29**, 571 (1993).

[37] C. Iaconis and I. A. Walmsley, Opt. Lett. **23**, 792 (1998).

[38] K. W. DeLong, D. N. Fittinghoff, R. Trebino, B. Kohler, and K. Wilson, Opt. Lett. **19**, 2152 (1994).

[39] W. J. Tomlinson, R. H. Stolen, and C. V. Shank, J. Opt. Soc. Am. B **1**, 139 (1984).

[40] M. Nisoli, S. DeSilvestri, and O. Svelto, Appl. Phys. Lett. **68**, 2793 (1996).

[41] C. P. Hauri, W. Kornelis, F. W. Helbing, A. Heinrich, A. Courairon, A. Mysyrowicz, J. Biegert, and U. Keller, Appl. Phys. B **79**, 673 (2004).

[42] P. A. Franken, A. E. Hill, C. W. Peters, and G. Weinreich, Physical Review Letters **7**, 118 (1961).

[43] M. Hentschel *et al.*, Nature **414**, 509 (2001).

[44] L. Gallmann, C. Cirelli, and U. Keller, Annu. Rev. Phys. Chem. **63**, 447 (2012).

[45] F. Krausz and M. Ivanov, Rev. Mod. Phys. **81**, 163 (2009).

[46] R. Locher, L. Castiglioni, M. Lucchini, M. Greif, L. Gallmann, M. Hengsberger, and U. Keller, in *CLEO Europe - IQEC 2013*Munich, 2013), pp. Postdeadline talk PD.

[47] M. V. Ammosov, N. B. Delone, and V. P. Krainov, Sov. Phys. JETP **64**, 1191 (1986).

[48] Z. Chang, CRC Press (2011).

[49] A. L'Huillier, C. Schafer, and K. C. Kulander, J. Phys. B: At. Mol. Opt. Phys. **24**, 3315 (1991).

[50] C. G. Durfee, A. R. Rundquist, S. Backus, C. Herne, M. M. Murnane, and H. C. Kapteyn, Phys. Rev. Lett. **83**, 2187 (1999).

[51] E. Constant, D. Garzella, P. Breger, E. Mével, C. Dorrer, C. Le Blanc, F. Salin, and P. Agostini, Physical Review Letters, 1668 (1999).

[52] P. Antoine, A. L'Huillier, and M. Lewenstein, Phys. Rev. Lett. **77**, 1234 (1996).

[53] V. Véniard, R. Taïeb, and A. Maquet, Physical Review A **54** (1996).

[54] J. Mauritsson, M. B. Gaarde, and K. J. Schafer, Phys. Rev. A **72**, 013401 (2005).

[55] E. Goulielmakis *et al.*, Science **305**, 1267 (2004).

[56] Y. Mairesse and F. Quéré, Phys. Rev. A **71**, 011401 (2005).

[57] P. B. Corkum, N. H. Burnett, and M. Y. Ivanov, Opt. Lett. **19**, 1870 (1994).

[58] I. J. Sola *et al.*, Nat Phys **2**, 319 (2006).

[59] G. Sansone *et al.*, Science **314**, 443 (2006).

[60] K. S. Budil, P. Salières, A. L'Huillier, T. Ditmire, and M. D. Perry, Physical Review A **48** (1993).

[61] V. Strelkov, A. Zaïr, O. Tcherbakoff, R. López-Martens, E. Cormier, E. Mével, and E. Constant, Journal of Physics B: Atomic, Molecular and Optical Physics **38**, L161 (2005).

[62] E. Benedetti, Ph.D. thesis Polytecnico die Milano (2007-2008).

[63] H. Mashiko, S. Gilbertson, C. Li, S. D. Khan, M. M. Shakya, E. Moon, and Z. Chang, Phys. Rev. Lett. **100**, 103906 (2008).

[64] M. J. Abel, T. Pfeifer, P. M. Nagel, W. Boutu, M. J. Bell, C. P. Steiner, D. M. Neumark, and S. R. Leone, Chem. Phys. **366**, 9 (2009).

[65] F. Ferrari, F. Calegari, M. Lucchini, C. Vozzi, S. Stagira, G. Sansone, and M. Nisoli, Nature Photon. **4**, 875 (2010).

[66] H. Vincenti and F. Quéré, Physical Review Letters **108**, 113904 (2012).

[67] D. J. Bradley, B. Liddy, and W. E. Sleat, Opt. Comm. **2**, 391 (1971).

[68] M. Lewenstein, P. Balcou, M. Y. Ivanov, A. L'Huillier, and P. B. Corkum, Phys. Rev. A **49**, 2117 (1994).

[69] P. Eckle, *Attosecond Angular Streaking* (Südwestdeutscher Verlag für Hochschulschriften, 2008), 18118.

[70] F. X. Kärtner, U. Morgner, R. Ell, T. Schibli, J. G. Fujimoto, E. P. Ippen, V. Scheuer, G. Angelow, and T. Tschudi, JOSA B **18**, 882 (2001).

[71] P. Eckle, M. Smolarski, P. Schlup, J. Biegert, A. Staudte, M. Schöffler, H. G. Muller, R. Dörner, and U. Keller, Nature Phys. **4**, 565 (2008).

[72] A. N. Pfeiffer, C. Cirelli, M. Smolarski, D. Dimitrovski, M. Abu-samha, L. B. Madsen, and U. Keller, Nature Phys. **8**, 76 (2012).

[73] R. Boge, C. Cirelli, A. S. Landsman, S. Heuser, A. Ludwig, J. Maurer, M. Weger, L. Gallmann, and U. Keller, Physical Review Letters **111** (2013).

[74] R. Locher *et al.*, Review of Scientific Instruments **85**, 013113 (2014).

[75] H. M. M. Chini, H. Wang, S. Chen, C. Yun, S. Scott, S. Gilbertson, Z. Chang, Opt. Express. **17** (2009).

[76] H. Wang, M. Chini, S. D. Khan, S. Chen, S. Gilbertson, X. Feng, H. Mashiko, and Z. Chang, J. Phys. B-At. Mol. Opt. Phys. **42** (2009).

[77] R. Lopez-Martens *et al.*, Phys. Rev. Lett. **94**, 033001 (2005).

[78] H. G. Muller, Appl. Phys. B **74**, S17 (2002).

[79] A. S. Landsman, M. Weger, J. Maurer, R. Boge, A. Ludwig, S. Heuser, C. Cirelli, L. Gallmann, and U. Keller, arXiv:1301.2766v2 (2013).

[80] J. Gagnon and V. S. Yakovlev, Opt. Express. **17**, 17678 (2009).

[81] A. S. Kheifets, Phys. Rev. A **87**, 063404 (2013).

[82] L. R. Moore, M. A. Lysaght, J. S. Parker, H. W. van der Hart, and K. T. Taylor, Physical Review A **84**, 061404(R) (2011).

[83] E. P. Wigner, Physical Review **98**, 145 (1955).

[84] A. P. French and E. F. Taylor, W. W. Norton & Company (1978).

[85] B. I. Schneider, J. Feist, S. Nagele, R. Pazourek, S. Hu, L. A. Collins, and J. Burgdörfer, Quantum Dynamic Imaging, CRM Series in Mathematical Physics, 149 (2011).

[86] S. Nagele, R. Pazourek, J. Feist, K. Doblhoff-Dier, C. Lemell, K. Tökési, and J. Burgdörfer, J. Phys. B: At. Mol. Opt. Phys. **44**, 081001 (2011).

[87] C. T. Chantler, K. Olsen, R. A. Dragoset, J. Chang, A. R. Kishore, S. A. Kotochigova, and D. S. Zucker, http://physics.nist.gov/ffast [Wednesday, 16-Jul-2014 10:28:25 EDT] (2005).

[88] J. M. Dahlström, A. L'Huillier, and A. Maquet, J Phys B-At Mol Opt **45** (2012).

[89] J. M. Dahlström, T. Carette, and E. Lindroth, Phys. Rev. A **86**, 061402(R) (2012).

[90] F. T. Smith, Phys. Rev. **118**, 349 (1960).

[91] R. Pazourek, S. Nagele, and J. Burgdörfer, submitted to Reviews of Modern Physics (2014).

[92] R. Pazourek, S. Nagele, and J. Burgdörfer, Faraday Discussions **163**, 353 (2013).

[93] J. M. Dahlström and E. Lindroth, arXiv: 1404.3895v1 [physics.atom-ph] (2014).

[94] F. Felipe Morales, J. F. Pérez-Torres, J. L. Sanz-Vicario, and F. Martín, Chem Phys **366**, 58 (2009).

[95] J. F. Pérez-Torres, F. Morales, J. L. Sanz-Vicario, and F. Martín, Physical Review A **80**, 011402(R) (2009).

[96] A. Fischer *et al.*, Physical Review Letters **110**, 213002 (2013).

Curriculum Vitæ

Personal

Name:	Mazyar Sabbar
Date of Birth:	September 21, 1983 (Tehran, Iran)
Nationality:	German

Education

05/2010 – 09/2014	PhD studies in the group of Prof. Dr. Ursula Keller, Institute of Quantum Electronics, Physics Department, ETH Zurich, Switzerland
10/2004 – 01/2010	Diploma in Physics, Leibniz Universität Hannover, Germany
02/2008 – 08/2008	Academic exchange, Universidad de Salamanca
10/2004 – 10/2006	Pre-diploma in Physics, Leibniz Universität Hannover, Germany
08/1996 – 08/2003	Gymnasium Helene-Lange-Schule, Abitur

Research Experience

08/ 2009 – 09/2013	PhD studies at the Institute of Quantum Electronics, ETH Zurich, Switzerland (Attosecond science, ultrafast light-matter interactions)
09/2008 – 02/2009	Diploma thesis at Institut für Quatenoptik (IQO) at Leibniz Universität Hannover, Germany, (Microwave evaporation in a hybrid trap for the production of quatum degenerated atom mixtures)

Acknowledgements

An dieser Stelle möchte ich die Gelegenheit nutzen, all denen zu danken, die zum Erfolg dieser Doktorarbeit beigetragen haben und mich während dieser Zeit unterstützt haben.

Ursi möchte ich für die Bereitstellung der exzellenten Rahmenbedingungen bedanken. Außerdem danke ich dir für das Vertrauen, das du uns entgegen gebracht hast die Freiheiten, die du uns gewährt hast.

Bei Lukas möchte ich mich für die kompetenten Gespräche und für das Engagement beim Schreiben der Paper bedanken. Deine Kommentare waren stets hilfreich.

Ich bedanke mich bei Hans Jakob für das unkomplizierte Übernehmen des Korreferats und auch für die interessanten Diskussionen auf den Konferenzen.

Sebastian Heuser danke ich für die produktive, aber auch unterhaltsame Zeit im Labor. Es gab einige Momente, die ich in guter Erinnerung behalten werde: Die Fischer`sche Wellenfunktion, mit einem charakteristischen Maximum in Heidelberg und Zürich. Oder aber auch der Klassiker: „Ich glaube wir brauchen dringend professionelle Hilfe.“.

Robert Boge danke ich für die interessanten Diskussionen rundum die Experimente. Insbesondere aber auch für die Installation der AIS und des Super-Racks. In guter Erinnerung wird mir auch die „Nahtod-Erfahrung“ im Zusammenhang mit der bis heute mysteriösen Erdung bleiben.

Claudio Cirelli danke ich für die unkomplizierte und hilfreiche Unterstützung insbesondere beim Schreiben der Paper aber auch für die gute Atmosphäre im Team. Unsere z.T. langen und intensiven Diskussionen über Wissenschaft und das Drumherum waren immer ein Vergnügen.

Jochen, Benedikt und André möchte ich für das gute Miteinander und für die z.T. amüsanten Momente im E9 danken. Jochen: „Gib alles!“ oder André: „Wow wow wowa wow“.

Ein spezielles Dankeschön an Benedikt. Du hast stets Rücksicht auf unsere Messungen genommen.

Meiner Bürokollegin Cornelia möchte ich für die gute Atmosphäre danken. Sorry nochmals für die Endlosdiskussionen, die fortwährend im Büro stattgefunden haben.

Ich möchte mich aber auch bei den anderen Mitgliedern der sub-10 und den Ehemaligen bedanken:

Clemens Heese, Jens Herrmann („Oma, gibt's noch Curryking?“), Reto Locher (mit George Michael im Labor – das war schon was), Matteo Lucchini (Never running out of good jokes!), Adrian Pfeiffer (auf einer 1m Couch schlafen nach Stuz2), Thomas Remetter („Hey Guys...“), Mathias Smolarski, Matthias Weger (Danke für die interessanten Wanderausflüge.)

Natürlich bedanke ich mich auch recht herzlich bei den anderen Gruppenmitgliedern, mit denen ich die Freizeitaktivitäten stets genossen habe:

Cyrill Bär, Yohan Barbarin, Andreas Diebold, Florian Emaury, Matthias Golling, Oliver Heckl, Martin Hoffmann, Lamia Kasmi, Alexander Klenner (Nie werde ich unseren Abend im Supermarket vergessen :D), Alexandra Landsman, Sandro Link, Mario Mangold, Aline Mayer, Wolfgang Pallmann, Selina Pekarek, Christopher Phillips, Clara Saraceno, Cina Schriber, Oliver Sieber, Thomas Südmeyer, Bauke Tilma, Valentin Wittwer, Hirofumi Yanagisawa, Christian Zaugg.

Den Mitarbeitern des Ingenieursbüros (Marcel Bär und Walter Bachmann), der Labortechnik (Hansruedi Scherrer und Sandro Tiegermann) und der Werkstatt (Andreas Stuker und Bernhard Morath) möchte ich für die zuverlässige und hervorragende Arbeit danken. Ohne diese Hilfe wäre Vieles nicht möglich gewesen.

Unserer Büroleiterin Sandra Schmid möchte ich danken für ihre Geduld mit uns PhD Studenten und Postdocs.

Auch dem NCCR MUST office gebührt ein großes Dankeschön für die Koordination der vielen ausgezeichneten Veranstaltungen.

Ich möchte auch die Gelegenheit nutzen meiner Familie zu danken. Sie hat mich zu jedem Zeitpunkt unterstützt. Dies hat mir den Rücken gestärkt und mich auf meinem Weg motiviert. Zum Schluss, aber nicht zuletzt, möchte ich mich bei meiner Freundin Mena bedanken, die mir sowohl in guten als auch in schwierigen Zeiten fortwährend zur Seite gestanden hat. Du hast einen großen Anteil am Erfolg dieser Arbeit.

M. Sabbar

Zürich, August 2014